SCUOLA DI SCIENZE

Dipartimento di Chimica Industriale“Toso Montanari”

Corso di Laurea Magistrale in

Chimica Industriale

Classe LM-71 - Scienze e Tecnologie della Chimica Industriale

Correlation between structure and electrochemistry of $LiMO_2$ cathode materials (M = Ni, Co)

Tesi di laurea sperimentale

RELATORE

Chiar.mo Prof. Marco Giorgetti

CANDIDATO

Cristina Grosu

CORRELATORI

Dr. Karin Kleiner

Johannes Sicklinger

Dr. Michele Piana

Chiar.mo Prof. Hubert Gasteiger

Sessione III

Anno Accademico 2015-2016

Abstract

Technical diversity and various knowledge is required for the understanding of undoubtedly complex system such as a Lithium-ion battery. The peculiarity is to combine different techniques that allow a complete investigation while the battery is working. Nowadays, research on Li-ion batteries (LIBs) is experiencing an exponential growth in the development of new cathode materials. Accordingly, Li-rich and Ni-rich NMCs, which have similar layered structure of $LiMO_2$ oxides, have been recently proposed. Despite the promising performance on them, still a lot of issues have to be resolved and the materials need a more in depth characterisation for further commercial applications. In this study $LiMO_2$ material, in particular M = Co and Ni, will be presented. We have focused on the synthesis of pure $LiCoO_2$ and $LiNiO_2$ at first, followed by the mixed $LiNi_{0.5}Co_{0.5}O_2$. Different ways of synthesis were investigated for LCO but the sol-gel-water method showed the best performances. An accurate and systematic structural characterization followed by the appropriate electrochemical tests were done. Moreover, the in situ techniques (in-situ XRD and in situ OEMS) allowed a deep investigation in the structural change and gas evolution upon the electrochemically driven processes.

Table of contents

1 Introduction

The exponential growth of the energy demand, not only from the developed countries but also from the developing ones, results in an extreme increase of pollution which forces research to focus on finding an alternative to the use of fossil fuels. Since it has been recognized that ~ 23% of the CO_2 evolution is due to the emission from transportation, it is important to decrease the amount of CO_2 from vehicles in order to reach the future emission target. In fact, the most recent Paris agreement on the environment has the purpose to reduce the emission by 21% till 2020 and by 43% till 2030.[1]

Therefore, it is necessary to develop an alternative power supply for vehicles, which may use batteries, fuel cells or a combination of both.[2] In order to extend the use of electric vehicles (BEV), hybrid electric vehicles (HEV) or even fuel cell driven cars the usage of renewable energies to produce hydrogen or to charge batteries has also to be enhanced.[2] Renewable energy sources like wind-, solar- and hydropower are stationary and temporary applications which also need energy storage systems like batteries. Therefore, research also focuses on finding a compromise for the BEV market and stationary energy storage systems with a second life application. After batteries reach the end of life in a vehicle (actual capacity of 80 % compared to the capacity at begin of life) they still can be used for stationary applications for which the operation conditions are less harsh.

In this context, the present work focuses on the field of batteries. One of the main challenges in the last decades of battery research is the long-term cycling stability of cathode materials in a lithium-ion battery. Since the commercialization of the first lithium ion battery (LiB) by SONY in 1991, layered oxides are the most suitable materials in order to achieve high energy densities and long term stability of a lithium-ion battery.[3] Different types of lithium-ion batteries are already widely used in commercial products like laptops, cell phones, cameras, etc. However, the application of batteries in electric vehicles still requires higher energy densities, even if other side parameters have to be taken into account.[4,5] To figure out, which system fits to electric vehicles, a more fundamental understanding of the different materials needs to be generated. Although the characteristics of the LiB depend on both cathode and anode material, improvements on the positive electrode will have a higher impact upon the overall cell performance as anodes, since they already offer higher capacities.[6]

The most commercially used cathode materials are $LiCoO_2$ and different isostructural layered oxides ($LiMO_2$ with M = Co, Ni, Mn and Li), as for example $Li(Ni_{1/3}Co_{1/3}Mn_{1/3})O_2$ known as

NMC, which is shown in Figure 1. The most recent developed material, which is still based on this structure but offers a higher energy density, is the Li-rich NMC, known also as High-Energy NMC.[7,8,9]

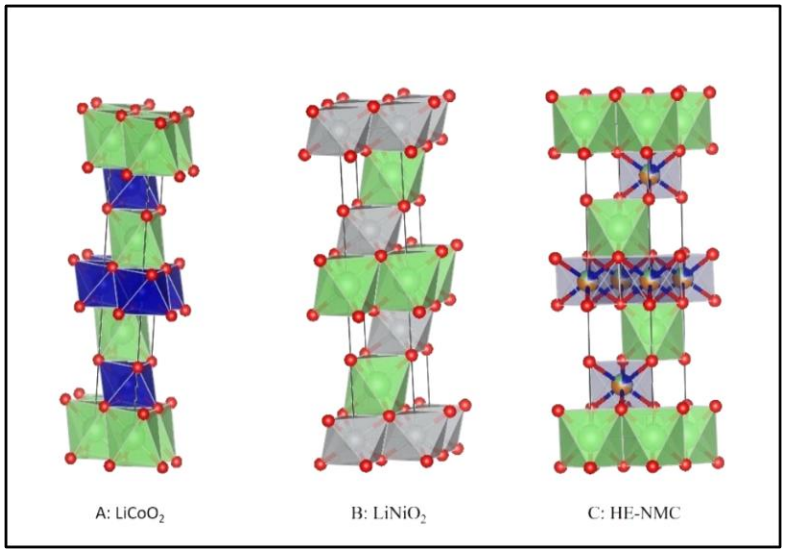

Figure 1: Structural illustration of layered, R-3m, LMO_2 (M=Co, Ni) and HE-NCM. Graphic was created using VESTA with red: oxygen, blue: cobalt, grey: nickel, orange: manganese and green: lithium.

The advantages of the mixed layered oxides are high energy and power densities as well as the high operation voltage. However, the capacity loss and voltage decay upon cycling is still not completely understood. The complexity of the structure in this class of materials requires various techniques to understand fading mechanisms. Although the synergy of different transition metals on the structure are known, it is suggested to start from the basic understanding of the simple layered oxide as $LiMO_2$ (M=Co, Ni). The aim is to find the relationship between structural changes and the electrochemical properties of each of this transition metals with a well-defined stoichiometry and to deduce the role of each cation during the operation inside the cell.[7,9]

2 Batteries: state of art

A battery is an electrochemical device that converts chemical energy into electrical energy. Batteries have the capability to store energy supplied by an external source and therefore they can act as a portable source of electric power. Originally, the "battery" term was used to refer to a group of "cells" which are connected in series or parallel for having the requested performance. However, nowadays battery and cell are used interchangeably, as can be found also in this work.[10]

In an electrochemical cell, Red-Ox reactions take place on or in electrodes where the energy is converted. The underlying process is an electron migration from one chemical species to another through an electron conductor (which carries out work), and a simultaneous ion migration through an ionic conductor. The charge transfer, during charge takes place at the electrode interfaces: the negative electrode (anode) supplies electrons to the external circuit while being oxidized, and the positive electrode (cathode) receives them while being reduced.[10] For the representation of a lithium ion battery see Figure 2.[11]

To prevent an internal short circuit between the anode and cathode an insulating (but ionic conducting) material is required that usually is porous and soaked with electrolyte. The electrolyte is working as an ionic conductor with electric isolating properties. The cell reaction proceeds spontaneously, driven by the net free energy change and the total amount of charge that can be supplied to the external circuit Q, "theoretical cell capacity", that is given by Faraday´s law, shown in equation 1:

$$Q = \int_0^t i \times dt = nF \times N \tag{1}$$

Where *i* is the current flowing in the circuit, *t* is the time, *n* is the number of electrons associated with the redox reaction, *F* is the Faraday´s constant (96485 C/mol) and *N* represent the number of mole of reactant participating in the reaction. Due to technical limits the theoretical cell capacity is almost never reached. However, this can be an indication for the maximum energy density of the battery.

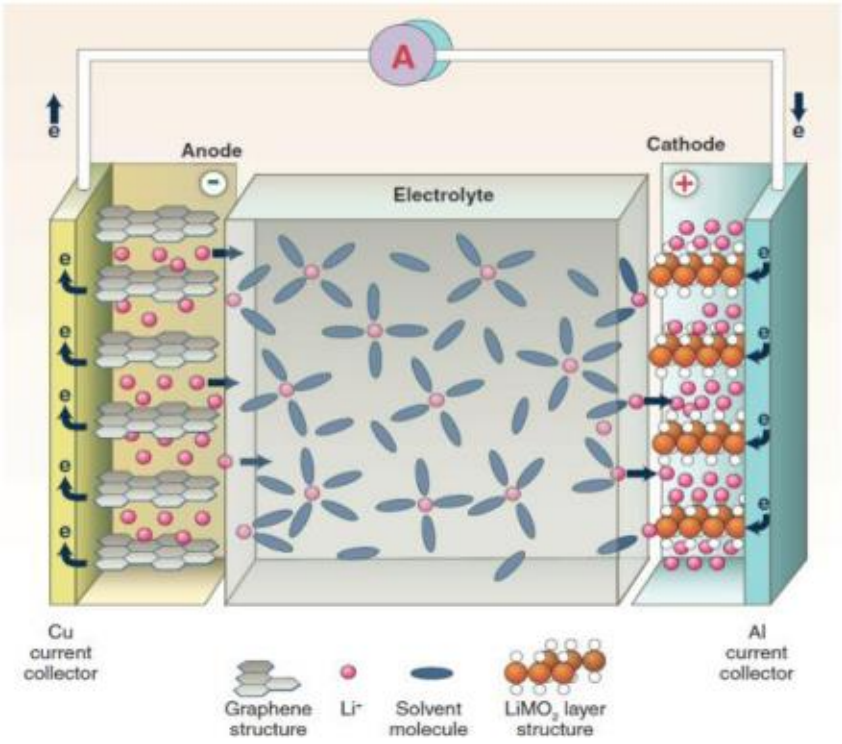

Figure 2: Representation of a lithium ion battery.[11]

Batteries are in common divided into in “primary” and “secondary” batteries. For a “primary battery” the cell stops running when all the reactants are consumed and it is fully discharged. Examples are alkaline batteries, zinc-carbon or lithium batteries (for this Li is used as metallic anode). While in this case the reaction is not reversible, “secondary batteries” can be re-charged due to reversible reactions. For re-charging this kind of batteries an external electric power source can be used. The lead-acid, nickel cadmium (Ni-Cd), nickel metal hydrate (Ni-MH) and last but not least lithium-ion batteries (LiBs) are secondary batteries.[10,12] To compare different battery systems, various parameters can be used. However, the characteristic performance parameters of energy storage devices (not only limited to batteries) are graphically illustrated best by the Ragone plot shown in Figure 3.

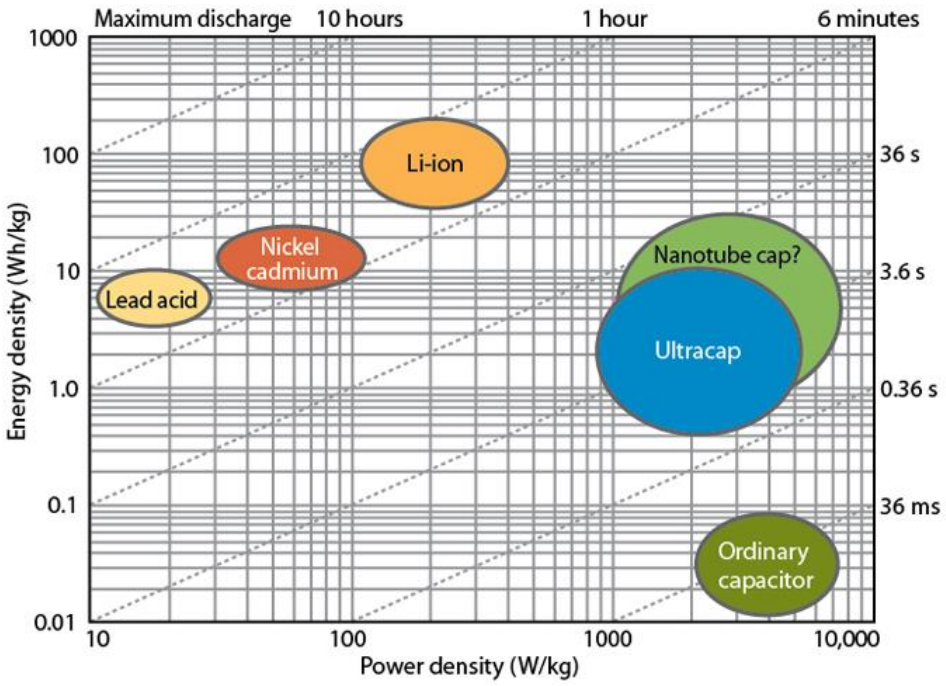

Figure 3: Depiction of the energy density as a function of the power density: The so called Ragone Plot.[13]

The specific energy density in Wh/kg is plotted as a function of the specific power density in W/kg in order to illustrate both the energy that the device can deliver and the ability to deliver that energy. The bi-logarithmic axes allow the comparison between devices with extremely different values in energy or power. The expression of both is shown by Equations (2) and (3).

$$Specific\ Energy = \frac{U_{avg} * I * t}{m} \tag{2}$$

$$Specific\ Power = \frac{U * I_{max}}{m} \tag{3}$$

U is the present voltage [V], U_{avg} is the average voltage [V] of the cell during one cycle, I is the current [A], t is the time [s] and m is the mass [kg]. Compared to other battery technologies, the lithium ion batteries offer higher energy densities and similar or even higher power densities. Capacitors show a higher power density. However, they suffer from a poor energy density and therefore they are not suitable for an application in electric vehicles or for stationary energy storage systems.

2.1 Lithium-ion Batteries

The first lithium-ion battery was proposed in 1976[14,15] and since the market introduction in the early 1990s, Li-ion batteries have been widely adopted for a variety of portable electronic devices.[14] The development of the secondary cell based on lithium as the cationic charge carrier

started with lithium metal as negative electrode, a positive, polycrystalline electrode and the electrolyte that allows the transfer of Li-ions between the electrodes. The active material for the cathode should undergo a reversible reaction with Li-ions, which are de-intercalated during charge and re-intercalated during discharge. The chemical reaction that the electrodes undergo is shown in Equation (4). The lithiation (accompanied with an oxidation) of the cathode is usually called discharge while the charge (accompanied with a reduction) is the delithiation. Equation (15) shows the possibility of unlimited cycles of reduction and oxidation on both electrodes (respectively discharge and charge), in the case that the reaction is ideally reversible.

$$x\ Li^{+} + AM_{(s)} + x\ e^{-} \underset{\text{charge}}{\overset{\text{discharge}}{\rightleftharpoons}} Li_xAM_{(s)} \tag{4}$$

A schematic representation of the operation of a battery while charging and discharging is shown in Figure 4.

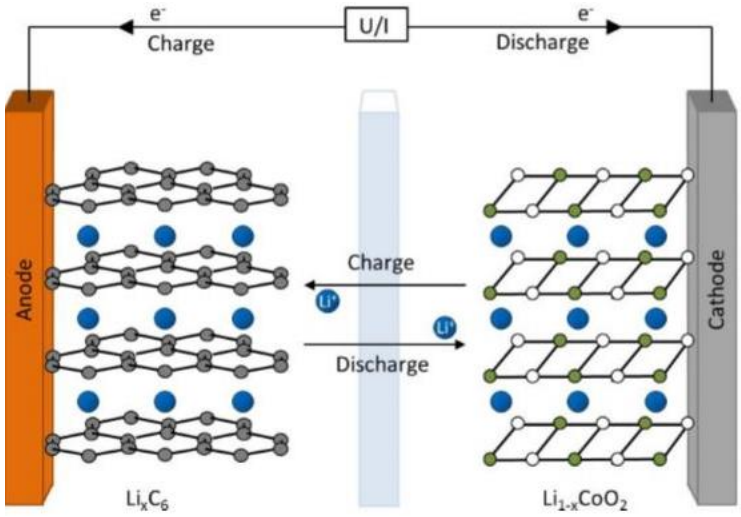

Figure 4: Schematic illustration of the charge and discharge of a lithium-ion battery.[16]

The performance of the cell depends on the nature of all of the components: the properties of the electrodes with a prudent selection of the active material, the electrolyte composition and the geometry of the cell assembling.[12] A brief overview of the basic components of the cell is given in the next subchapters.

2.1.1 Negative electrodes in lithium cells (Anode materials)

The first negative electrode in the secondary cell was metallic lithium because of the favourable thermodynamic electrode potential of 3 V versus the standard hydrogen electrode (the lowest potential of all elements) and the very high specific capacity (3.86 Ah/g; 7.23 Ah/cm^3). However, due to its highly electropositive nature electrolytes are unstable if they get in contact

with the lithium electrode. The organic decomposition products form a passivating layer (SEI, solid electrolyte interface) when the electrode is cycled and this introduces in some case safety hazards.[10,12] Under harsh operation conditions the decomposition products can further decompose in uncontrolled side reactions which produces heat and therefore initializes a thermal runaway of the cell. Li metal has also an intrinsic safety problem, because of the continuous dissolution and deposition of lithium-ions from or on top of the surface upon charge and discharge. The deposition of lithium-ions can lead to dendrite formation, which creates a higher surface area and also can lead to a short circuit in case the dendrites penetrate the separator. Under harsh operation conditions or in the case of a failure of the battery the temperature can raise enough to melt metallic lithium, which starts to react with more electrolyte, causing a further increase of temperature and the device goes on fire or explodes.[2]

A subsequent development replaced the metal lithium anode, which was mainly based on an insertion material, which allowed Li-ions to be intercalate. Currently graphite is used as negative anode, which intercalates Li and forms LiC_6. Even though carbon has a wide range of structures and properties which arise from the difference in the production process, graphite shows the best electrochemical properties. One of the major influences of the presence of lithium in the graphite crystal structure is that the stacking of graphene layers is changed by the insertion of lithium. The process of lithium intercalation into graphite occurs through formation of different "stages" with increasing ratio of Li/C which includes intercalation compounds such as LiC_{12}.[12]

In fact, the anode is affected by a rather high capacity loss of the battery during the first few charges due to the formation of the SEI, better known in the literature as ageing process on this electrode. The SEI is a particular solid layer that is formed after the first cycle of the battery, which provides a protective layer for the anode and avoids the continuous reduction of electrolyte, that will be discussed in the next chapter.[17]

Summing up the requirements of an anode material, a high efficiency is needed (no surface changes which force electrolyte decomposition reactions, the formation of a stable surface film in the first cycles), the safety risk with the respect to metallic lithium has to be reduced and the rate capability should be enhanced. Further the electrode should operate at potentials close to that of metallic Li to ensure a high-energy density, it should have a low equivalent weight for maximizing the specific capacity and it should be lightweight, cheap and safer than metallic lithium.[10,12]

As alternatives, to the carbonaceous materials, lithium alloys with silicon and anthimonium, titanates as $Li_4Ti_5O_{12}$ and titanium oxide (TiO_2) are taken into consideration because they operate at higher potentials at which the electrolyte is still stable and no SEI formation is necessary. However, this leads to lower energy densities and therefore graphite remains the most used anode in commercial batteries up to now.[12,18]

2.1.2 Electrolytes in lithium cell

As mentioned, the main function of the electrolyte is to work as an ionic conductor and an electronic isolator. Electrolytes for LiBs need to be stable at the electrode potentials applied in the cell. In the case of LiBs the chemical environment is quite demanding. As lithium reacts vigorously with water forming LiOH and hydrogen, an organic based anhydrous electrolyte is required. For the organic solvents, the solubility of the conductive lithium salts is often very challenging. Due to this, the electrolyte consists of a mixture of carbonates that present good solubility of the conducting salt as well as low viscosity. The most common electrolyte consists of ethylene carbonate (EC), dimethyl carbonate (DMC) and ethyl methyl carbonate (EMC). Propylenecarbonate (PC) was used in the beginning, but this resulted in exfoliation of the graphite anode.[19] The most used conducting salt is lithiumhexafluorophosphate ($LiPF_6$), as this offers the best compromise of solubility, conductivity, electrochemical stability and safety.[20] Obviously, any water trace must be removed not only due to the reactivity of lithium but also due to the decomposition of $LiPF_6$, which forms LiF and PF_5. This PF_5 will react with water to POF_3 and HF. As the organic solvents are not stable at very low potentials, a decomposition reaction is happening, leading to the SEI on the surface of the negative layer. For this reason, EC is fundamental to guarantee a good SEI formation on the surface of the graphite electrodes. In fact, this layer is a Li-ion conductor, but it is electrical isolating and thus also extends the potential window of the electrolyte. However, the EC only has a high viscosity and would have a low ionic conductivity. DMC or EMC are used to reduce the viscosity of EC and to promote a better Li-ion transport.[10,12]

2.1.3 Positive electrodes in lithium cells (Cathodes materials)

Since LiBs consist of various components, it is not easy to identify the impact of the individual components on the overall performance of the battery. However, the area of research of most interest within LIBs is dedicated in the moment to the improvement of the positive electrode. [7-9,21–24] In almost every case, the cathode materials are host structures which can undergo insertion reactions and are therefore also known as intercalation cathodes. An intercalation

cathode is a solid host network, which can store guest ions like Li-ions.[14,25] Nowadays a lot of intercalation cathodes can be found in the literature with different fields of applications. However, three main classes of cathode materials have to be considered. The first class use either layered oxides like $LiCoO_2$ or its derivatives ($LiMO_2$, M=Co, Ni, Mn and Li), the second one is based on the spinel-like compounds such as $LiMn_2O_4$ and the third one are polyanionic compounds with a olivine structure ($LiMPO_4$, M=Fe, Co, Mn and Ni).[4,7] Depending on the application the research is either taking safety and cost issues into consideration (spinel and olivine structures) or focuses on the energy density despite sometimes high costs (layered oxides). Since for the automobile industry the second aspect is the most important one, the $LiCoO_2$ chemistry with several improvements will be discussed further. In fact, the development of cathodes with a higher rate capability, a higher specific capacity, an enhanced cycle life and better safety characteristic is the target of the ideal cathode especially for EV application.[7]

2.1.3.1 Spinel LiM_2O_4

In the spinel structure LiM_2O_4 (M=Ti, V, and Mn), the most common $LiMn_2O_4$ adopts a normal spinel structure consisting of cubic close-packed oxide ions with the $M^{3+/4+}$ ions in the 16d octahedral sites and lithium ions in 8a tetrahedral sites, which gives a distribution of $(Li)_{8a}[Mn_2]_{16d}O_4$ (Figure 5). The Mn_2O_4 framework occupies a three-dimensional region via face sharing octahedron and tetrahedron, which provide three dimensional conducting pathways for the insertion and the extraction of the lithium-ions without collapsing the spinel framework.

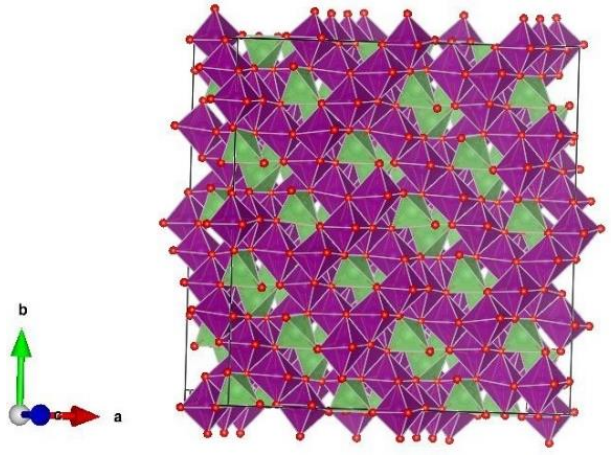

Figure 5: $LiMn_2O_4$ spinel structure. Graphic was created using VESTA with red: oxygen, purple: manganese and green: lithium.

$LiMn_2O_4$ is a promising material due to its rather low cost, high intrinsic safety issues compared Ni-rich layered oxides, that will be discussed below and its long-term stability.[18] The material has an operating potential of 4.1 V and offers a capacity of 148 $mAhg^{-1}$. This material suffers from pronounced capacity fade upon cycling under elevated temperatures due to Mn^{2+} dissolution (generated by the disproportion reactions $2\ Mn^{3+} \leftrightarrow Mn^{4+} + Mn^{2+}$) and secondary phase generation.[12,18,26]

2.1.3.2 Polyanion-based electrode materials, $LiMPO_4$ and $Li_xM_2(PO_4)_3$

The olivine family has been studied since $LiFePO_4$ (LFP) as an intercalation material has been discovered.[27] The crystal structure of olivines is shown in Figure 6 a. The $LiFePO_4$ has an hexagonal oxygen host structure, in which Li^+ and Fe^{2+} occupy half of the octahedral sites and PO_4^{3-} 1/8 of the tetrahedral sites. The peculiar distribution of Li^+ and Fe^{2+} within the octahedral sites generates [$TeOc_2$] layers. This connectivity has a special impact on both electronic and ionic conductivity in LFP. FeO_6 octahedrons share corners between each other and electronic delocalization are made difficult.

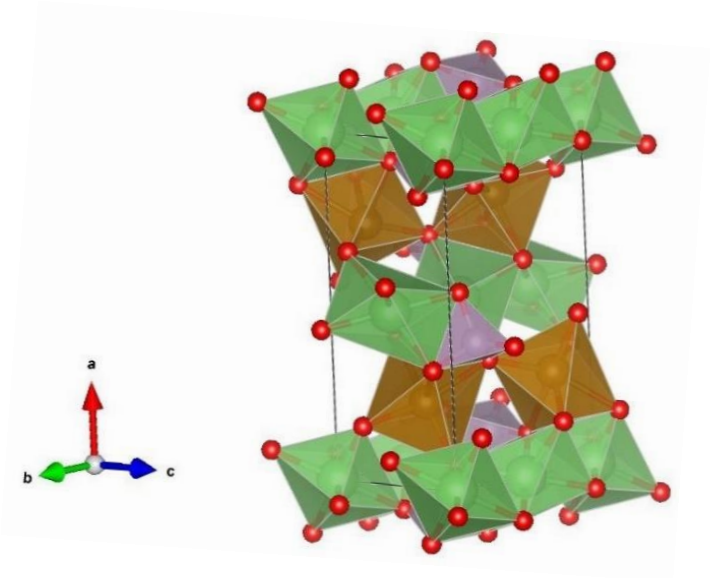

Figure 6: LiFePO4, olivine structure. Graphic was created with VESTA with red: oxygen, brown: iron, light purple: phosphorus and green: lithium.

The theoretical capacity of 170 $mAhg^{-1}$ at a flat voltage plateau of 3.5 V, the non-toxicity, the low price of iron and especially the long-term stability accompanied with a low safety risk makes it to a promising cathode material for stationary applications.[4,27] By substituting Fe with Mn, Co and Ni, the working potential and therefore the energy density which offers potential for further research.[4]

2.1.3.3 Layered Oxides LMO_2

In spite of a huge research work on the alternative cathode materials, the layered oxides, from the first commercial LIBs, introduced into market by Sony Corporation in 1991, still dominates the market for portable application.[27] Generically, the cell can be represented, as the most rechargeable lithium cells, how was said before use as anode the graphite matrix and $LiCoO_2$ as positive electrode:

$$Li_xC/\text{organic solvent electrolyte}/Li_{1-x}CoO_2$$

The redox reactions present in the most common commercial cell, that are represent and discussed below; it can be divided as one on the negative electrode during discharging process (Equations (5) and (6))

$$\text{(negative electrode)}\quad Li_xC_6 \rightarrow 6C + xLi^+ + xe \tag{5}$$

$$\text{(positive electrode)}\quad Li_{1-x}CoO_2 + xLi^+ + xe^- \rightarrow LiCoO_2 \tag{6}$$

With the combination of both that led us to the full cell reaction (Equation (7))[25,28]:

$$LiCoO_2 + 6C \leftrightarrow Li_{1-x}CoO_2 + Li_xC_6 + \text{energy} \tag{7}$$

However, the LCO is mostly used in various commercial application, is not suitable as it is, for EV or stationary energy storage. For the use in the EV, the major problems and limitations are high cost, low thermal stability, fast capacity fading if use at a high current and deep cycling.[2] In addition, the cost of processing the Co for the cathodes is the major contributing on overall cost, even if Li is not the cheapest one.[4]

Another problem is during the delithiation process in this type of materials, and taking the case of $LiCoO_2$/C Li-ion cell, it must be limited to 0.5 Li in the intercalation, which means that only half of the theoretical capacity is used (~ 140 mAh/g instead of 275 mAh/g). Over the time, also this limit with was tried to be overcome.[4,7] The attempts to substitute the cobalt during the last decades, lead to a different new cathodes materials developed on the base of layered oxides as pure Li-transition metal (M) oxides ($LiNiO_2$), or mixture of Ms as Li $(Ni_{1/3}Co_{1/3}Mn_{1/3})O_2$ known as NMC, also in different stoichiometry between the M.[7,22,29]

Further investigation of this material and the Li-substitution in layered oxides have led to the most recently and promising, Ni-rich layered oxides and Li-rich NMC layered oxides, known with different stoichiometry as High-Energy Nickel-Cobalt-Manganese oxides (HE-NCM).[7–9]

In fact, from 2003 with the introduction of thus Li-rich NMC from two independently groups Thackeray and Dahn the research is focusing on understanding the structure, the properties and the performance of this compound, that shows almost a double capacity of 280 mAh/g comparing to the one used from LCO.[30] However, a series of problem hinder the implementation of this cathode in practical and commercial cell. It shows a poor kinetics and voltage decay upon cycling. Even if the performance correlate to the extra capacity is easily reproducible, it is not enough to clarify the source of the problems and even if the research made great strides in understanding the structure and properties of the material, significant progress is required for the HE-NMC to become commercial viable.[7,8,29] The points including the voltage decay note also as voltage fade during cycling, high 1st cycle irreversible capacity loss (IRC), poor rate capability, and low volumetric energy density has to be overcome if it is wanted to introduce into the market.[7]

Another promising material is Ni-Rich materials also with a high discharge capacity 200-220 mAh/g, even if lower than the HE-NMC still with a significant improvement over the commercial LCO (140 mAh/g).[8,9] However, as HE-NMC the Ni-rich layered oxides have intrinsic problems like capacity fade, detrimental side reactions on the high cycling voltage, safety issues due to thermal runaway reactions and the challenge to maintain all the Ni in the 3^+ oxidation state, during synthesis.[7,9,22,29,31–33,34]

Even if, a lot of work and many papers can be found in the literature[32,35,36] on different studies about the advanced materials and basic layered oxides, a systematically way that starts with the basic understanding, in the class of normal layered oxides, of the correlation of the structure, composition and electrochemistry performance is missing.[7,29] Considering that in the advanced materials are present not only different M as Co, Ni and Mn, but also an excess of Li or Ni in the HE-NMC and Ni-rich, that influence all the properties during the working battery. In addition, the use of high voltage by itself is playing a crucial role on all components of the cell and elements in the cathode. As for all materials, surface and bulk properties has to be taken into account. For sure, surface chemistry can improve the properties inside of the battery, while the bulk properties are more challenging to clarify the structure of one compound.[7,18] Nevertheless, the surface itself has not direct influence on the bulk properties unless not during the combination with other processes that are taking place on the interface when the battery is working.[37,38]

2.2 Motivation

The present work focuses on the correlation of structural changes in layered oxides upon charge and discharge and the electrochemical performance of the materials, which varies a lot with the type of transition metals in the crystallographic structure. In particular, the aim will be to understand the role of cobalt and nickel in the basic layered oxides: $LiCoO_2$ (LCO), $LiNiO_2$ (LNO) and mixed structures as $LiNi_{1-x}Co_xO_2$ while special attention is paid on the disorder inside the material. To overcome the use of Co due to the high costs and the low capacity Ni or other elements like Al, Mn, Mg, Li are introduced[39,18] but a clear understanding of the function of each metal is missing. In addition, the knowledge obtained by investigating simple layered oxide can be used to build systems, which are more complex as HE-NCM. Even if the HE-NCM is a Li-rich material it can be seen as combination of different layered oxides and it will be useful to identify which cation is influencing the others in which way.

First, a suitable synthesis method has to be find from the literature which allows an accurate characterization of the morphology and crystallographic structure of the material.[23,35,36,40–50] Second part was focused on the electrochemical characterization with classical battery tests as rate capability and cycle life characterization. For being able to correlate the different properties of the material, structural changes and the electrochemistry, in-operando techniques were applied. In-situ X-ray diffraction (XRD) allowed the correlation of structural parameters with the electrochemical performance, while the On-line Electrochemical Mass Spectroscopy (OEMS) allows to monitor the gas evolution of the cathodes, which can occur as effect of structural changes in this family of cathode material.[51–54]

3 Used methods

3.1 Morphological analysis: Scanning Electron Microscopy (SEM)

The SEM permits information about the morphology, the particle size and the particle distribution of the synthesized material. In principle, an electronic microscope involves a scanning beam of electrons over a specimen and detects the signals, which are emitted. The main difference to an optic microscope resides from the wavelength of the electromagnetic radiation generated by the source which can give a higher resolution. The resolution can achieve the order of 2 nm in a high-resolution SEM. However, for the sample investigation the low resolution SEM was used in this work. For all samples, the images were taken with a Jeol SEM (JEOL, Tokyo, Japan, JED-2300 JCM-6000). The samples were prepared by pressing powder into a sticking copper tape which was placed on the SEM sample holder. For the investigation of the morphology, the SEM was operated at acceleration voltage of 10 or 15 kV, depending on the sample and the required resolution.[55]

3.2 TG/MS analysis

Thermogravimetric analysis to investigate the thermal behaviour of the samples was performed with a TGA/DSC1 STAR^e SYSTEM (Mettler Toledo, Switzerland), which is combined with a mass spectrometer (MS) as gas analysis system (Pfeiffer Vacuum, Germany). The measurements were performed in the temperature range of 25 °C – 900/1000 °C using Al_2O_3 crucibles in synthetic air or oxygen atmosphere at a heating rate of 10 K/min. The TGA connected with MS gas analysis system allows to identify the components from the decomposition of the investigated samples.

3.3 Surface analysis: BET

The Brunauer, Emmett and Teller (BET) theory is used as a standard procedure for the determination of the specific surface area of the synthesized materials. It can be used for a wide range of fine powders or porous materials and also to investigate the pore size distribution. The BET theory is based on an oversimplified model of multilayer adsorption and for these the reliability of the BET method is questionable unless certain conditions are fulfilled. The BET theory is somehow an extension of the Langmuir theory, which is valid only for a monolayer and is taking different hypothesis adapted for the multilayer adsorption into account. The main assumptions are that the gas is physically adsorbed on solids in layers without interaction between the layers so that the Langmuir theory can be applied to each layer.

The specific surface area of a powder is determined by the physical adsorption of a gas on the surface of the solid and by calculating the area from the amount of adsorbed gas assuming a monomolecular layer on the surface. Physical adsorption results from relatively weak forces (van der Waals forces) between the adsorbed gas molecules (N_2) and the adsorbent surface of the tested powder. The amount of gas V_a adsorbed on the sample with mass M_s, is dependent on the equilibrium pressure P, the temperature T and the nature of the gas-sample system, which has to be take into account for a BET analysis. The amount of gas adsorbed can be measured by a volumetric or continuous flow procedure, depending on the instrument. Usually, the data are treated according to the BET adsorption isotherm, Equation (8).

$$\frac{1}{[Va\left(\frac{P0}{P}-1\right)]} = \frac{C-1}{VmC} \times \frac{P}{P0} + \frac{1}{VmC} \tag{8}$$

Here P and P_o are the equilibrium and the saturation pressure of adsorbates at the temperature of adsorption, V_a is the volume of the adsorbed gas quantity, and V_m is the quantity of the gas for one monolayer adsorbed. *C* is a BET constant expressed as:

$$c = exp^{\left(\frac{E1-El}{RT}\right)} \tag{9}$$

Where E_1 and E_l are the heat of adsorption equal to the one of liquefaction for the first layer and for the second or higher, respectively. On this bases, the BET plot consists in having on the x axis the ratio (P/P_0) and on the y axis the left terms of Equation 6, this correlation gives a linear dependent plot, valid in the range of $0.05 < P/P_0 < 0.35$. The slope (s) and the intercept (i) of this linear plot are used to calculate the Volume of the adsorbed gas V_m for a monolayer and c as shown by Equation (15).

$$Vm = \frac{1}{s+i}\ ,\ \ c = 1 + \frac{s}{i} \tag{10}$$

Knowing these 2 parameters, the specific surface area of the material can be calculated with the mass of the sample. In this way, the total surface area (S_t) and specific surface area BET (S_{BET}) are expressed by Equations (11)and (12).

$$St = \frac{(VmNs)}{Va} \tag{11}$$

$$\text{Sbet} = \frac{St}{M_S} \tag{12}$$

Here N is Avogadro´s number, s the adsorption cross section of the particles, V_a the molar volume of the adsorbate gas, and M_S the mass of the sample. The measurements were

performed using N_2 as adsorbed gas with a Quantachrome Autosorb iQ. The determination was carried out at the temperature of liquid nitrogen (77 K) as usually done for the measurement.

The accurately weighed powder was placed in a glass tube with a glass filler road to reduce the dead volume for increasing the precision of the measurement. Before starting with the adsorption on the sample, it is necessary to remove gasses and vapours that may have become physically adsorbed onto the surface after synthesis, during treatment, handling or storage.

The outgassing conditions are critical for obtaining the required precision and accuracy of specific surface area measurements. The outgassing conditions defined by the temperature, pressure, and time are chosen so that the original surface of the solid is not influenced. In fact, in case of a not complete outgassing, the specific surface area may be reduced or may be changed because an intermediate area of the surface is covered with molecules of the previously adsorbed gases or vapours.

In addition, the outgassing condition has to yield to reproducible BET plots and no detectable physical or chemical changes in the powder.

The Nitrogen adsorption was done with a multipoint measurement, in particular 11 points, and for each point was the specific surface area of the sample evaluated.

In addition, the BET theory allows estimating the particle size. It is based on the hypothesis that the particles are spherical with a volume V and surface S of a ball.

$$V = \frac{4}{3}\,\pi r^3 \quad , \quad S = 4\pi r^2 \tag{13}$$

By this the particle size d can be calculated from the specific BET area of the sample according to Equation (14).

$$d = \frac{6}{BET \times \varrho} \tag{14}$$

3.4 Bulk structural analysis: X-ray powder diffraction (XRD) and Rietveld refinement

X-ray powder diffraction (XRD) is a rapid “bulk” analytical technique that provides information about the structure in crystalline materials, which is used for phase identification of crystalline material and can provide information on unit cell dimensions with an appropriate treatment of the data. It is also one of the few techniques that can identify the position and occupancy of the ions incorporated into the molecular structure.

A cathode X-ray tube is used and the generated radiation is filtered to produce monochromatic radiation, collimated to concentrate, and directed toward the sample. The interaction of the incident rays with the sample produces constructive interference (and a diffracted ray) when conditions satisfy Bragg's Law as shown in Figure 7 and Equation (15).

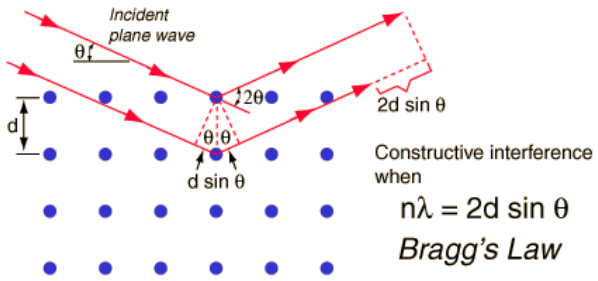

Figure 7: Bragg condition, showing constructive interference.[56]

$$n\lambda = 2dsin\theta \tag{15}$$

With n the integer, λ the wavelength of the incident X-Ray beam, d the space between atomic layers in the crystal and θ is the angle of the incidence of the X-Rays.

This law relates the wavelength of electromagnetic radiation to the diffraction angle and the lattice spacing in a crystalline sample. These diffracted X-rays are then detected, processed and counted. By scanning the sample through a range of 2θ angles, all possible diffraction directions of the lattice should be attained due to the random orientation of the powdered material. Conversion of the diffraction peaks to d spacing allows identification of the material because each crystalline material has a set of unique data. Typically, this is achieved by comparison of d spacing with standard reference patterns from the ICDD library.[57] XRD can be applied to powders or single crystals, which need different instruments. It is important to underline that an accurate collection of the diffracted X-rays and the sample preparation is necessary.

Different modes of data collection are used, mostly the transmission and Debye-Scherer geometry. The transmission mode is more suitable for the in-situ measurements.

On the other part the Debye-Scherer is more suitable for the powder. It is necessary to be careful at the geometry of the diffractometer, the calibration and the quality of the instrument alignment.

A crystalline compound, analysed with XRD, gives a diffraction pattern consisting of well-defined, narrow, sharp and significant peaks.

The powder material is usually finely ground, homogenized, and an average bulk is measured. From this the crystallinity of the powder can be determined by comparing the integrated intensity of the background pattern to that of the measurement.

The phases and structures of the crystals were identified using X-ray diffraction analysis performed with a STOE STADIP diffractometer (STOE, Germany) using Mo $K\alpha_1$ radiation (λ = 0.70932 Å, 50 kV, 40 mA) and a Mythen 1K detector. The diffraction patterns for the crystalline powders were collected with a capillary (0.3 mm) in a Debye-Scherer mode. Regarding the 2Θ range, two different data sets were collected; one from 3-40 ° with a step size of 0.015 ° and measurement time of 240 s/step for 20 min measurement for all samples and 3-60 ° with a step size of 0.015 ° and measurement time of 7 s/step for overnight measurements for samples without impurity and side phase. All measurements were compared with the ICCD library for checking the synthesized phase of the sample.

The accurate collection of the data in Debye Scherer mode are important also for the subsequent treatment of the Rietveld Refinement, which is performed with the Fullprof software package.[58]

With a Rietveld treatment of the data, it can be deduced a significant amount of information from the sample. Performing a Rietveld Refinement requires usually a known crystal structure and parameters of the instrument. In order to have the information from the Rietveld Refinement a model is used to analyse the pattern. In fact, Rietveld Refinement provides results on a model and for fitting the experimental results, different strategies for refinement can be found with an accurate evaluation of the convergence to avoid wrong interpretation of the data. Mainly, the structural phase of the crystals, with lattice parameter, volume of the cell, occupancy of the atoms in the unit cell and information related to our purpose can be identified.

The Refinement Strategy, used for the XRD pattern, will be described in details during the analysis of the pattern for the samples.

3.5 Ink preparation and coating

To prepare the electrodes, it is necessary to make a slurry of active material (AM), conductive additives and a binding agent, which is then coated on Cu or Al foil for anodes or cathodes. The inks for comparing the performance of all the synthesized materials contained 80 % AM, which were tested in Swagelok cells, while for the in situ XRD (see chapter 3.8.1) electrodes with 92 % AM were made to get good patterns from the material.

For all tested AM carbon black (Super C65, TIMCAL, Switzerland) was used as conductive additive and PVdF (Polyvinylidene-difluoride, Kynar HSV 900, Arkema, France) was used as binder. All the ingredients were dispersed in N-methyl-2-pyrrolidone (NMP, Sigma Aldrich, Germany) and put in a planetary centrifugal mixer (Thinky, USA). The NMP was added step-by-step to the solids and mixed. For different requirements to the ink different compositions were prepared, depending on the use of the electrode. All the slurries were mixed in a four step procedure, where first hundred percent of the solid content were mixed for 2 min at 1000 rpm. Afterwards a third of NMP was added and mixed for 5 min at 2000 rpm two times. In between all the steps the homogeneity and the viscosity of the ink were checked. After the third addition of NMP the ink was mixed 10 min at 2000 rpm also to degas the ink for getting a homogeneous coating.

The resulting viscous slurry with a solid content of 55 $\%_{wt}$ was maintained and was cast onto a thin aluminium foil (MTI corporation USA, 18 µm), using a doctor blade (RK Print Coat Instruments, UK). After drying at 55°C for 2h in a self-made drying oven, electrodes with 10 mm diameter were punched and then dried at 120 °C overnight under vacuum in a glass oven (Büchi oven 585, Switzerland).

For AM which is showing agglomerates, a ball mill (Fritsch, Pulverisette 7 Premium Line) was used to mix the AM, SuperC65 and Binder with NMP in the same composition. For this a 20 ml ZrO_2 jar war used with 10 balls of 10 mm diameter for ensuring the grinding function of the ball mill. The powders were added on top of the balls and all the NMP was added in one step. The ink was then mixed at 180 rpm for 1 h. After this procedure, the ink was coated on the Al-foil and dried identical to the process for the ink produced with the planetary mixer.

For the OEMS measurement (3.8.2), the inks were prepared using also the planetary mixer in several steps, with the different ratio of 96 %wt of AM, 2 %wt of Super C65 conductive carbon and 2 %wt of PVDF with NMP. The very viscous slurry was coated on a stainless-steel mesh (SS) (The Mesh Company Ltd, UK, SS316, aperture 26 µm, wire diameter 25 µm) for gas permeation for the OEMS measurement.

3.6 T-cell assembling

Swagelok T-cells (Figure 8 a) were assembled in an argon filled glove-box (MBraun, Germany, H_2O and O_2 < 0.1 ppm,) using two glass fibre separators (VWR, Germany, glass microfiber filter, 691) and 180 µL of LP57 electrolyte (1 M $LiPF_6$ in EC:EMC 3:7 %wt, < 20 ppm H_2O,

BASF, Germany). For three-electrodes measurements (Figure 8 b), a metal lithium foil (450 µm thickness, Rockwood Lithium, USA) was used, as counter and reference electrode.

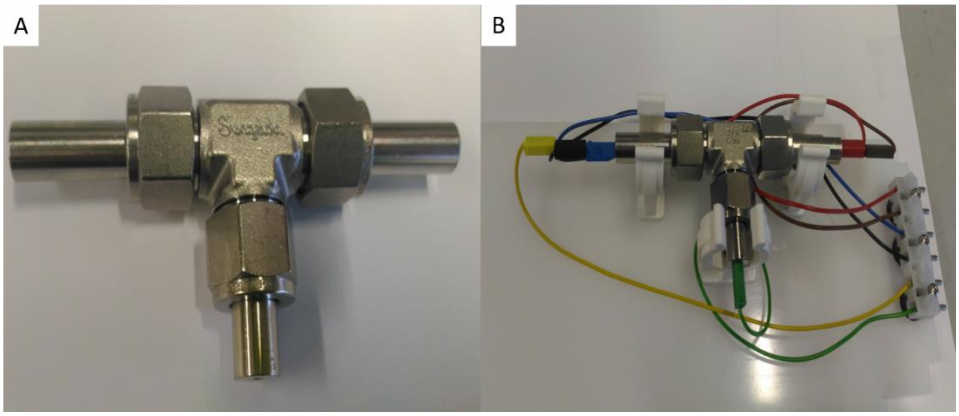

Figure 8: Swagelok cell (A) and connection in three-electrode set-up (B)

Electrochemical tests as C-rate and life-time characterizations, (described in the next subchapter) were carried out in a climatic chamber at 25 °C (Binder, Germany) using a battery cycler (Maccor, USA, Series 4000).

3.7 C-rate and life test characterization

The rate capability test determines the specific capacity of the AM at different C rate with charge-discharge cycles of the cell. The C rate is the electrical current that is imposed to the cell, where 1C is the current which charges or discharges the theoretical capacity of the cell within 1 h. If the cell is cycled at C/10, the current would be a factor 10 less, by 10C the current would be a factor 10 higher.

For having a good electrochemical characterization of the material in terms of capacity and its behaviour during cycling, different C-rates have to be investigated. For this, 3 cycles of C/10 were applied to the battery followed by 3 cycles of C/5, C/2, 1C and 2C. After this a cycle test was performed with 200 cycles at C/2.

The measured capacities were normalized to the active material of the electrode.

3.8 In situ-operando techniques

3.8.1 In situ-XRD

The XRD is a suitable technique for understanding the structure of various materials. Due to the availability of better X-ray source, with high resolution, the importance was increased. However, even if it was already used for the characterization of battery materials for a long

time, the challenge started again with the possibility to have a cell that allows the structural characterization of the materials during the charge and discharge of it. In this way, the problems of ex-situ measurements, like during disassembling the cell, air contact or relaxation processes, are overcome.[53] In the case of combination of the electrochemical characterization with the XRD, the degree of lithiation of the material can be controlled and the changes in the structure of the active material can be monitored simultaneously.

Obviously, the synergy of both technique leads to a detailed investigation, however there are problems regarding the correlation of data from different instruments and it has to be taken into consideration that the variation of the structure due to cycling the cell during the recording of the XRD pattern might be an issue.[52–54]

In this case the in-situ XRD pattern are collected in the transmission mode with a sample holder developed at the Chair of Technical Electrochemistry (TEC) at Technical University Munich, which can be used with the XRD instrument in the lab, as shown in Figure A and B.[16] The cells for this sample holder are pouch cells, which are built in a bag of a propylene coated aluminium foil. The electrodes are cut with a size of 3 cm x 3 cm. The separators (Celgard C2325) were cut with a size of 3.5 cm x 3.5 cm (bigger than the cathode to ensure the isolation between cathode and anode).

The pouch cells were preassembled outside of the glovebox, After the partial assembling outside, the setup was dried in the glass oven overnight at 90°C under vacuum. The final assembling was done in the glovebox, with a lithium metallic foil as negative electrode, cut in the size of 3.5 cm x 3.5 cm, filled with 700 µL of LP57 electrolyte and finally sealed in a vacuum chamber sealing device (C100, Multivac) applying a vacuum of 50 mbar.

The pouch cell was put in the sample holder for the XRD measurement and connected for charge and discharge to a potentiostat (Biologic, VMP-200).

For the in situ XRD measurements a pouch cell was built which contained a cathode with 92 wt% AM, 4 wt% PVdF binder and 4 wt% Super C65 conductive carbon. Two Celgard separators (500 µm thickness each) soaked with 700 µl electrolyte (LP57) and lithium metal foil (Rockwood Lithium, 450 µm thickness) as anode were used.

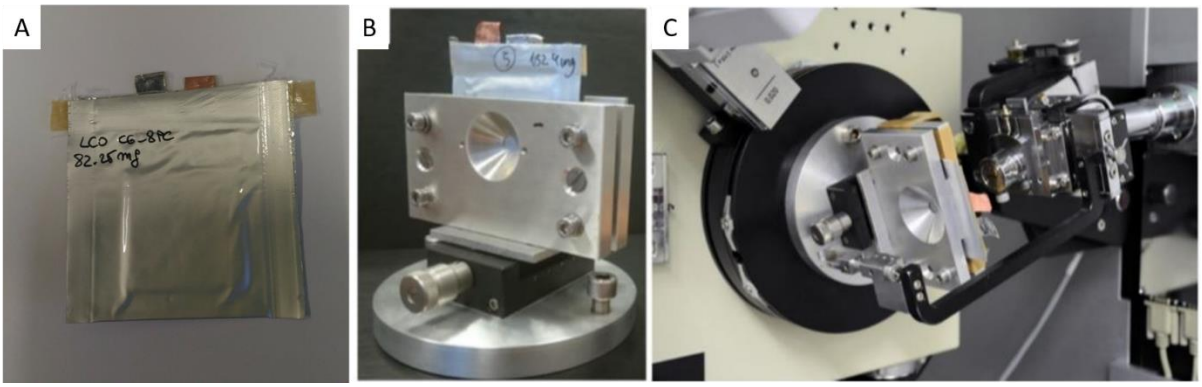

Figure 9: A; Pouch cell design, B; Device for mounting the pouch cell for the STOE STADI P diffractometer in transmission mode and C; mounted pouch cell on the STOE STADI P diffractometer.

The XRD pattern were recorded in transmission mode with a wavelength of $\lambda = 0.70930$ (Mo Kα source). For all LMO_2-lithium cell, the XRD scans were performed between 7.000 - 44.965 of 2θ with a step size of 0.015 ° and a step time of 4 s, which resulted in 42 min for each recorded pattern.

3.8.2 On-line Electrochemical Mass Spectrometry (OEMS) and OEMS-cell assembling

Mass Spectrometry (MS) is a powerful technique based mainly on the measurement of the ratio of mass to charge (m/z) that is specific for each molecule due to the fragmentation of the molecule. The fragments are ionized for being able to be measured. A typical mass spectrum is an intensity plotted versus m/z-values and is used usually in combination with other instruments depending on the aim of the analysis. On-line Electrochemical Mass Spectrometry (OEMS) was used for the first time in the battery characterization by the Technical Electrochemistry Munich, where the setup was designed and improved since 2012 for battery operation.[59–61] With the OEMS the gas evolution in the cell can be monitored in operando during cycling the cell. The Figure 10 illustrates the set-up of the OEMS system developed by Tsiouvaras et al.[59] The design of this Mass Spectrometry consists in a single stage pressure reduction from ambient pressure to the high vacuum required by the MS (Pfeiffer Vacuum, QMA 410). The measurements of the gas evolution during the operation of the cell can be done with the special cell shown in Figure 11 designed in the same group.

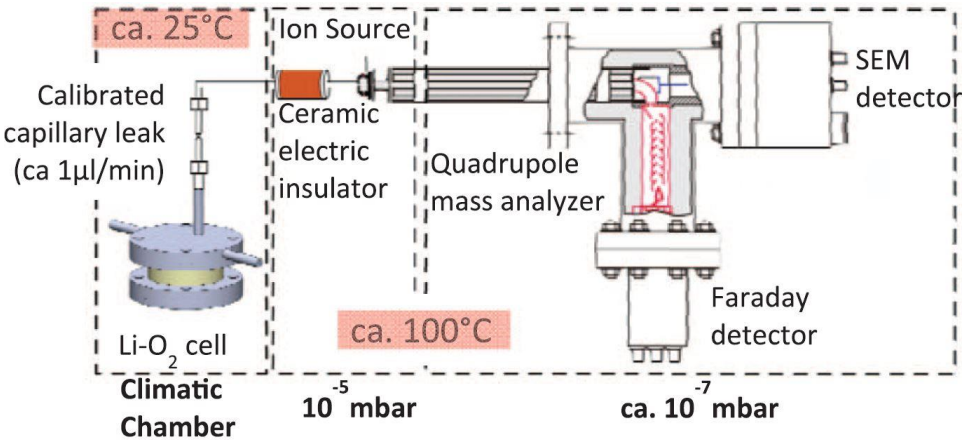

Figure 10: On-line electrochemical mass spectrometer (OEMS) system. Developed at TEC by Tsiouvaras et al.[59]

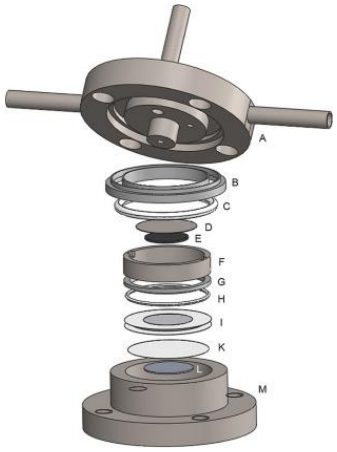

Figure 11: Isometric view of the sealed two-compartment OEMS cell from Metzger et al.[61]

The sampling of the gas is done by sampling the cell headspace at an established flow rate of 1 µL/min through a calibrated crimped-capillary. The setup allows a fast time of response in the order of seconds, which allows to correlate the evolution of gasses with the potential of the cell. The inlet is guided using a tube directly into a differentially pumped cross-beam ionization chamber. Usually the working pressure in the ionization chamber is $1*10^{-6}$ mbar and $1*10^{-7}$ mbar at the Secondary Electron Multiplier of the MS, this allows the quantification in the order of ppm-level for the evolved gasses.

The cells were assembled in an Argon-filled glove box in different steps; putting a 17 mm diameter lithium foil as negative electrode on the lower part of the cell (Figure 11) put 20 µL of electrolyte LP57 and add 2 porous polyolefin separators with 20 mm diameter (Celgard, USA, H2013) with 2 times 20 µL electrolyte. On this the AM electrode, which was coated on a mesh of 15 mm diameter was added and soaked with 40 µL of LP57. A stainless steel mesh

(The Mesh Company (Warrington) Ltd) was placed on the cathode for distributing the pressure of a compressed spring.

Once assembled the cell was connected to the OEMS. Before starting the measurement, the head space of the OEMS was purged for 2 min with argon to remove the glovebox atmosphere and to flush the connection of the cell to the OEMS.

A 4 h OCV step was applied before starting the charge of the cell with C/10 with a potentiostat (Gamry, Series G300) in a climatic chamber (Binder, KB23) at 25 °C.

All the gas analysis were normalized to the m/z-Signal 36, which is an Ar isotope.

4 Synthesis of $LiCoO_2$ and characterization

$LiCoO_2$ is widely used as a commercial cathode material.[18] However, different aspects of this material have to be taken into account. Overall $LiCoO_2$ samples are varying in structure, stoichiometry or morphology due to small changes of the synthesis conditions. In literature $LiCoO_2$ with a hexagonal cell (space group R-3m) is reported to be the most suitable material for battery application. The prototype for this kind of structure is known to be a α-$NaFeO_2$ structure. Subsequently 3 different routes of synthesis for LCO will be shown and by this an easy adjustable method for all layered oxides (LNO, LNCO) will be identified.

4.1 Flux method

It was recently reported, that the flux growth method can lead to the preparation of high-quality layered oxides for lithium ion batteries.[42] The flux growth method is up to now the only way to obtain singles crystals without any thermal strain or defects from the liquid phase. It utilizes a high-temperature melt of inorganic salts as the solvent for the crystallization.[62] Although the flux growth method is reported for one-dimensional LCO single crystals, it was tried out to enforce this approach for our synthesis, which should result in crystalline powder.[42]

In a typical flux growth synthesis, all solids are mixed delicately for 30 minutes using an agate mortar. As precursors for Co and Li, Co_3O_4 and $LiOH{\cdot}H_2O$ were used respectively, purchased by Sigma Aldrich (99.995%). NaCl (Sigma Aldrich, 99.99%) flux growth was performed and it was ensured that the concentration of Co is 5 mol Wt%. The molar ratio of Co_3O_4 and $LiOH{\cdot}H_2O$ was 1:2. The excess of the Li is necessary due to the volatility at high temperature.[62] The homogeneous mixture was placed in an open Al_3O_4 crucible and annealed in a tube furnace with synthetic air. According to Zettsu et al.[42] the final temperature was 900 °C which was hold for 5 h. After annealing the crucible was cooled down to 500 °C at a rate of 200 K/h and afterwards to room temperature with the natural cooling rate of the furnace.[42] The temperature program is shown in Figure 12. After annealing, the crystals were separated and washed from the flux mixture with warm water to remove the NaCl. The samples were dried in a vacuum oven at 70 °C.

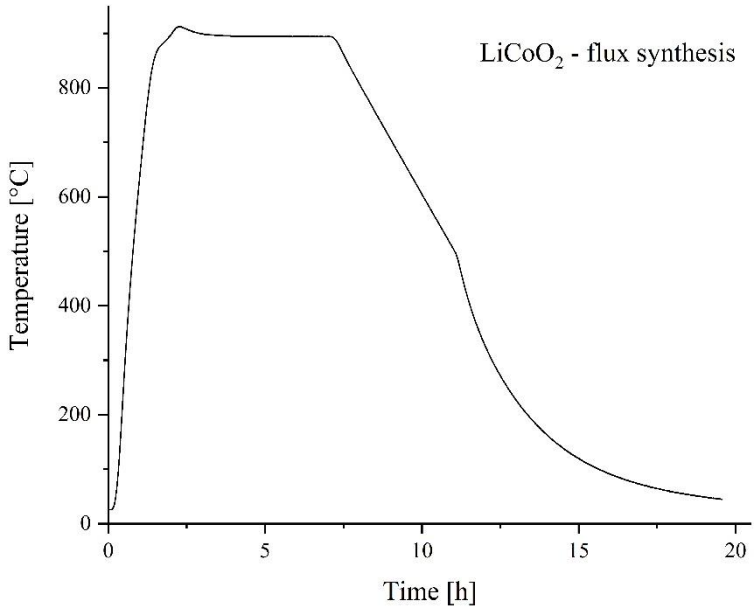

Figure 12: Temperature procedure for the LiCoO2 via flux growth synthesis.

The morphology and average size of the $LiCoO_2$ crystals were characterized with SEM Figure 13, which displays the as-obtained $LiCoO_2$. From this the morphology and different shape of the synthesized particles can be seen. The SEM pictures show hexagonal particles with different sizes, from 5 to 10 µm.

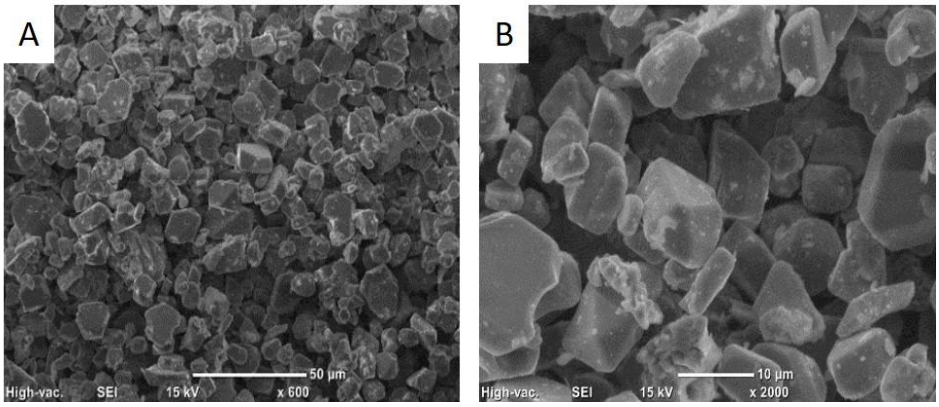

Figure 13: SEM picture of the LiCoO2 powders obtained with flux growth synthesis after annealing at 900 °C. Particle size in the range of 5-10µm.

Figure 14 shows the XRD profiles of the as-obtained powder. For identification of the phase and to check for crystalline side phases or the presence of impurities first the ICCD database was used. The pattern was checked for $LiCoO_2$ and/or Co_3O_4 before performing a detailed analysis of the XRD pattern with a Rietveld refinement.

All diffraction lines are in agreement with the ICCD data (PDF 75-0532) for $LiCoO_2$. However, some diffraction lines agree with Co_3O_4 (ICCD data PDF 00-42-1467), with a main characteristic peak at 15 2θ (see Figure 14). Presence of Co_3O_4 might be due to a not complete

dissolution in NaCl or even a decomposition of $LiCoO_2$, even if it is reported to be stable at high temperature.[36]

In addition, the NaCl flux created problems with the quartz tube due to the open crucible in the tube furnace because of the volatility of Li. Another problem might be the evaporation of NaCl as it is in a continuous flux. Due to this, the flux growth synthesis was not continued. Moreover, the unlike spinning of the NaCl, that cannot be controlled in this synthesis, leads to a not homogeneous particles size distribution or a phase pure product. Overall, it was decided to use another method, where the control of synthesis is more reproducible and which will lead to a phase pure product with small particles.

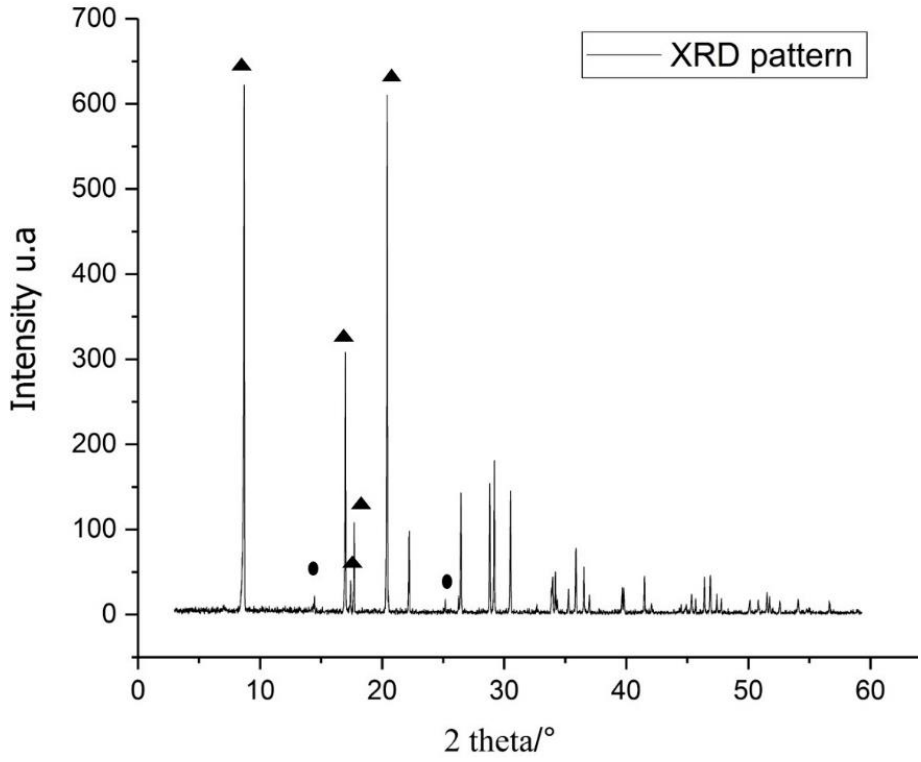

Figure 14: X-ray diffraction (XRD) pattern of powders registered with Mo ($K\alpha_1$,λ=0.70931Å) as-obtained by the flux-growth method. Analysis shows the presence of LiCoO2 (▲) and impurity of Co3O4(●).

4.2 Sol-gel-ethylene glycol

According to Peng et al. and also supported by different literature, a sol-gel synthesis route is suitable for the control of the crystallographic structure and to obtain a phase pure LCO.[63] In this literature this synthesis route is identified as the best for getting the requested properties for a good cathode material. Further it is reported to obtain small and homogeneous particles with a narrow particle size distribution. In the synthesis, the transition metals and the lithium ions are first embedded in a polymer matrix to ensure a homogenous and distribution which

helps to gain the right stoichiometry. Usually for these kind of synthesis nitrates or acetates are used as source for the transition metals (M) and Li. As in the Peng paper, it was decided to use acetates instead of nitrates, which are more environmental friendly. The nitrates are a source of NO_x during the annealing.[48] Ethylene glycol was used for dissolving both precursors and the complexing agent. Different experiments were conducted with the procedure described in details below.

$Co(CH_3COO)_2*4H_2O$ (Merckmillipore, >99.0%) and $Li(CH_3COO)$ (Sigma Aldrich, 99,99%) were used in an atom ratio of 1 : 1 (Co : Li) and Citric Acid (CA) (Sigma Aldrich, >99.5 %) to Ethylene Glycol (EG) (Sigma Aldrich, ρ= 1.113 g/mL, 99.8 %) in a ratio of 1:7. First, the CA was dissolved in EG and subsequently the Co and Li precursor were added. The total molar ratio for Co, Li and CA was 1 : 1 : 1. The solution was heated up to 140 °C under stirring to form a gel.

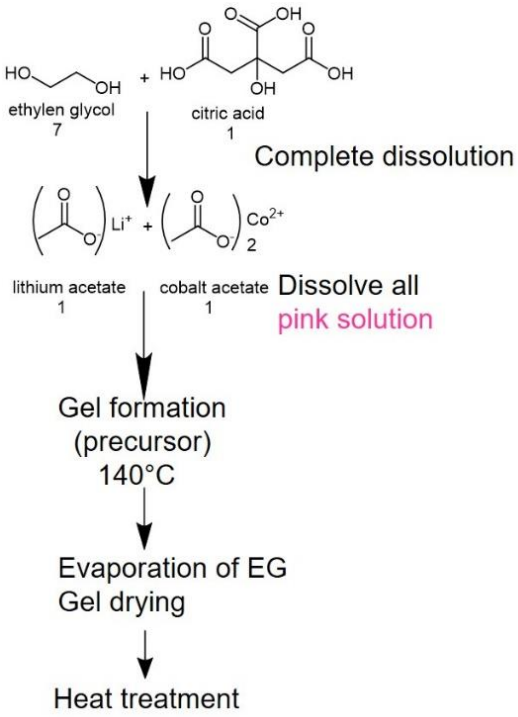

Figure 15. Schematic process for the LiCoO2 synthesis via sol-gel using ethylene glycol as solvent.

From a pink mixture at the beginning, the colour changed to purple with a gel consistence during the heating process. However, the gel was not homogeneous. It was assumed that the solvent was not enough as reported in the paper.[41] From the qualitative analysis and SEM pictures it can be observed that the gel from the first two samples in Figure 16 (A and B) were not suitable for performing the heat treatment. The third sample (with EG : CA of ratio of 20 : 1) was looking more or less homogenous enough to carry out the heat treatment, which

was done in a small quantity just to identify if the gel formation was fine. The gel was vacuum dried at 180°C to obtain an organic polymer foam. The SEM images (Figure 16 C) of the gel precursors show the frame of a polymer with a homogeneous distribution. Anyway, from the SEM picture the final results for the LCO cannot be predicted.

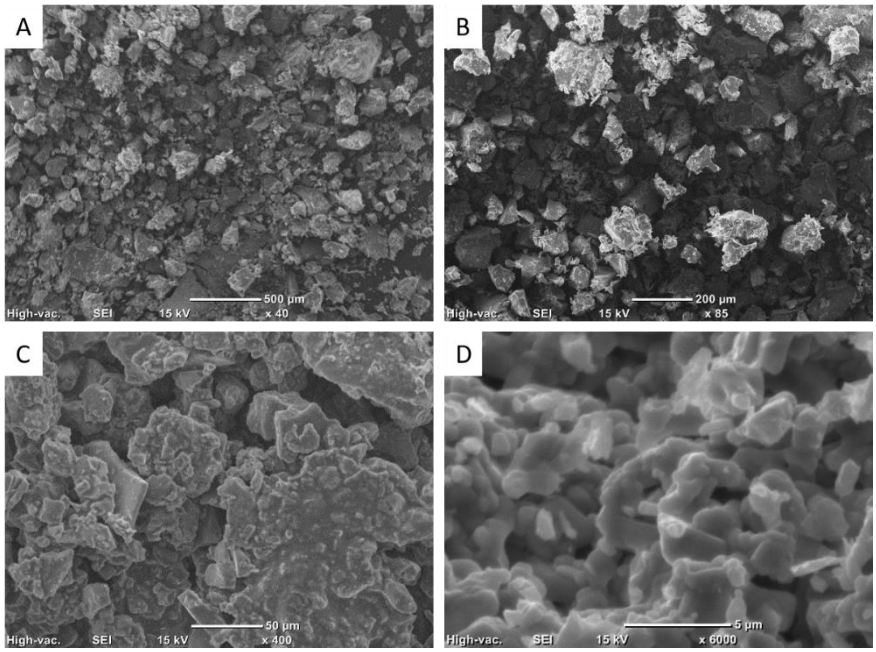

Figure 16: SEM images via sol-gel in EG, precursors of LiCoO2, A, B: 1st and 2nd batch of synthesis, C, D: 3rd batch of synthesis precursor and powder after calcination at 750 °C respectively.

The $LiCoO_2$ was produced by calcining the precursors in synthetic air at 750 °C as suggested by Peng et al.[41] Figure 17 shows the TGA data and the MS results of the gel precursor. The weight loss of the gel terminated at 400 °C and two discrete weight-loss regions occur at 90-190 °C and 270-400 °C. From the TGA/MS-results it can be deduced that the weight loss in the first temperature range corresponds to the removal of superficial ethylene glycol of the gel precursor and the second to the decomposition of the chelated precursors. It can be identified form the decomposition products Figure 17. The SEM picture (Figure 16 D) of the calcined LCO shows a narrow particle size distribution with an average size less than 2 µm.

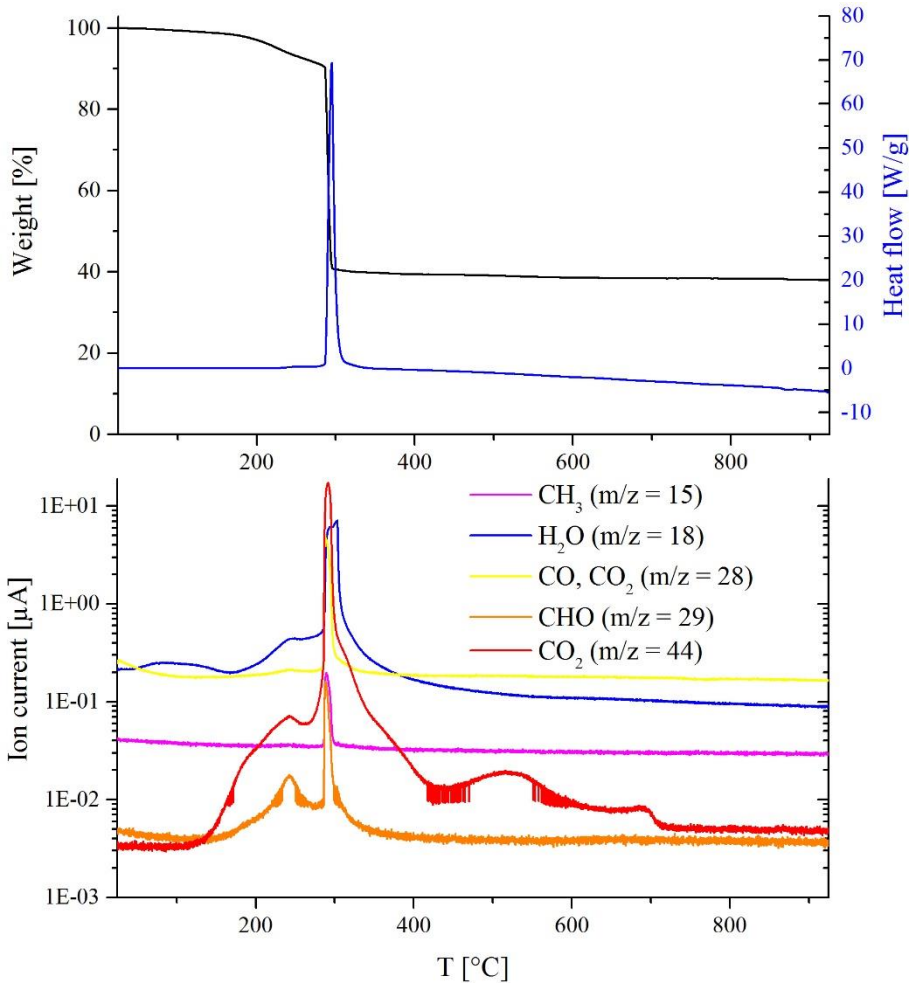

Figure 17 Thermogravimetric analyses and mass spectrometric (TGA-MS) of the $LiCoO_2$ gel precursor at a heating rate of 10 °K/min.

Figure 18 shows the XRD patterns for the LCO powder calcined at 750°C. The pattern shows the presence of a dominant rhombohedral LCO-phase as main compound, but the presence of Co_3O_4 as impurity can still be noticed around 15° (2θ) with a significant intensity. The presence of Co_3O_4 might be due to the volatility of Li at high-temperature, as this Li deficiency could let the cobalt oxides stay unreacted once it is formed.[36] To result in a phase pure sample without impurities, it should be tested to increase the Li amount during the gel formation, but due to the long evaporation of EG at relatively high temperature, a different solvent is tested. In fact EG is an organic viscous solvent in which the dissolution of the educts takes long or require a significant amount of solvent. Therefore, the evaporation time is by far too much.

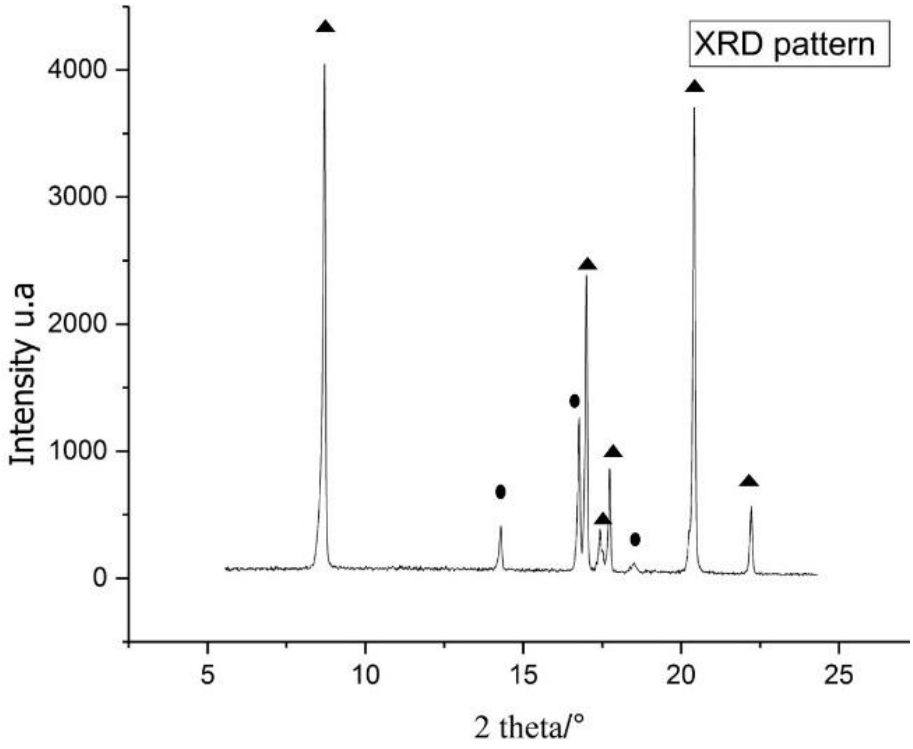

Figure 18: XRD-pattern of LCO, Mo ($K\alpha_1$,λ=0.70931Å) (▲LiCoO2 pattern) and (● Co3O4 impurity), synthesized via sol-gel with ethylene glycol as solvent.

4.3 Sol-gel-water

To overcome the issues of EG, which were described in chapter 4.2, water was used as solvent. In fact, Predoana et al reported in details the gelling process with water as solvent.[44,45,64] LCO was prepared from the gel precursor obtained by the sol-gel method in aqueous media, as shown in Figure 19. Although studies with nitrates and acetates are described in literature, for comparison reasons the same acetate precursors were used as for the previous sol gel synthesis. $Li(CH_3COO)$ and $Co(CH_3COO)_2*4H_2O$ were used in an atom ratio of 1.1 : 1 as metal oxide source while Citric acid (CA) was used in a molar ratio of 1 to the Co as chelating agent. The aqueous solutions of Li- and Co-salts (0.25 mol/L) was prepared first and the CA was added afterwards. The mixture was stirred until the solvents were totally dissolved and a clear solution was obtained. While stirring, the pH was corrected for keeping the metals diluted. The initial pH of the mixture was 8, which changed to pH = 5.5 when the CA was added and corrected to pH = 6 by adding ammonium hydroxide solution (1M NH_3 in H_2O). Afterwards the solution was heated up to 80 °C for the gelation process. The gelation occurred after some hours depending on the quantity of the solvent used and the obtained gel was hold at 80 °C until it was completely dry. Afterwards it was stored at 70 °C to be kept dry. To ensure the

homogeneity of the powders during the thermal treatment, the dry gel was ground in an agate mortar and put in an Al_2O_3 crucible.

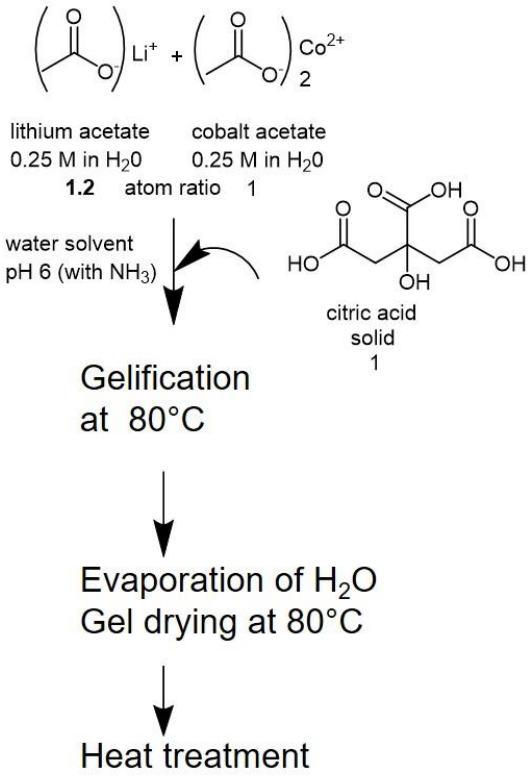

Figure 19:Schematic representation for the $LiCoO_2$ synthesis via sol-gel using water as solvent.[45]

LCO was obtained by thermal treatment of the so prepared gel following the procedure with reported by Pedroana et al.[44]shown in Figure 20 The annealing was started with a heating rate of 1 K/min up to 400 °C followed by a1 h hold at this temperature to remove all the chelating agent; then the sample was heated up to 700 °C with 5 K/min and was hold at this temperature for 6 h. The heat treatment was performed in a static synthetic air atmosphere.

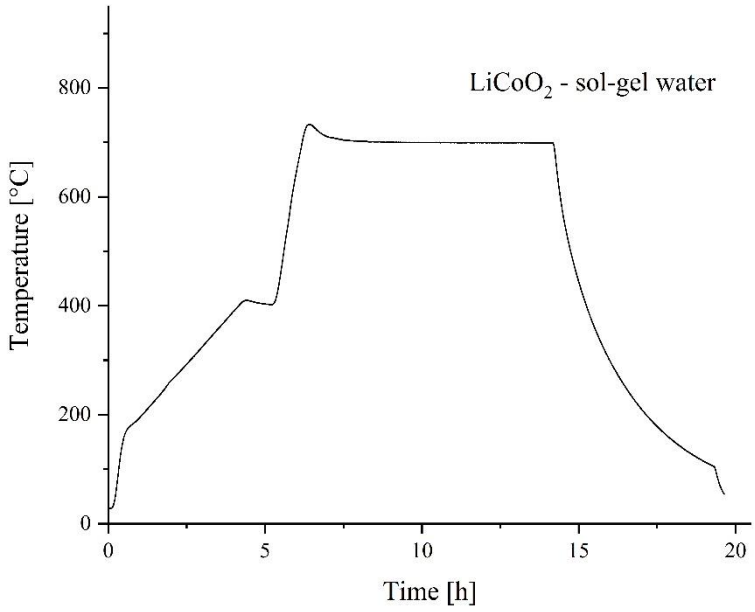

Figure 20: Annealing treatment for the $LiCoO_2$ precursor with 1 K/min up to 400 °C and 5 K/min up to 700 °C in a static synthetic air atmosphere.

The XRD pattern of the obtained LCO-powder in Figure 21 A shows a good crystallinity. However, Co_3O_4 is still present as a side phase. The stoichiometry of the sample was identified by phase-matching with ICSD data base to be $Li_{0.94}CoO_2$ comparing with the ICDD data (PDF-. As a consequence of the lack of Li it was decided to increase the ratio of Li:Co in the precursors to 1.2 : 1. As a result, the XRD pattern in the Figure 21 B shows that the stoichiometric $LiCoO_2$ was obtained.

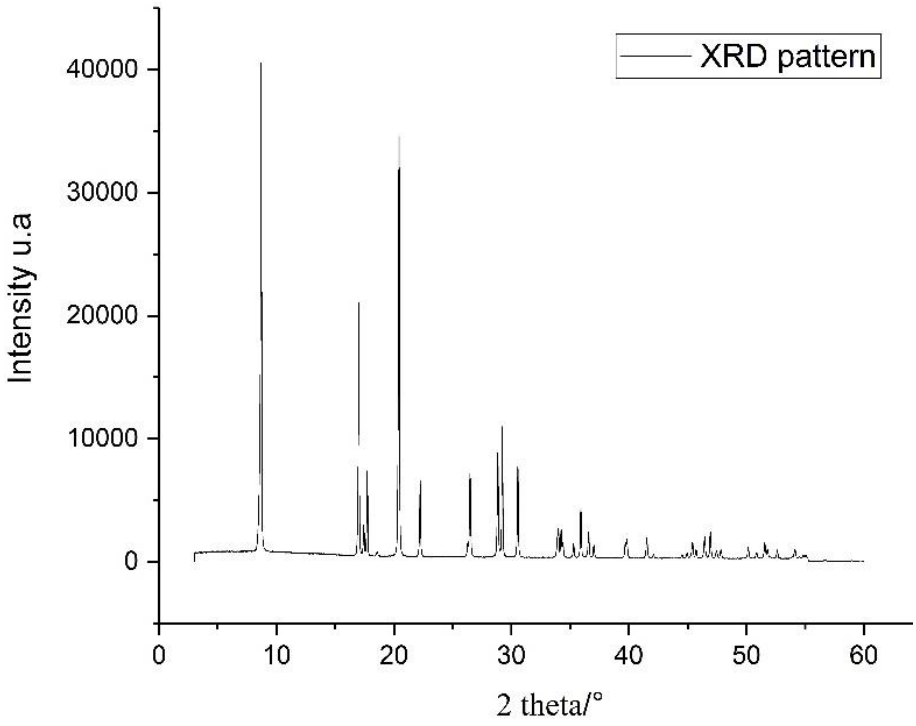

Figure 21: X-ray diffraction (XRD) pattern registered with Mo ($K\alpha_1$,λ=0.70931Å) of LCO powders as-obtained by the sol gel water method with the Li:Co of 1.2:1. No impurity is noticed.

The SEM pictures in Figure 22 show the gel morphology before annealing (A) and after annealing (B). Primary particles of the LCO powder (Figure 22 B) cannot be completely distinguished due to the low resolution of the SEM. In addition, the range of the particle size can be determined despite the agglomerates of primary particles. By counting a significant number of particles in the SEM picture it is deduced to be between 2 and 5 µm. To ensure that this result is reliable, the specific surface of the LCO was measured with BET and an average particle size was calculated with the assumption of spherical particles, as described in the chapter 2.3. This resulted in an average particle size of 3 µm.

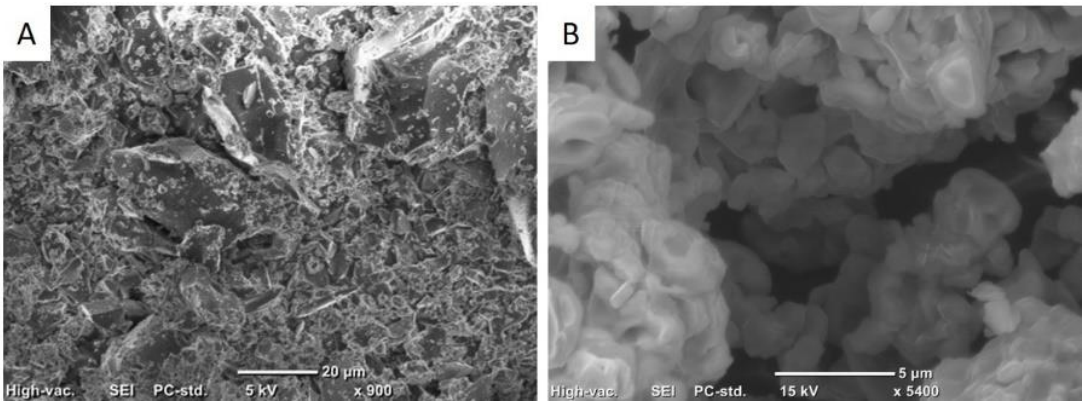

Figure 22: SEM pictures for $LiCoO_2$, A before annealing, polymer frame and B, powders after calcination.

The BET, surface area as described in the chapter 2.3 for the LCO was identified to be 0.4 m^2/g. Considering the good control of the gel formation and the obtained phase pure material it was decided to continue with this method for other layered oxides. Therefore, sol-gel-water method was applied further for other layered oxides, even if attention has to be payed to the used atmosphere. In addition it is reported in the literature to work well for different mixed layered oxides.[23,65]

After the successful synthesis of LCO, the scale up of the synthesis has to be investigated for being able to continue with the electrochemical characterization, for which a significant amount of LCO is needed. Usually the scale up of aqueous synthesis should not be problematic in a laboratory scale, but the sol gel synthesis has the problem of temperature control once the gel starts to be formed. This results in a not perfect homogeneity during the drying process and subsequently in a not perfect distribution of elements in the gel. Additionally, the formation of side phases of cobaltoxides was a problem because of the scale up of a factor of 10, even if an excess of lithium for ensuring the stoichiometry was used (from sample LCO-3-2 to LCO-3-3, Appendix 12.1). Obviously, the surface of the vessel was increased and the temperature was kept constant during all the gelification process. The formation of the gel was observed as for the sample before. From the TGA/MS measurement (Figure 23) and SEM picture (Figure 24) of the dried gels of the two different synthesis no significant difference can be observed.

The TGA/MS shows for both gels the decomposition between 300-410 °C, mainly with the evolution of CO_2 and H_2O which is in accordance with the mentioned paper from Pedroana et al. which shows the reaction and decomposition of the gel during the annealing procedure.

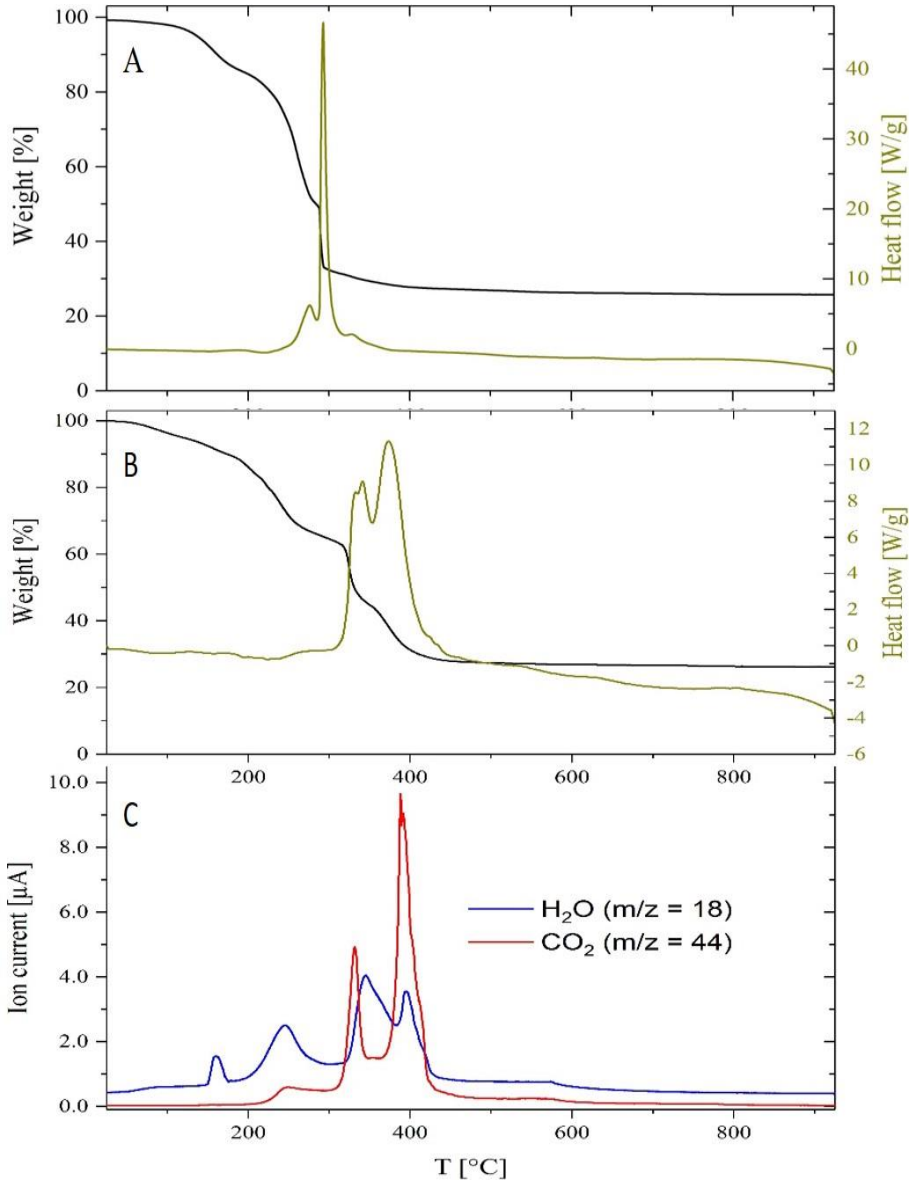

Figure 23: Thermogravimetric analyses and mass spectrometric (TGA-MS) of gel precursor sample LCO_3_3 (A) and LCO_3_2 (B, C) at heating rate of 10 K/min.

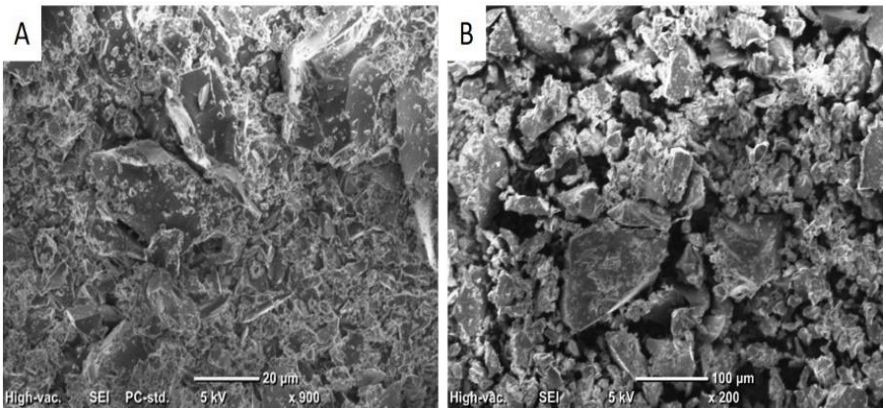

Figure 24: SEM picture for the precursor of $LiCoO_2$ synthesized with sol-gel water, A showing the 1. batch of synthesis and B the 2. batch of synthesis.

In particular the sample LCO-3-2 shows a narrow peak in the TGA signal, which can be explained with the low water content of the material, in comparison with the LCO-3-3, which shows a broader temperature range for the decomposition. In addition, it can be noticed qualitatively from the mass spectrum signals that the sample has much more water. This is reasonable if it is considered that the higher quantity of educts results in a bigger quantity of the gel, which needs to be dried. Due to this the temperature step at 400 °C was hold for longer time. However, from the TGA/MS measurement of the gel no conclusion on the result of the final calcination of the gel can be made, but it is used with the aim of identifying the correct range for the complete decomposition of the precursors and to estimate the holding time in the furnace.

The SEM pictures (Figure 24) of the gel show a negligible difference. It can be notice that for both samples the polymer framework looks not perfect homogeneous, which is maybe caused by higher water content or just a difference in the sample preparation for the SEM.

After the calcination, the LCO from the precursor of LCO-3-3 shows not a phase pure material, but a significant amount of CoO (JCPDS 9-0402) can be noticed. The intensity of the peak of CoO in the XRD measurement of this sample is in comparison with the 003 peak of hexagonal $LiCoO_2$ three times higher. (Figure 25) In addition, the XRD patterns show different phases of LCO and not only the hexagonal $LiCoO_2$, which is the aim for the synthesis of battery material.

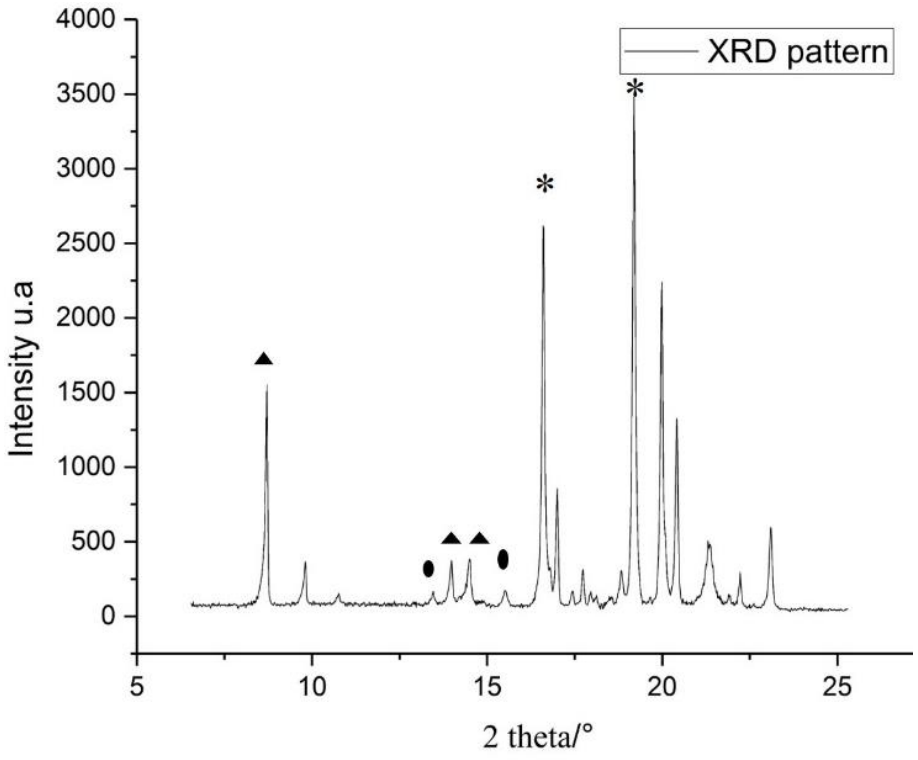

Figure 25.XRD pattern registered with Mo ($K\alpha_1$,λ=0.70931Å) for LCO (▲) as obtained from the sol-gel-water synthesis, after the scale-up. It can be noticed the presence of impurities as Co3O4 (●) and CoO (*)

Due to this the synthesis with small amounts of precursors was reproduced. A volume of 200 mL for the synthesis was figured out to be the suitable quantity for the synthesis, which results in an amount of LCO, which allows the structural and electrochemical characterization with one batch. The calcination time was adjusted in accordance to the results of a TGA/MS-measurement, which was performed for each sample. The performed TGA/MS-measurements resulted in the same wide range of gel decomposition between 330/350 °C and 430 °C, evolving mainly water and carbon dioxide with a total weight loss of 75-85 %. Additionally, other decomposition products were observed due to the chelate decomposition, but this signals were lower in intensity than the others. The quantitative analysis of the gel decomposition can be found in literature.[45]

Despite of different parameters in the preparation of the gel, the key role in the sol-gel synthesis is the calcination step. In the review by Antolini it is well described, how the final temperature of the calcination, but also the rate of heating influence the phase formation and the result of the synthesis.[36] The possibility of having different phases as function of the temperature makes it difficult to predict the success and the reproducibility of it each time. In theory, the high calcination temperature ensures the formation of hexagonal LCO with the space group R-3m. On the other hand the high temperature influences the amount of lithium available, as the

volatility of this is well known.[36] Due to this, either the temperature is too low for the formation of the pure hexagonal phase or the lithium is not enough to guarantee the stoichiometric phase of LCO. In fact, excess of lithium is used in the solid state synthesis of this material for resulting in the right stoichiometry.[36]

When the final product shows a stoichiometric and phase pure LCO, the XRD characterization should be studied in details. For this a Rietveld refinement was performed based on an overnight XRD measurement, if the 20 min XRD measurement showed phase pure LCO.

All the characteristic intensity and lattice parameters in comparison with the data from the ICDD (PDF 75-0532 XRD) database.

Subsequently Figure 26 shows the Rietveld profile for the sample LCO-3-4. The profile fits the XRD pattern with the crystallographic structure based on the α-$NaFeO_2$, prototype for this material as mentioned before, space group R -3m where Li and Co ions occupy the 3a and 3b octahedral sites of the trigonal unit cell. The hexagonal lattice parameters, *c/a* ratio and intensity ratio I_{003}/I_{104} of the 003 and 104 peaks are given in the Table 1

Table 1: Results of Rietveld Refinement of the LCO synthesized with sol-gel water.

#	**$LiCoO_2$ – sol-gel water_3_4**
A	2.81645(3) Å
C	14.05978(9) Å
c/a	4.99
I_{003}/I_{104}	1.27

The XRD patterns and the hexagonal *a* and *c* match well with the LCO reported in the literature *a* =2.81645(3) Å; *c* =14.05978(9) Å.(ref) The *c/a* ratio of 4.99 and well-resolved 006/102 and 018/110 peaks for all diffraction patterns are good indication for a perfect layered structure. The fact that the intensity ratio of I_{003}/I_{104} is bigger than 1.2 indicates the absence of cation mixing, confirmed better by the Rietveld refinement.[46,66]

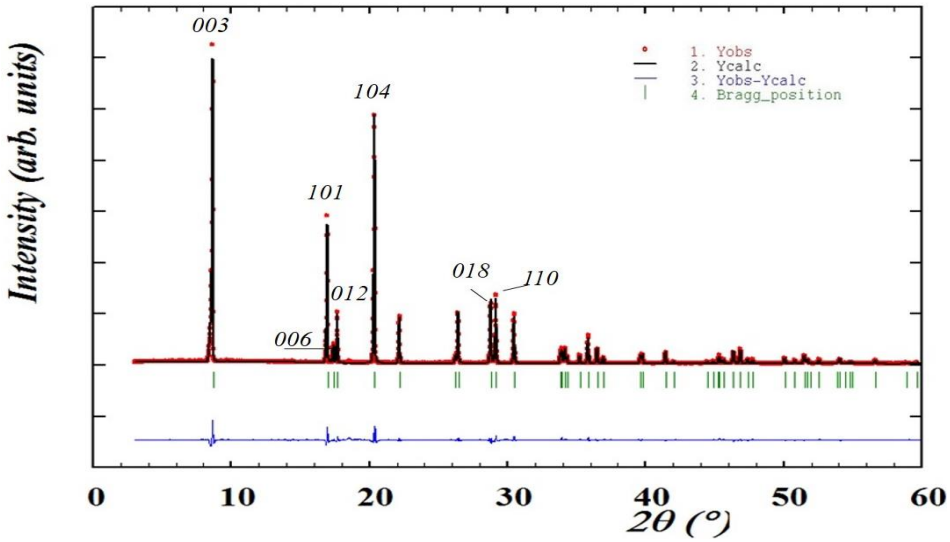

Figure 26: Rietveld Refinement of via sol-gel-water self-synthesized $LiCoO_2$ (R-3m) of the X-ray diffraction data. XRD pattern registered with Mo Kα1 (λ = 0.70932 Å).

For other samples the lattice parameters and other information are reported in Table 2. This shows the good reproducibility of the synthesis. The XRD patterns of the samples are shown with the Rietveld refinements in the Appendix 12.2.

Table 2: Results of Rietveld Refinement of the other LCO samples synthesized with sol-gel water (different batches) and the commercial LCO from MTI.

#	**$LiCoO_2$ -sol-gel-water-3-2**	**$LiCoO_2$ – sol-gel-water-3-9**	**$LiCoO_2$ – sol-gel-water-3-5**	**$LiCoO_2$ – sol-gel-water-3-11**	**$LiCoO_2$ – MTI**
c [Å]	14.0536(8)	14.0602(2)	14.0594(4)	14.0630(4)	2.8181(7)
a [Å]	2.81448(8)	2.81643(2)	2.81678(7)	2.81671(4)	14.0660(1)
c/a	4.99	4.99	4.99	4.99	4.99
I_{003}/I_{104}	1.27	1.27	1.27	1.27	1.25

The self-synthesized LCO was compared additionally with the commercial LCO, which was provided by MTI ($LiCoO_2$, MTI Corporation). The XRD patterns from the commercial LCO are in agreement with our desired phase, with the lattice parameters as shown in and Table 2. The most obvious difference is the particle size, which is 20 µm for the MTI sample in comparis on to 2-3 µm for the self-synthesized, as shown by SEM pictures in Figure 27.

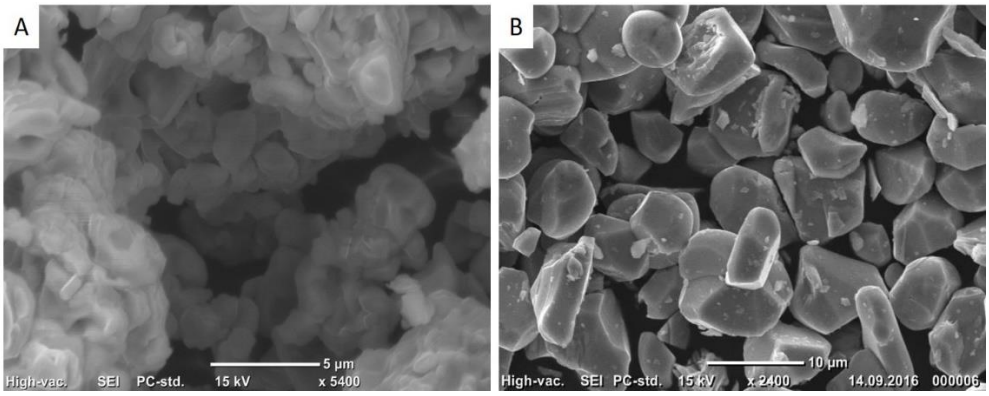

Figure 27: SEM pictures for $LiCoO_2$ (A, self-synthesizes via sol-gel-water) and (B, commercial LCO provided by MTI).

4.4 Electrochemical characterization

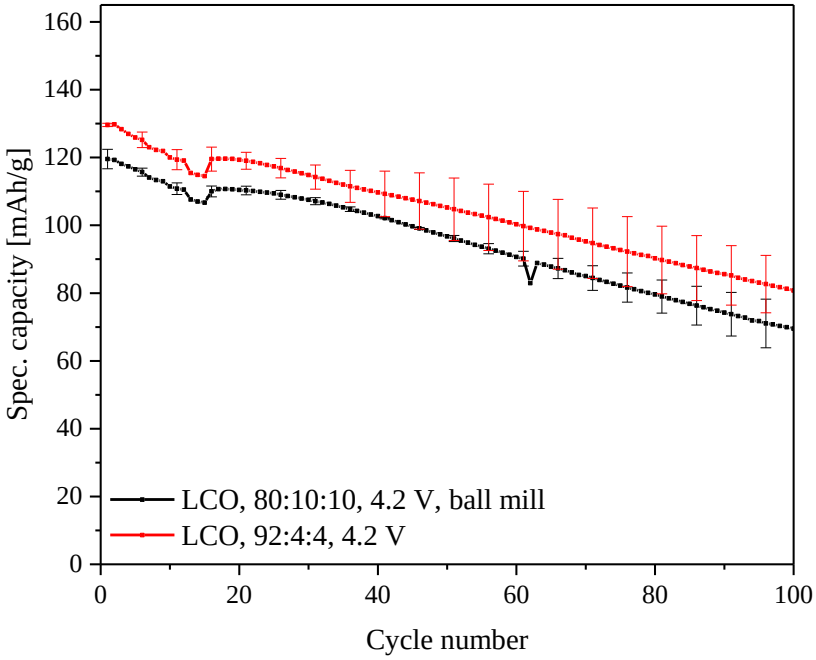

Figure 28: C rate test at C/10, C/5, C/2, 1C, 2C and cycle at C/2 for 100 cycles of $LiCoO_2$ with inks with 80 % or 92 % active material. For each composition, the average values of 3 cells with standard deviation are shown.

The Figure 28 shows specific discharge capacity of the rate capability and cycling test for the LCO for two different compositions of the LCO electrodes, which were measured in half cells with Li anodes. For better comparison of the different electrodes only the discharge capacity is plotted, which is relevant for the use of a battery. The theoretical capacity of LCO is 274 mAh/g, if the AM would be 100 % delithiated, but for calculating the C-rate a specific capacity of 150 mAh/g is used, which corresponds to an extraction of Li of x = 0.55 in $Li_{1-x}CoO_2$, which is the usable capacity for a stable cycling. The upper cut of potential is set to 4.2 V vs. Li/Li^+, which is for the LCO a high potential limit and already at the limit for the

irreversible change in the crystal structure of LCO, which anticipates the faster degradation of the cell during cycling.[67] Thus the capacity fade of the cells should be higher than for cells cycled with a lower cut of potential.

The red curve shows the average specific capacity and standard deviation of 3 cells of electrodes made with the Thinky mixer with 94 % AM, as described in chapter 3.5. The C-rate test (described in chapter 3.7) starts at C/10, the initial capacity of the LCO at this C-rate is 131 mAh/g. The specific capacity is decreasing with increasing C-rates, as expected.[68] After 100 cycles in total the measured specific capacity at a C-rate of 2 C was 80 mAh/g, which is 61 % of the initial value. The capacity loss for the self-synthesized LCO is higher than expected, as the LCO is known to be stable, but at lower cut off potential.[18]

The black curve shows the average specific capacity and standard deviation of 3 cells of electrodes made with the ball mill with 80 % AM, as described in chapter 3.5, which should result in an electrode in which all agglomerates are broken up and thus resulting in a homogeneous particle size distribution. The disadvantage of the ink preparation with the ball mill is the longer preparation time and the loss of material due to the fact, that the balls and the jar are covered with ink which cannot be used any more. Due to this the ball mill was not used any more for ink preparation. Additionally, the measured specific capacity for the 80 % AM electrodes is lower than for the electrodes with 92 % AM with a comparable capacity fade.

Subsequently, the Figure 29 shows the average and standard deviation of 3 cells each for specific discharge capacity for LCO provided by MTI in comparison to the self-synthesized LCO. For both materials electrodes with 92 % AM and 4 % SuperC65 and 4 % PVdF were used.

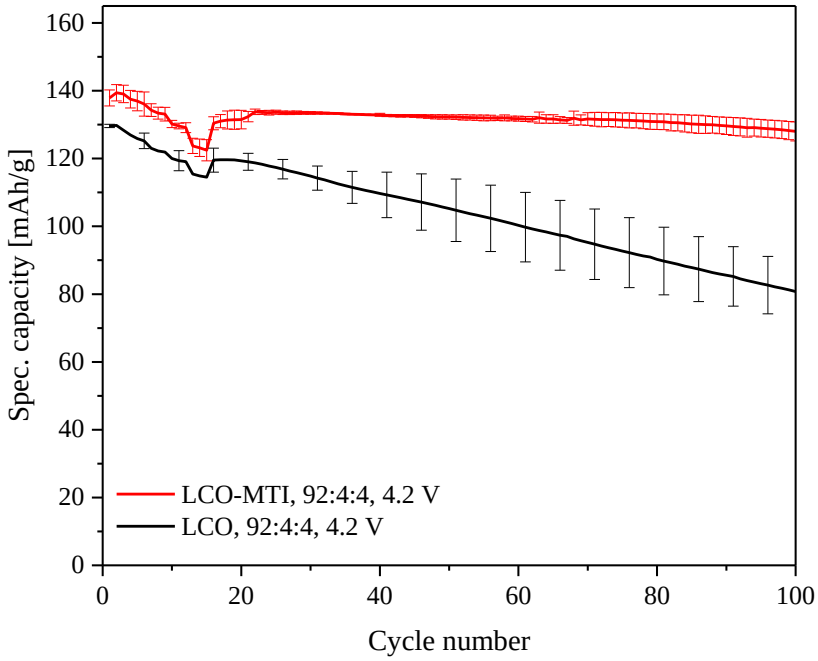

Figure 29: C rate test at C/10, C/5, C/2, 1C, 2C and cycle at C/2 for 100 cycles of LiCoO2 (black line self-synthesized LCO and red line commercial LCO) with inks with 92 % active material. For each composition, the average values of 3 cells with standard deviation up to 100 cycles are shown.

The cycling stability of the two material are obviously different and the commercial LCO shows good stability when it is cycled up to 4.2 V, but after 100 cycles also this is decreasing quite significant as shown in Figure 30. Moreover, the standard deviation is for the LCO from MTI much lower than for the results of the self-synthesized LCO.

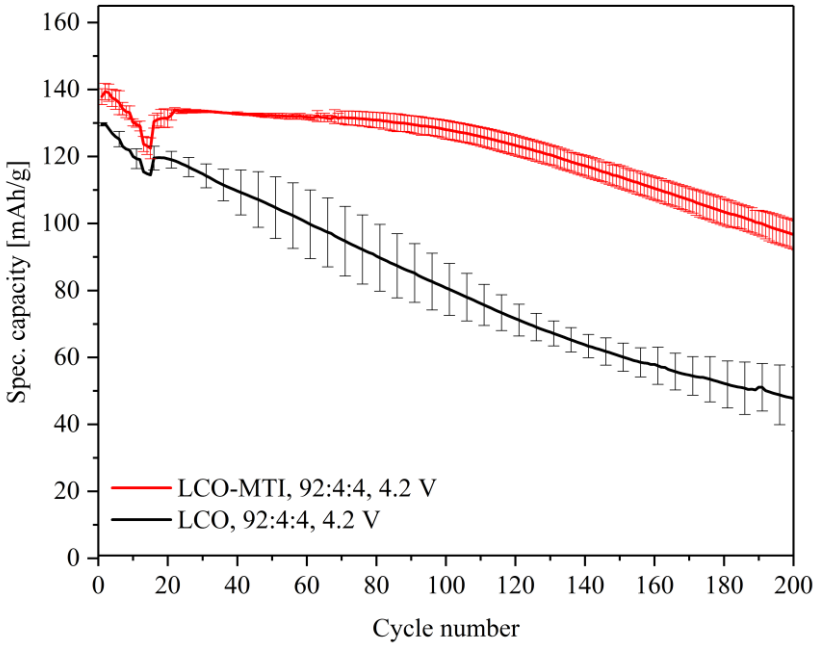

Figure 30: C rate test at C/10, C/5, C/2, 1C, 2C and cycle at C/2 for 100 cycles of LiCoO2 (black line self-synthesized LCO and red line commercial LCO) with inks with 92 % active material. For each composition, the average values of 3 cells with standard deviation up to 200 cycles are shown

Important to be investigated is a possible difference between the first and second cycle of the battery. This is investigated with the dQ/dV plot in Figure 31. This plot allows to identify, at which potential the processes of the active material happen and can tell more on the ongoing redox process. Additionally, it can give information about the reversibility or irreversibility during the operation of the battery. The dQ/dV plot for the LCO shows the first main anodic peak at a potential below 4.0 V and the corresponding cathodic peak as well. In the literature this peaks is assigned to the $Co^{3+/4+}$ redox couple.[69] However, from the analysis of the LCO self-synthesized is not a clear argument to say that exactly this redox process is happening.

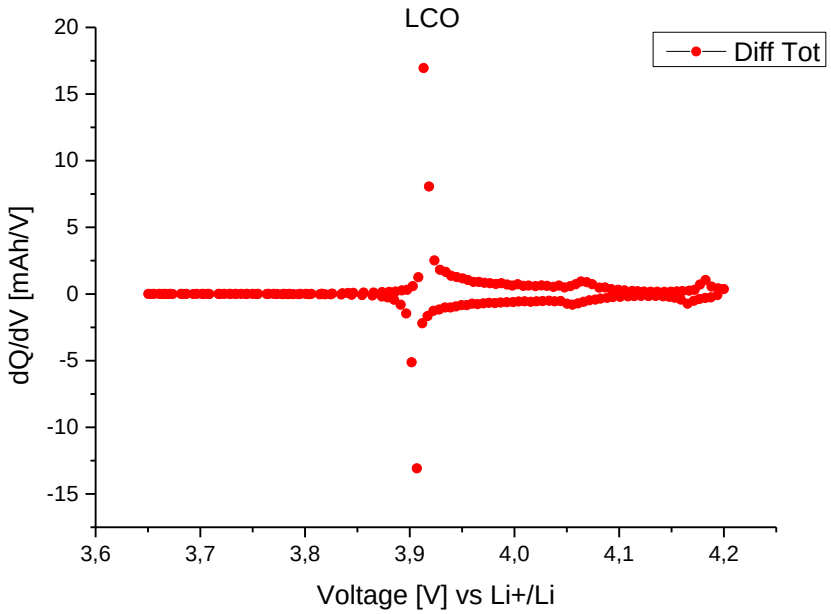

Figure 31: dQ/dV-plot for LiCoO2 vs Li^+/Li, assembled in a Swagelok cell, 1st charge and 1st discharge.

In fact, if only the transition metal is taken into account, for sure only Co is present, but it is necessary to think also about the influence and the role of the oxygen in the material. Since it is another element that might influence the electrochemistry, since it is known to be electrochemical active. Additionally, the anodic peaks at 4.06 V and 4.18 Vwith the corresponding cathodic peaks at 4.06 V and 4.16 V are assigned to the phase transition from the hexagonal to monoclinic and again to hexagonal.[46] To sum up, from the dQ/dV it can be seen the redox process correlate to the material, that in this case is reversible up to 4.2 V even if borderline.

The subsequent in-situ XRD, to understand what is going one during the first charge are analysed in the subsequent chapter.

4.5 In-situ measurements of LCO

4.5.1 In-situ XRD

The set-up of the pouch cell was done as mentioned in chapter 3.8.1 with LCO electrode loading of 3.00 ± 0.02 mg_{LCO}/cm^2. It allowed to record continuously XRD patterns (shown in Figure 32) during the first C/20 Charge up to 4.8 V. The XRD pattern were recorded in transmission mode as described in chapter 3.8.1.

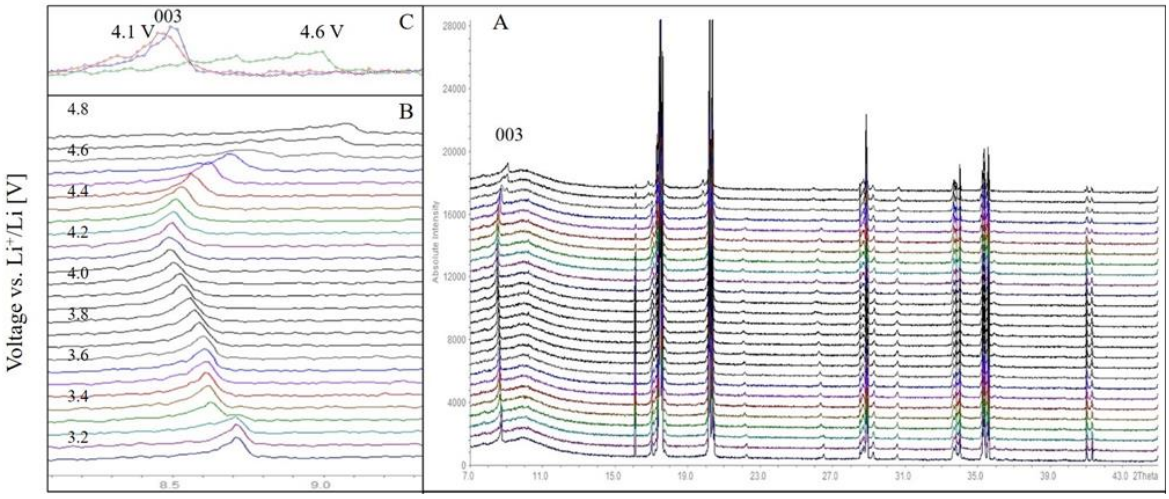

Figure 32: Raw-data of the in-situ XRD measurement assembled in the pouch cell LCO vs Li^+/Li, charged at C/20 up to 4.8 V. A: Complete set of the in-situ XRD data, with the attention on the 003 reflection. B: Zoom on the 003 reflection while charging. C: 003 reflection, the amorphous pattern after 4.6 V (green curve).

The variation of x in $Li_{1-x}CoO_2$ was calculated by the amount of charge to be 0.035 during the recording of one pattern with C/20 charge. Where x indicates the degree of delithiation. x = 1 means the cell was charged with the maximum theoretical capacity (274 mAh/g).

The potential curve of the in-situ XRD cell of the LCO vs. Li cycled with C/20 is shown in Figure 33. This is identical to the results of LNO charged in the Swagelok cell.

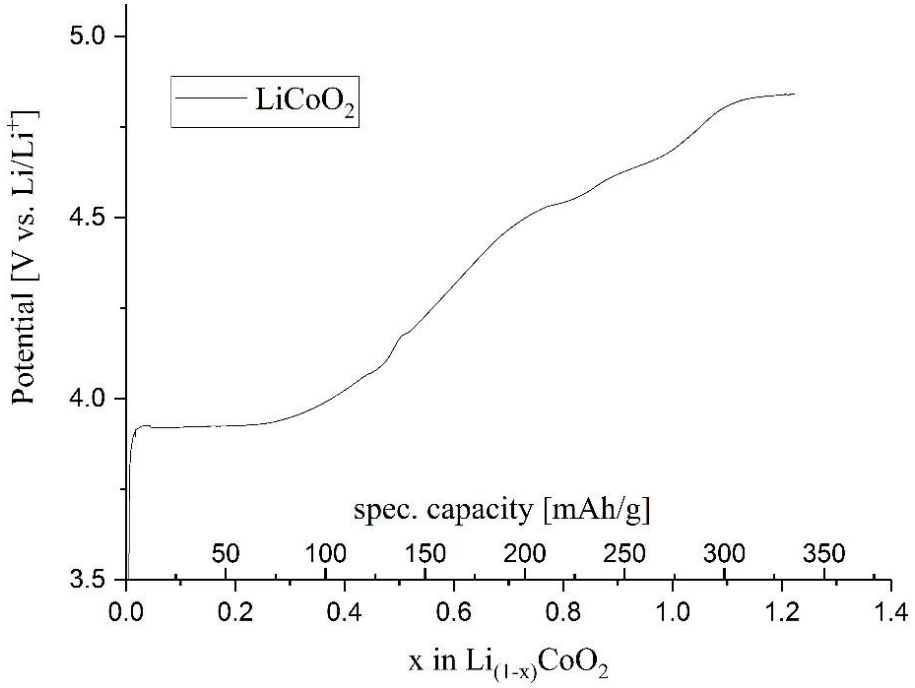

Figure 33 Charge curve for the pouch cell LCO vs Li^+/Li during the in-situ XRD data collection with C/20.

Before starting the electrochemical cycling of the cell, an XRD pattern was collected in the pristine state. The result is shown in Figure 34. By comparing the observed reflection positions of the LCO electrode to the standard capillary measurement of the pure LCO powder, a good agreement between both diffraction patterns can be recognized. All additional reflections in the upper pattern can be assigned to the aluminium current collector or the aluminium containing pouch foil.

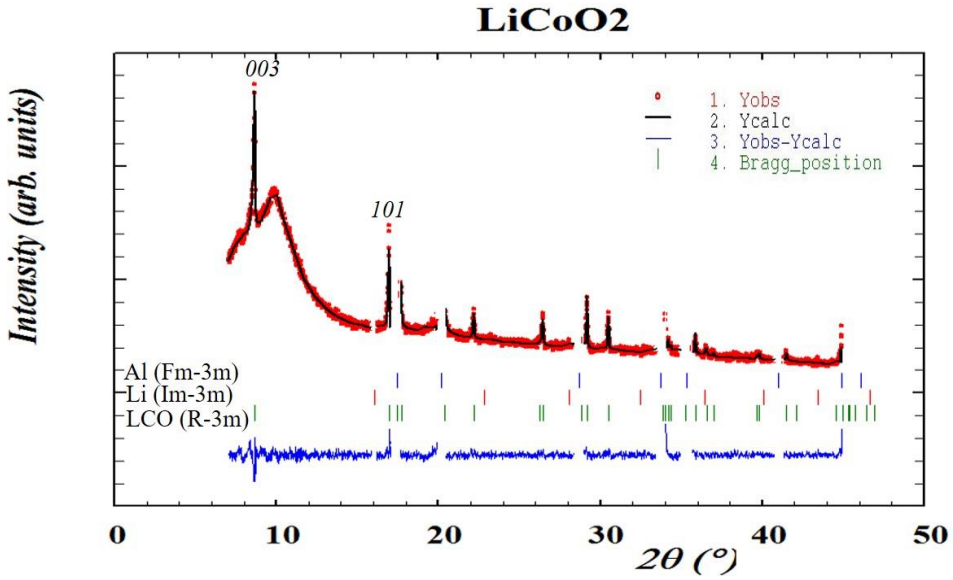

Figure 34: XRD pattern of the pristine LCO electrode assembled in the pouch cell vs Li^+/Li, cell before charging. Rietveld refinement for the three components. Due to high intensity Al was omit.

One obvious difference, however, is the highly reduced beam intensity of the LCO electrode diffraction pattern. The reason for this difference in intensity is the increase of the path length through the Aluminium foil, pouch cell foil, Li anode, separator and electrolyte which decreases the transmission of the X-rays. Furthermore the electrolyte in combination with the separator and the Pouch foil absorb X-rays and therefore the detected intensity decreases, too. Additionally, the thickness of the pouch cell and the layers of aluminium make it difficult to distinguish all pattern for the LCO with a good resolution. Nevertheless, the main reflections for the investigation of the LCO structure, e.g. 003 and 101, can be distinguished very well.

A first qualitative analysis of the XRD patterns of the pouch cell cycled at C/20 shows a shift of the 003 and 101 reflection, while all Al-reflection do not change its positions. Another important fact that indicates structural changes at high states of charge is the splitting of reflection 003 into 2 reflections, observed at potential slightly higher than 4.2 V on. Additional upcoming reflections can be observed also at 19.84 °.

All patterns were analysed using Rietveld refinement. For the cell charged up to 4.55 V the Rietveld refinements were calculated using the FullProf software package.[58] Al (F m-3m), LCO (R-3m), and Li (I m-3m) were refined according to their space group. The refined parameters are the scale factor, the specimen displacement or zero shift, the background, the lattice parameters, the profile parameters W and X and the asymmetry. Instrumental reflection broadening was refined with silicon standard and the reflection profile parameters were included in the refinement. The atomic coordinates, obtained from a crystallographic information file (ICSD 51182), were kept constant. For having a better resolution and due to the high intensity of the Al-reflections, this phase was refined first. After that the Al-reflections were taken out for the subsequent LCO refinement.

The refinement of pristine LCO is for example showm in Figure 34 shows the variation of *a* and *c* lattice-parameters and the *c/a* ratio during the electrochemical delithiation, charge curve is shown in Figure 33. The lithium content in the structure can be calculated as already discussed in section 4.5.1 third paragraph. during the delithiation of the LCO structure. The data reveal that the initial O3 structure of $Li_{1-x}CoO_2$ is maintained up to $Li_{0.54}CoO_2$ that corresponds to a capacity of 126 mAh/g and 4.21 V vs Li^+/Li. At this point, where x equals 0.46, the maximum *c* parameter (14.035(7) Å) is reached. In comparison in the pristine state the c lattice parameter was 14.411(7) Å. Nevertheless, at x=0.46 LCO still maintains the ordered hexagonal structure. The *c* parameter in fact is increasing on the z direction during the delithiation, however, the variation for *a*, which is changing from 2.8124(4) Å to 2.8066(7) Å, is much smaller ($\Delta a \sim 0.006$ Å, $\Delta c \sim 0.4$ Å). In fact, the c parameter is dominant considering the c/a ratio and therefore c/a shows the same trend. At 4.53 V vs Li^+/Li the 003 reflection is decreasing in intensity and a new reflection is observed that is attributed to a second, hexagonal LCO phase.

The hexagonal-monoclinic transformation is as reliable as the hexagonal-hexagonal one, however, the data were refined well with the hexagonal phase. The spinel phase was excluded because it shows a discrepancy in the reflections by the Rietveld analysis. In fact the values of lattice parameter after x=0.46 are obtained from the refinement of an hexagonal R-3m phase until x=0.22 at 4.53 V vs Li^+/Li. Thereby the c lattice decreases but maintained the R-3m phase. However, the structure started after 4.4 V to change irreversible and from 4.5 V it is getting amorphous. At x=0.18, it was not possible to discriminate the real reflections and to obtain the c lattice parameters. Since it is obvious in Figure 32, no crystalline structure can be refined

anymore because the intensity of the reflections is too low, the half width of the reflections is too broad and the signal to noise ratio is very bad.

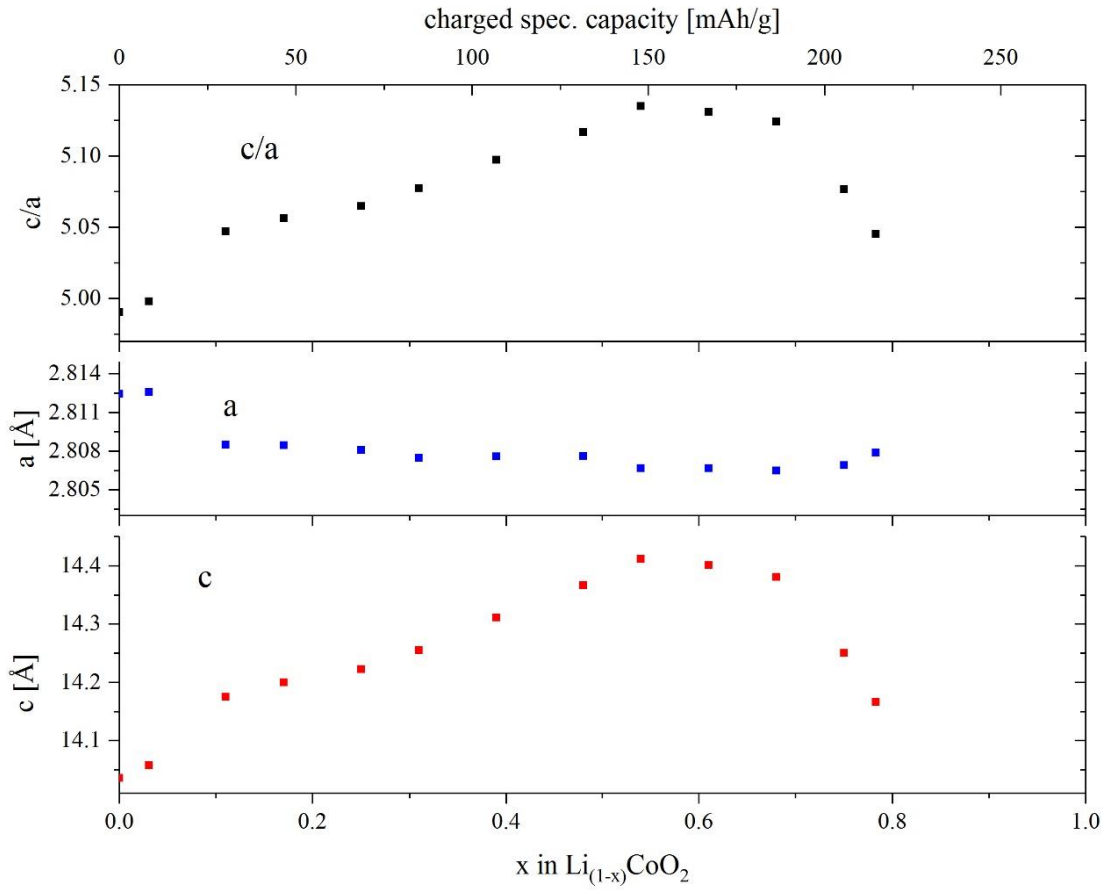

Figure 35 Variation of lattice parameters *a* , *c* and ratio *c/a*, subsequent of the Rietveld refinement of the $LiCoO_2$, in the hexagonal space group (R-3m) during delithiation.

Additionally, in-situ XRD pattern were recorded with C/10, Figure 36. The evolution of the reflections is similar to that observed for the C/20-cycling. Therefore it was renounced to an additional refinement.

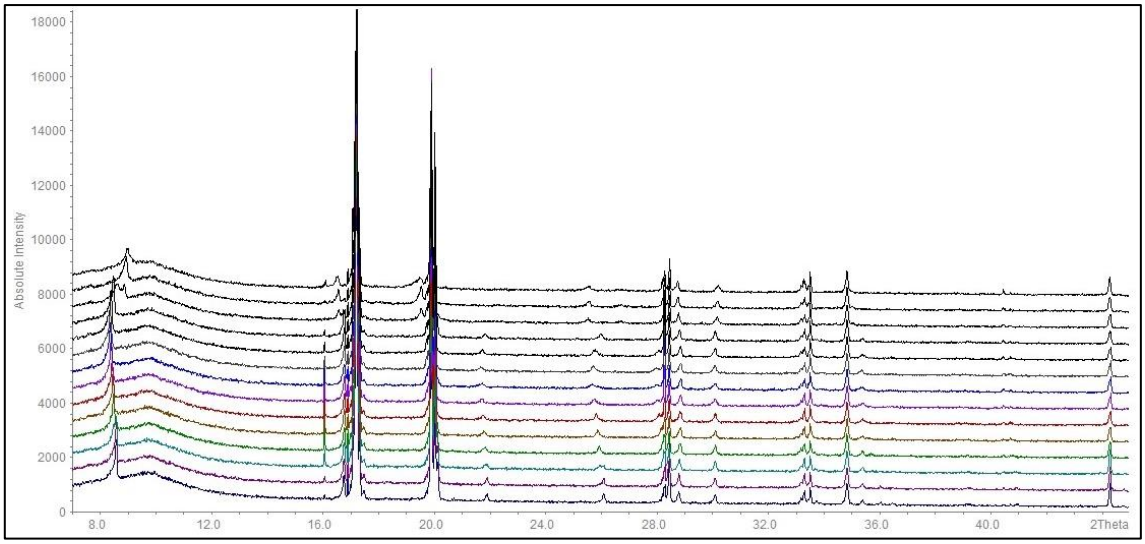

Figure 36. Raw pattern of the in-situ XRD measurement in the pouch cell of LCO vs Li^+/Li, charged at C/10.

4.5.2 In-situ OEMS

In order to analyze the gas evolution of an LCO-cell during the first charge, an OEMS-cell was built as described in chapter 3.8.2 and an OEMS experiment was performed. It was used an electrode with a loading of 5.96 mg/cm² (10.54 mg of AM in total). Two polymer separators soaked with 120 µL electrolyte (LP57) and a lithium counter electrode are used. Figure 37 shows the OEMS data obtained while charging LCO at C/10 up to 4.8 V. The upper part of the graph shows the voltage of LCO versus Li^+/Li of the cell, the middle the concentration of CO_2, CO and H_2 and the lower panel shows the corresponding gas evolution rates.

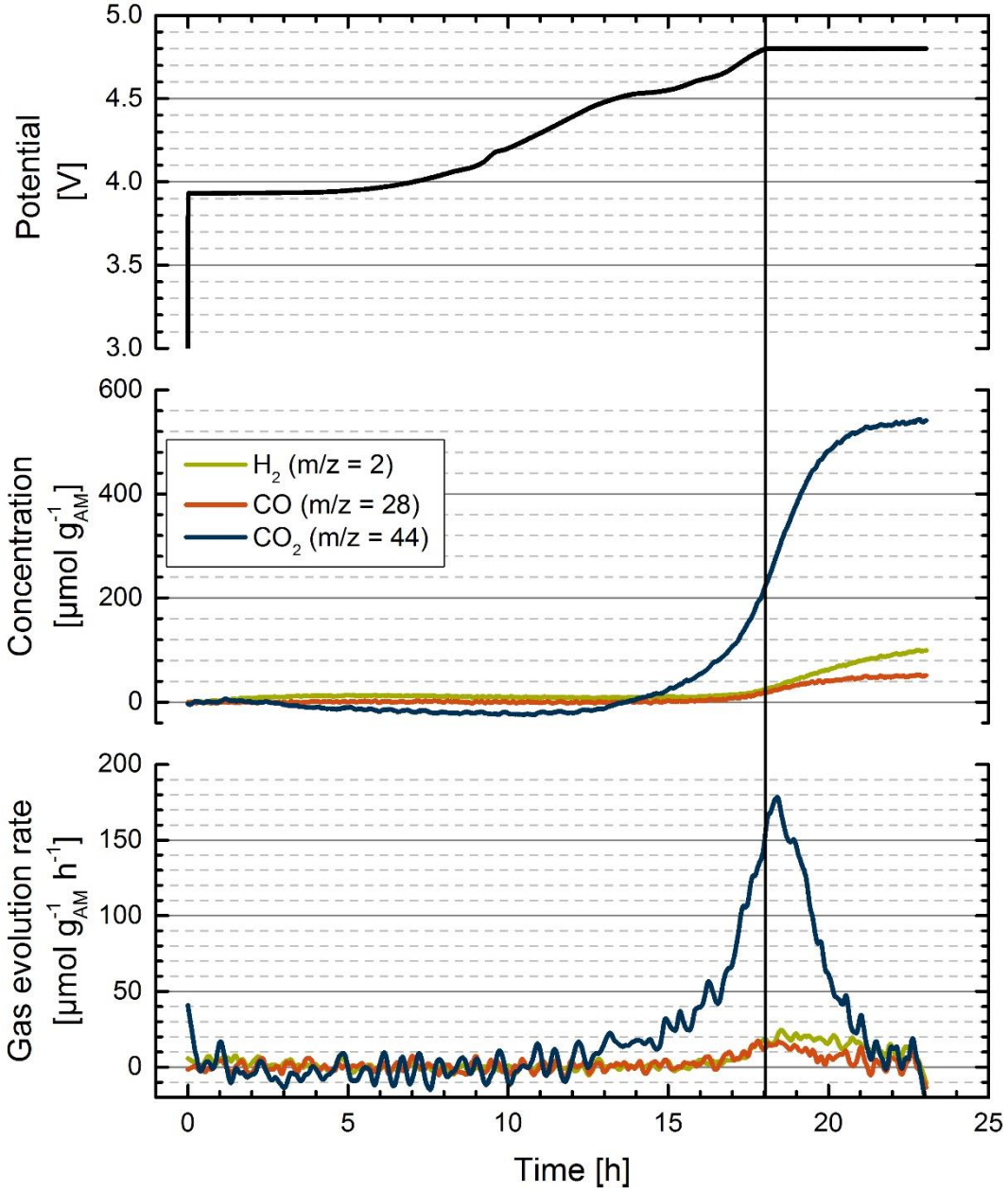

Figure 37: OEMS measurement of LCO vs Li^+/Li, charged at C/10 up to 4.8 V. Upper panel shows the voltage curve of the cell, in the middle the gases evolved with the gas evolution rate in the below one.

The CO_2 evolution starts at 4.4 V vs Li^+/Li followed by a continuous increase up to 4.8 V vs Li^+/Li and continuing with a lower evolution rate during the CV step. The CO and H_2 evolution start slightly before 4.8 V. The onset of the H_2 and CO evolution can be correlated with the decomposition of the organic electrolyte as shown by Zhang et al.[70] and with the structural changes in the powder diffraction patterns at this voltage (chapter 4.5.1).

5 Synthesis of $LiNiO_2$ and characterization

5.1 Sol-gel-water synthesis and characterization

In the literature is well described that it is almost impossible to synthesize the stoichiometric $LiNiO_2$ (LNO), but results close to this can be reached. In fact another convention to write this material is $Li_{1-z}Ni_{1+z}O_2$, due to the cation mixing, since Li^+ is similar in dimension with Ni^{3+}.[31]

Since for the stoichiometric LCO the water sol-gel was identified as a good route for having a phase pure material with an acceptable control of the morphology, the same method was used with adapting some parameters for LNO. For comparison reasons as few as possible parameters were modified and the same precursors were used; acetates as metal sources and citric acid as complexing agent. A lithium-nickel-citrate gel precursor was obtained following the same procedure as for LCO reported by Pedroana et al.[64]: Li(CH3COO) (Sigma Aldrich, 99.99%) and Ni(CH3COO)2*4H2O (Sigma Aldrich, >99.0%) were used in a molar ratio of 1.2 : 1 as metal oxide sources, citric acid was used in a molar ratio of 1 in relation to the Ni as chelating agent. The formation of the gel was performed by following the same steps Figure 38 as described in the LCO paragraph 4.3 with the only variation in the pH, which was set to 6.5-7.0 with ammonium hydroxides.[71]

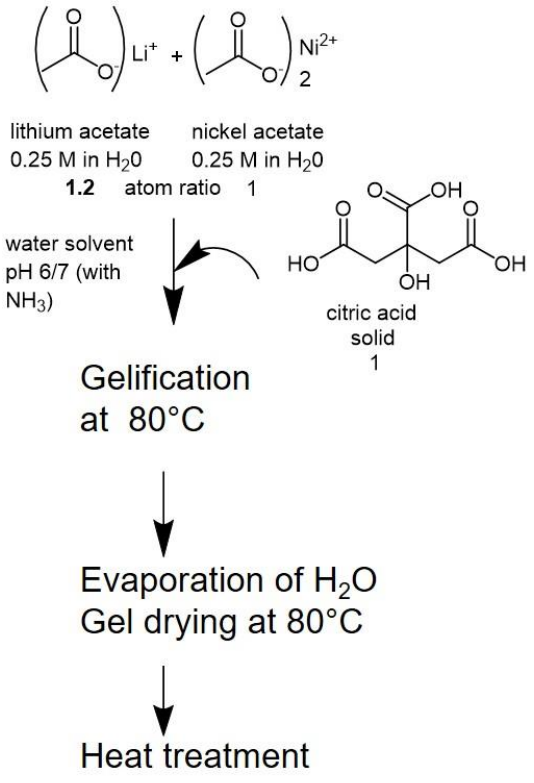

Figure 38: Schematic representation for the LiNiO2 synthesis via sol-gel using water as solvent.

The thermal treatment was changed due to the instability of Ni^{3+} in $LiNiO_2$ in air atmosphere to an oxygen one for the calcination step. In fact, it is reported the stabilization of the Ni^{3+} in oxygen atmosphere.[32]

Based on the literature and on the TGA/MS measurement (Figure 39) the heat treatment was performed in 2 steps, as shown in Figure 40.[71] The DSC signal of the TGA/MS measurement shows two different important peaks correlated to a significant weight lost, the first in the range of 310-390 °C and the second between 490-530 °C. Additionally, the mass spectrum confirms the decomposition of the complex agent with the evolution of CO_2, CO and obviously, H_2O due to the solvent.

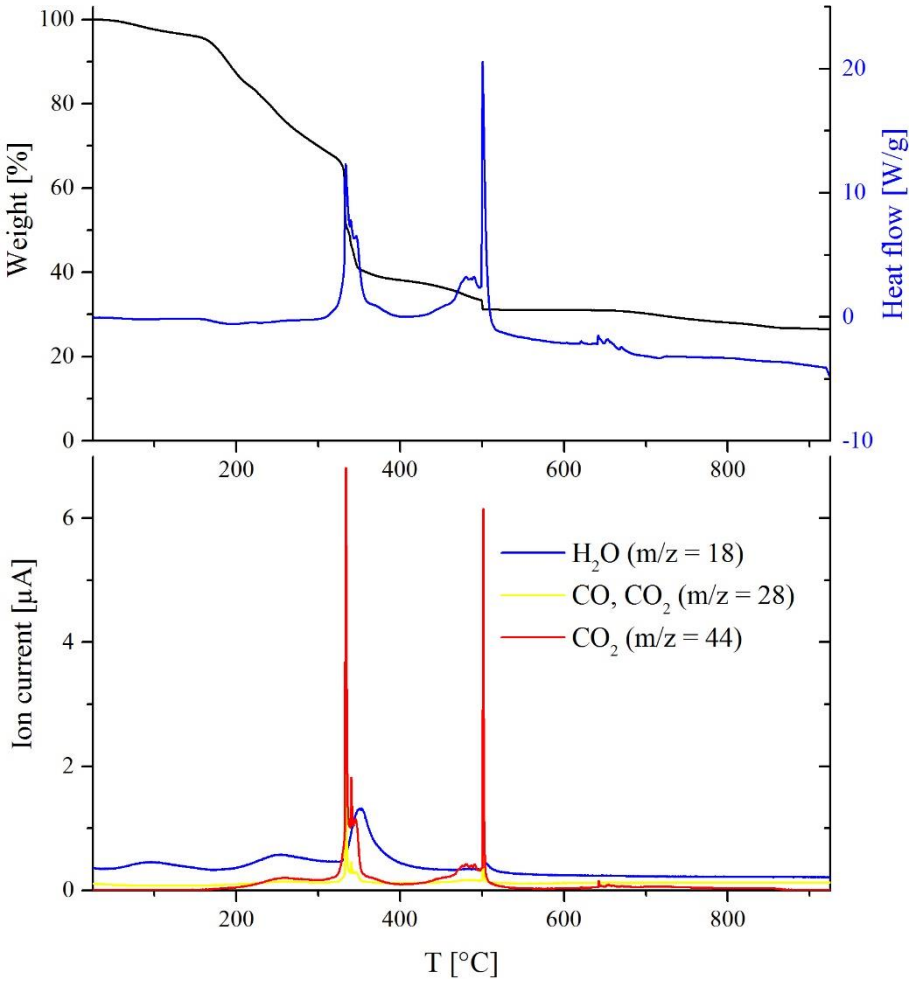

Figure 39: Thermogravimetric analyses and mass spectrometers (TGA-MS) of gel precursor for LiNiO2 at heating rate of 10 °K/min.

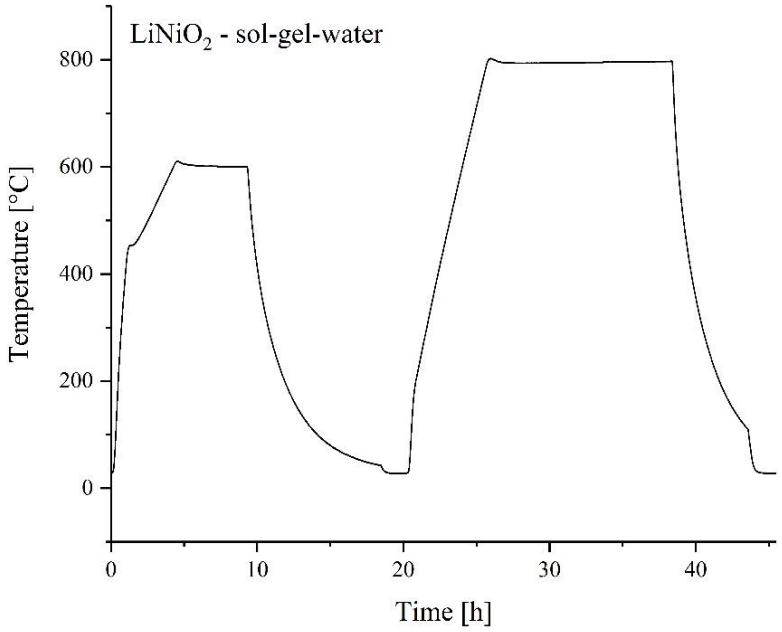

Figure 40: Preannealing treatment for LiNiO2 precursor with 1 K/min up to 400 °C and 5 K/min up to 600 °C in synthetic air atmosphere and annealing treatment with 5 K/min up to 800 °C in oxygen atmosphere.

The pre-calcination step of the precursors of the LNO was done in air atmosphere at 600 °C for 6 h, the procedure is shown in the Figure 40. Subsequently, the particles were ground in an agate mortar and calcined at 800 °C for 13 h in an oxygen atmosphere. After this annealing LNO powder was obtained.

The XRD pattern of the obtained LNO-powder (Figure 41) shows a good crystallinity.

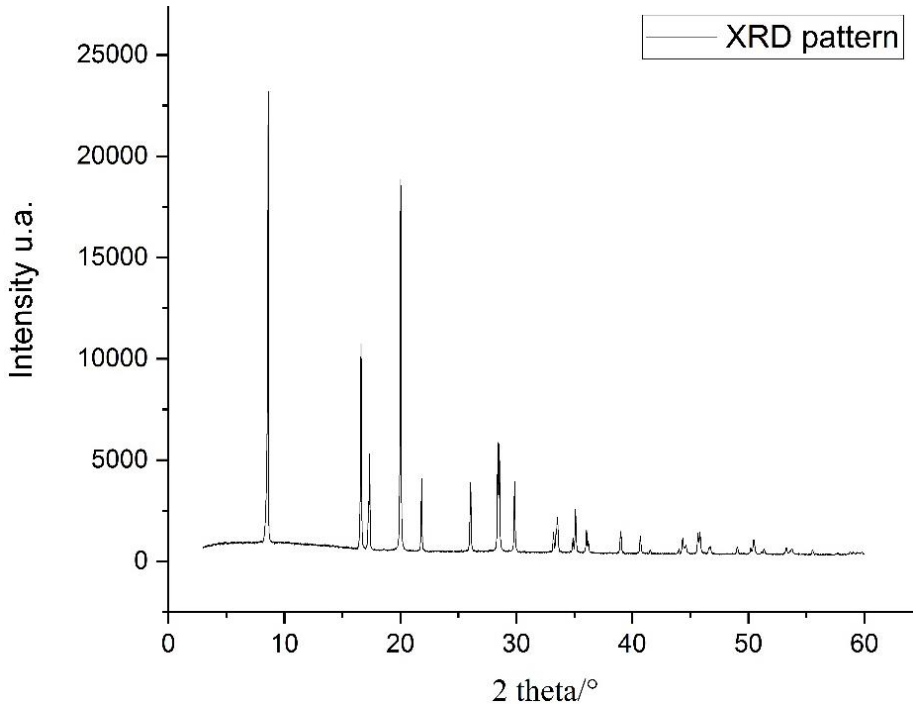

Figure 41: X-ray diffraction (XRD) pattern registered with Mo ($K\alpha_1$,λ=0.70931Å) of LNO powders as-obtained by the sol-gel water method, no impurity is noticed.

The stoichiometry of the sample was identified by phase-matching with ICCS data base to be $Li_{1-z}Ni_{1+z}O_2$ with $0.00 \leq z \leq 0.02$. As mentioned before, the ideal stoichiometry $LiNiO_2$ is difficult to reach, and as a pure crystalline phase can be observed, the sample was used for further investigation.

The SEM pictures (Figure 42) shows the gel before pre-calcination (A), after pre-calcination (B) and after the final annealing (C, D). Primary particles of the LNO powder (Figure 42 C, D) can be identified with hexagonal shape from the SEM. Additionally the range of the particle size can be determined despite the agglomerates of primary particles. By counting a significant number of particles in the SEM picture, the particle size can be estimated to be between 1 and 2 µm. To ensure that this result is reliable, the specific surface area of the LNO sample was measured with BET resulting in 1.5 m^2/g. This resulted with the assumption of spherical particles, as described in chapter 3.3, in an average particle size of 0.9 µm consistent with the SEM evaluation.

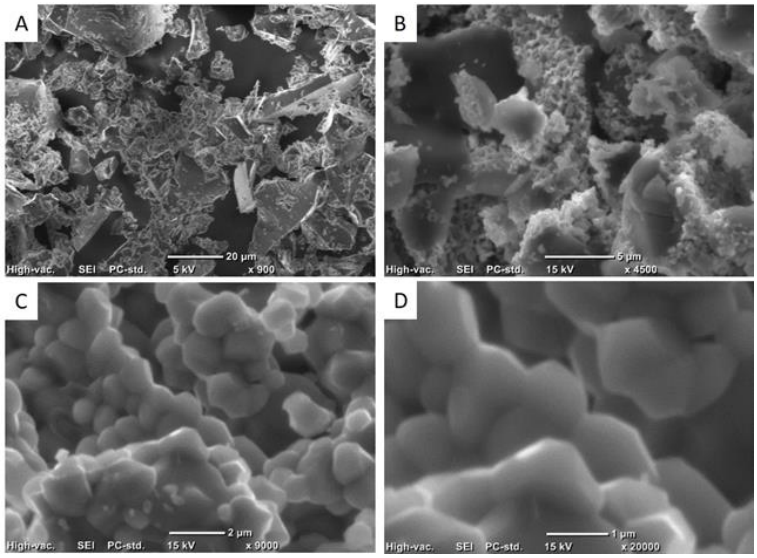

Figure 42 : SEM-pictures of the gel for LNO before pre-calcination (A), after pre-calcination (B) and after the final annealing (C, D).

Subsequently Figure 43 shows the Rietveld profile for the LNO. The profile fits the XRD pattern with the crystallographic structure based on the α-$NaFeO_2$, with a space group R -3m (fig a). In an ideal stoichiometric LNO the Li^+ and Ni^{3+} cations are supposed to occupy the 3a and 3b octahedral sites of the trigonal unit cell and oxygen the 6c position. However, taking in consideration the cation mixing, the disorder was refined leading in a better profile matching (FIG b) In fact the Ni^{3+} and Li^+ result to have a site-exchange. The cation mixing, based on the occupancy was calculate to be around 3 %.

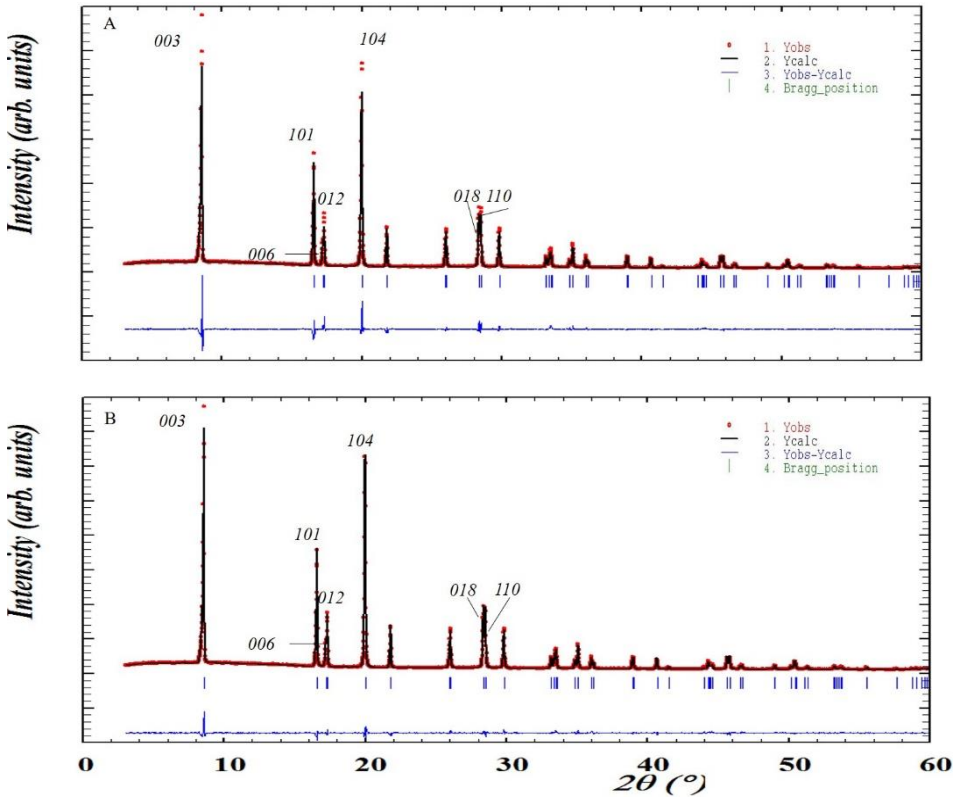

Figure 43 Rietveld Refinement of the via sol-gel-water self-synthesized $LiNiO_2$ (R-3m) of the X-ray diffraction data. XRD pattern registered with Mo Kα1 (λ = 0.70932 Å). A: without cation mixing and B Improvement due to the consideration of the cation mixing.

The hexagonal lattice parameters, *c/a* ratio and intensity ratio I_{003}/I_{104} of the 003 and 104 peaks are given in the Table 3.

Table 3: Results of Rietveld Refinement of the LNO synthesized with sol-gel water.

#	**$LiNiO_2$ – sol-gel water**
c	14.2061(2) Å
a	2.8798(8) Å
c/a	4.932883
I_{003}/I_{104}	1.43

The XRD patterns and the hexagonal *a* and *c* match well with the LNO reported in the literature *a* =2.8798(8) Å; *c* =14.2061(2) Å. Since the 006/012 and 018/110 peaks are correlate to a perfect layered structure, in this pattern are not perfect resolved. Moreover, the *c/a* ratio is

4.932883, deviated from the 4.99 assigned usually to a well-ordered structure and the fact that the intensity ratio of I_{003}/I_{104} is 1.43, bigger than 1.2-1.3 confirms the presence of the cation mixing in the LNO.[32]

The other samples show a good reproducibility of the synthesis of. $Li_{1-z}Ni_{1+z}O_2$ with $0.00 \leq z \leq 0.02$.

The self-synthesized LNO was compared additionally with the commercial LNO, which was provided by Sigma-Aldrich ($LiNiO_2$, Sigma-Aldrich). However, the patterns from the commercial LNO are not in agreement with the near stoichiometric pure LNO, but shows different phase of LNO or impurity Figure 44. It can be noticed also some additional peaks corresponding to a significant amount of Li_2CO_3 as matching with the ICCS data code (9008283)

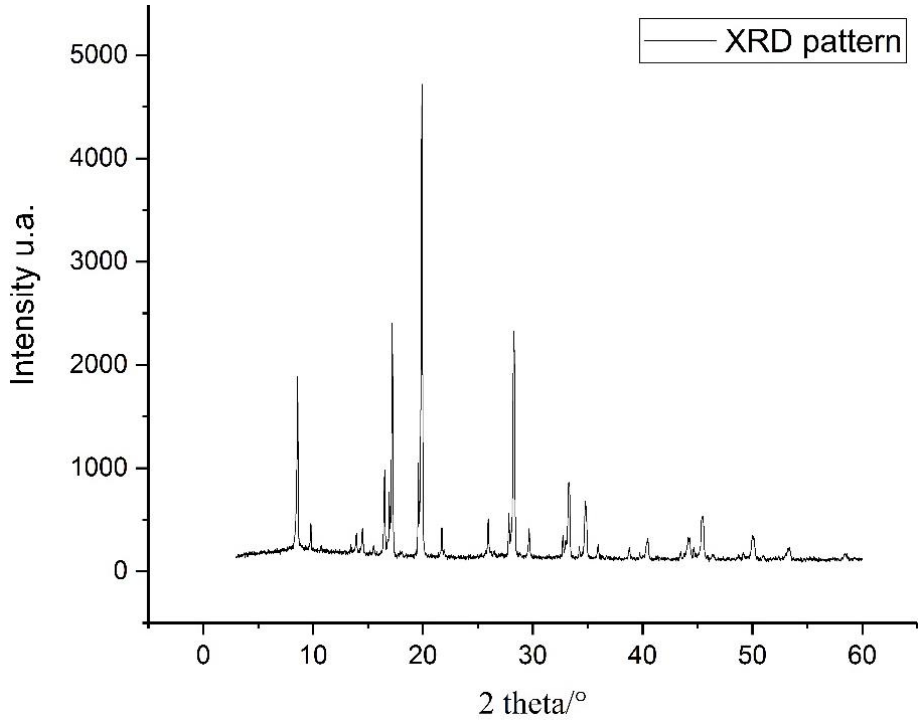

Figure 44. XRD pattern registered with Mo ($K\alpha_1$,λ=0.70931Å) of the LNO provided by Sigma Aldrich. A mixture of non-stoichiometric LNO and Li_2CO_3 was identified.

5.2 Electrochemical characterization

The Figure 45 shows specific discharge capacity of the rate capability and cycling test for the LNO for two different compositions of the LNO electrodes, which were measured in half cells with Li anodes. For better comparison of the different electrodes only the discharge capacity is plotted, which is relevant for the use of a battery. The theoretical capacity of LNO is

274 mAh/g, if the AM would be 100 % delithiated, but for calculating the C-rate a specific capacity of 160 mAh/g is used, which corresponds to an extraction of Li of x = 0.58 in $Li_{1-x}NiO_2$. The upper cut of potential is set to 4.2 V vs. Li/Li^+, which is the same as for LCO, even if for LNO is reported that has a reversible capacity also at high potential.

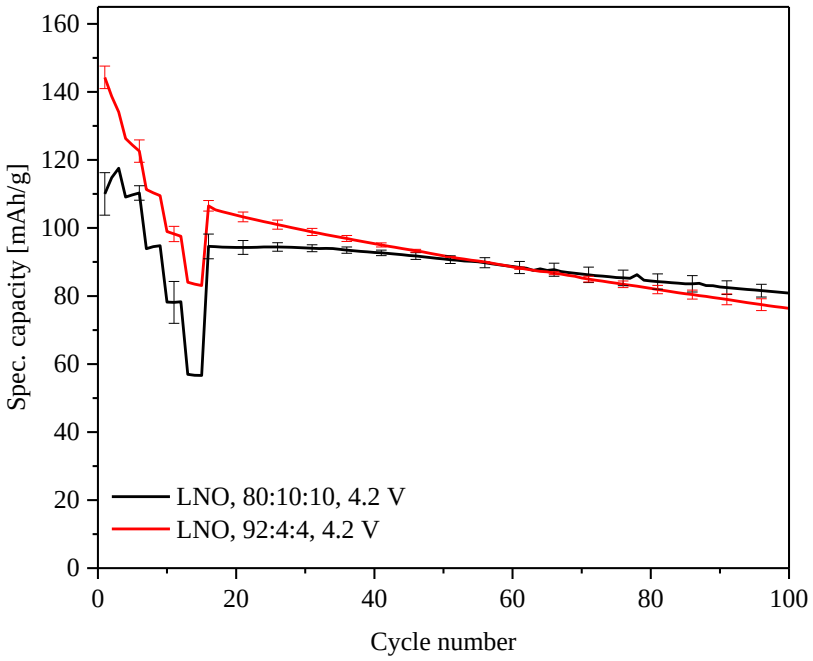

Figure 45: C rate test at C/10, C/5, C/2, 1C, 2C and cycle at C/2 for 100 cycles of LiNiO2 with inks with 80 % or 92 % active material. For each composition, the average values of 3 cells with standard deviation are shown.

The red curve shows the average specific capacity and standard deviation of 3 cells of electrodes made with the Thinky mixer with 94 % AM, as described in chapter 3.5. The C-rate test (described in chapter 3.7) starts at C/10, the initial capacity of the LCO at this C-rate is 144 mAh/g. The specific capacity is decreasing with increasing C-rates, as already seen for LCO. After 100 cycles in total the measured specific capacity at a C-rate of C/2 was 77 mAh/g, which is 55 % of the initial value. The capacity loss for the self-synthesized LNO is better than expected and same for the cycling stability.

The black curve shows the average specific capacity and standard deviation of 3 cells of electrodes made with 80 % AM, as described in chapter 3.5, which should result in a better coating due to the better homogeneity, therefore better performance.

Subsequently, the Figure 46 shows the average and standard deviation of 3 cells each for specific discharge capacity for LNO provided by Sigma Aldrich, in comparison to the self-synthesized LNO. For both materials electrodes with 92 % AM and 4 % SuperC65 and 4 %

PVdF were used. The commercial LNO from Sigma, however, shows zero activity and was not possible to compare in terms of electrochemical characterization.

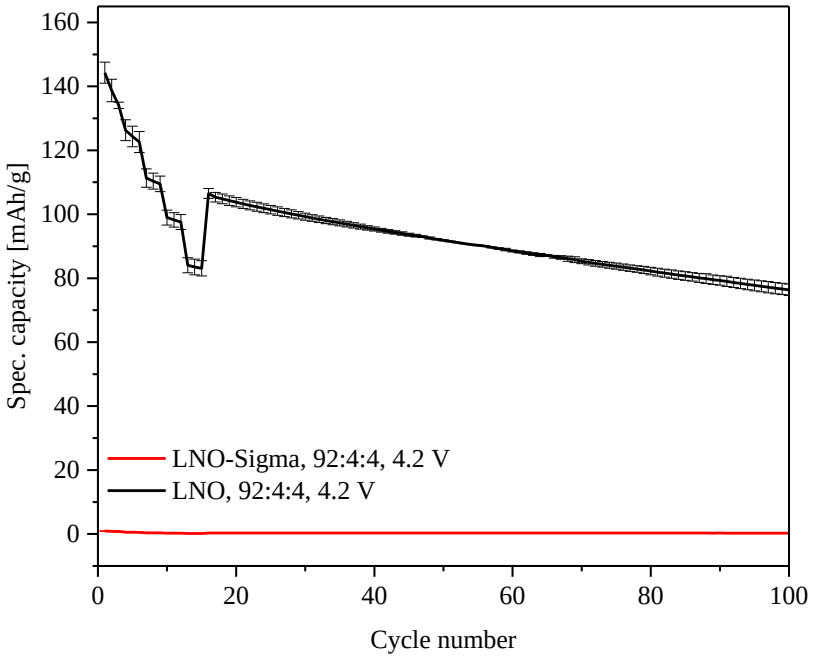

Figure 46: C rate test at C/10, C/5, C/2, 1C, 2C and cycle at C/2 for 100 cycles of LNO from Sigma-Aldrich (red line) and the self-synthesized LNO (black line) with inks with 92 % active material. For each sample the average values of 3 cells with standard deviation are shown.

Even more important than for the LCO, is to investigated the difference between the 1st charge and 1st discharge of the battery, subsequent of the identification of the disorder. This is investigated with the dQ/dV plot as for LCO. The Figure 31 shows the plot for LNO, an interesting point is the big difference between the capacity, during the first charge start that start at 191 mAh/g with an subsequent decreasing for the first discharge up to 141 mAh/g.

Additionally, the dQ/dV is used as indication about the reversibility or irreversibility during the operation of the battery, in particular here the 1st cycle. The first main anodic peak is at a potential below 3.8 V and the corresponding cathodic peak at 3.6 V.

It can be noticed, however, that the main redox peak are not reversible at 3.8 V due to the difference in the intensity of the dQ/dV, might be an indication of the reorganization of the structure. On the other hand, the second, anodic and cathodic peak at higher potential seems to be reversible.

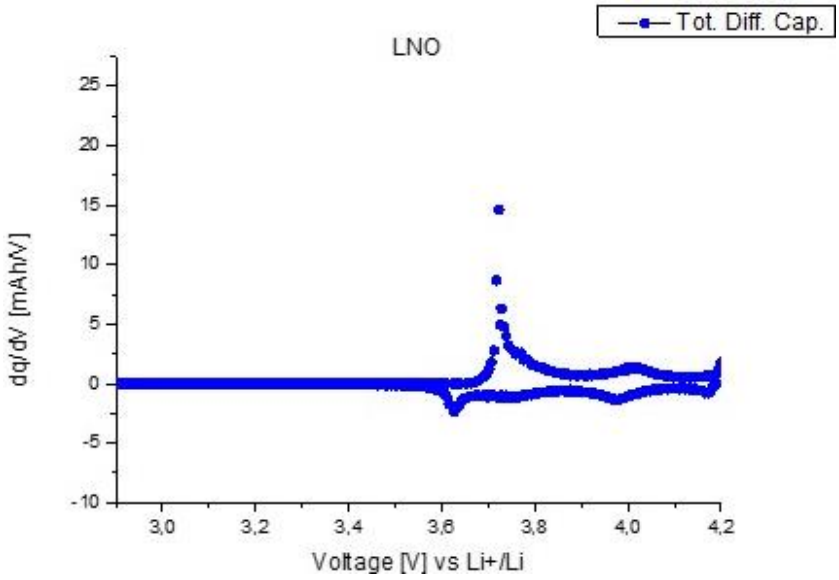

Figure 47: dQ/dV-plot for LNO vs Li^+/Li, assembled in a Swagelok cell, 1st charge and 1st discharge.

In fact, if only the transition metal is taken into account, only nickel is present, however is necessary to think about the influence and the role also of the oxygen during the electrochemical process. It is another element that might influence the electrochemistry and it is known to be electrochemical active.[21,72] Additionally, the mixing of the Li with Ni in the structure can lead to more effects that have to be investigate during the charge.

From the dQ/dV, therefore, it can be seen the redox process correlate to the LNO material, with the irreversible first redox process at 3.8 V and reversible at 4.0 V, but cannot be assigned the real oxidation state of the redox couple.

The subsequent in-situ XRD patterns, to understand what is going one during the first charge will be analysed in the subsequent chapter.

5.3 In situ measurements of LNO

5.3.1 In-situ XRD

The set-up of the pouch cell was developed as mentioned in the chapter 3.8.1. and was used with a LNO electrode with the loading of (3.82 ± 0.02 mg_{LNO}/cm^2).

This set-up allows to record continuously XRD patterns (shown in Figure 48) during charging with C/20 up to 5.2 V.

The XRD pattern were recorded in transmission mode as described in chapter 3.8.1. The variation of x in $Li_{1-x}NiO_2$ as for the LCO was estimate to be 0.035 during the recording of one

pattern with C/20 charge. Where x indicates the degree of delithiation. x = 1 means the cell was charged with the maximum theoretical capacity (274 mAh/g).

Before starting the electrochemical cycling of the cell, an XRD pattern was collected in the pristine state. The result is shown in Figure 48. By comparing the observed reflection positions of the LNO electrode to the standard capillary measurement of the pure LNO powder, a good agreement between both diffraction patterns can be identified. Since the pouch cell was build in the same way, the Al phase is correlated to it.

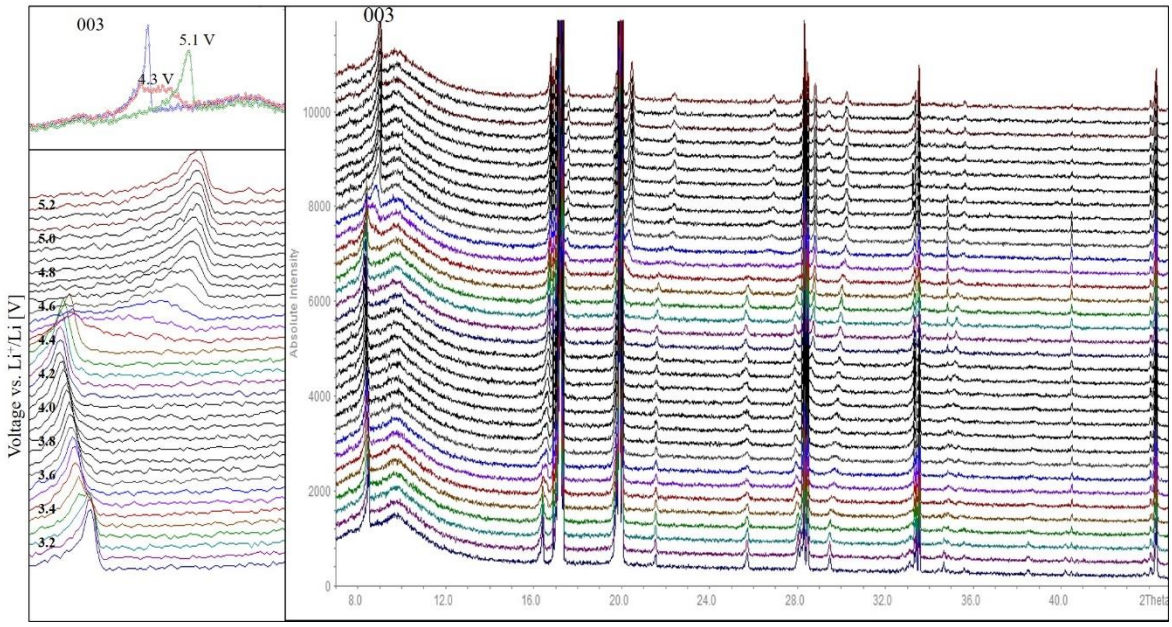

Figure 48: Raw-data of the in-situ XRD measurement assembled in the pouch cell LNO vs Li^+/Li, charged at C/20 up to 5.2 V. A: Complete set of the in-situ XRD data, with the attention on the 003 reflection. B: Zoom on the 003 reflection while charging. C: 003 reflection, pristine (blue curve), phase transformation (red curve) and stable phase of NiO_2 (green curve).

One obvious difference, as discussed for the LCO is the highly-reduced beam intensity of the LNO electrode diffraction pattern. The electrolyte in combination with the separator and the Pouch foil absorb X-Rays and therefore the detected intensity decreases. Nevertheless, the main reflections for the investigation of the LNO structure, e.g. 003 and 101, can be distinguished very well.

A first qualitative analysis of the XRD patterns of the pouch cell cycled at C/20 shows a shift of the 003 and 101 reflection, which stay stable up to a high voltage 5.2 V. This indicate that after the complete delithiation the structure is still crystalline and can be well-identified.

The potential curve of the in-situ XRD cell of the LNO vs. Li charged with a C-rate of C/20 is shown in Figure 49. This is identical to the results of LNO charged in the Swagelok cell.

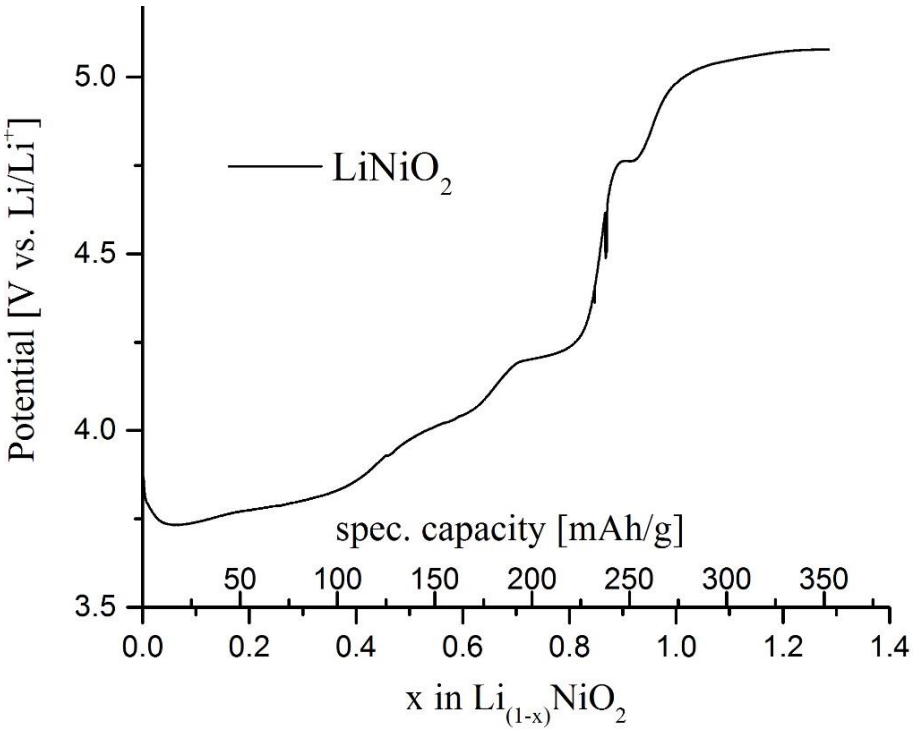

Figure 49: Charge curve for the pouch cell with LNO vs Li^+/Li during the in-situ XRD collection.

All patterns were analysed using Rietveld refinement. For the cell charged up to 4.55 V the Rietveld refinements were calculated using the FullProf software package[58,66]. Al (F m-3m), LNO (R -3m), and Li (I m-3m) were refined according to their space group as discussed in section 4.5.1 for the LCO. The refinement of pristine LNO is shown in Figure 50.

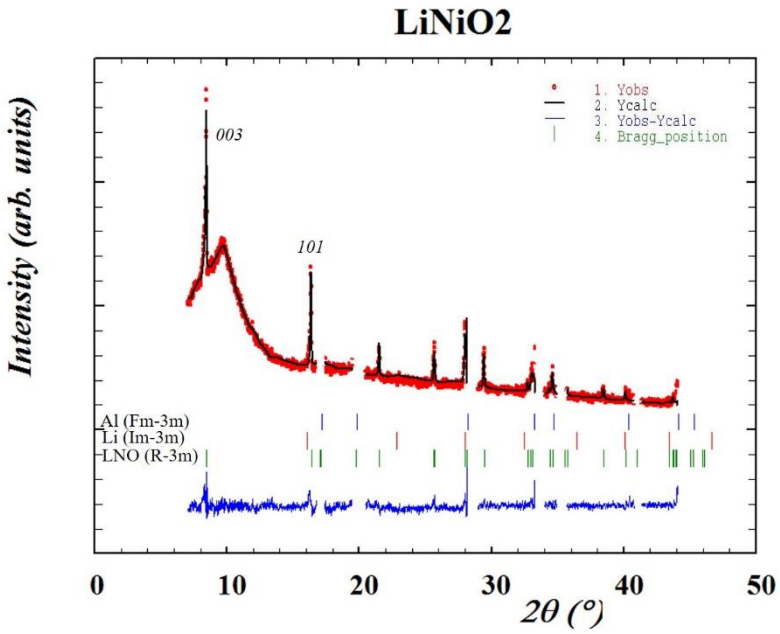

Figure 50: XRD pattern of the pristine LNO electrode assembled in the pouch cell vs Li^+/Li, cell before charging. Rietveld refinement for the three components. Due to high intensity Al was omit.

The accordance in positions are well described. However, the mismatching in the intensity of the LNO peaks is important to be taken into account. As it was discussing in the chapter is due to the mixing of the cation in LNO. In fact the occupancy was refined for the Li and Ni which confirmed to have at about 2% exchangeable Li and Ni. Subsequently while charging the refinement is improved. It looks like the structure is ordered due to the potential.

Figure 51 shows the variation of a and c lattice-parameters and the c/a ratio during the electrochemical delithiation. Where the lithium content is indicated with 1-x and x is the quantity of lithium removed during the charge.

The data reveals that the initial structure of $Li_{1-z}Ni_{1+z}O_2$, disordered in the pristine remains like this when the charge is start. Even if the lattice parameters are increasing during the charging process, in the beginning a sort of random variation in the *c* and parameters can be seen up to x=0.2.

At the point, where x equals 0.59, the maximum *c* parameter 14.6310(0) Å is reached. That corresponds to a capacity of 162 mAh/g at 4.04 V In comparison in the pristine state the c lattice parameter was 14.3803(0) Å. The *c* parameter in fact is increasing on the z direction during the delithiation, however, the variation for *a*, which is changing from 2.9153(3) Å to 2.8641(0) Å, is smaller ($\Delta a \sim 0.05$ Å, $\Delta c \sim 0.25$ Å), indicates also a significant change. In fact

the *c* and *a* parameters seems to be modified in a proportional way. Subsequently, up to 4.25 V vs Li^+/Li the parameters are decreasing in a proportional way, with *c* 14.2663(9) Å and *a* 2.8574(8) Å, maintaining the position for the hexagonal phase. Additionally, the *c/a* is at this point 4.99, this might indicate a well-organized layered phase. Might be assigned in this way to a hexagonal-hexagonal transformation. Additionally, during the transformation at 4.25 V the reflection 003 is splitting, however, cannot be really identified if the transformation is just hexagonal-hexagonal or it passed through monoclinic one. In fact the refinement with the monoclinic one (C2/m) and the hexagonal one (R-3m) fit better the XRD-pattern. Another phase that might be possible to fit was the spinel phase, which was excluded after the mismatching with the positions.

After the adjustment of the structure was possible to assign the phase better due to the well-defined intensity that was increasing. In fact, up to 4.75 V is continuing with the delithiation with an identified stoichiometry of $Li_{0.11}NiO_2$ and the complete the delithiation is identified to be after 4.89 V.

However, the structure was changed, the refinement was done with the hexagonal phase for NiO_2, which remains stable also at high potential. Therefore, the lattice parameters were obtained for the R-3m phase of NiO_2 (Figure 51).

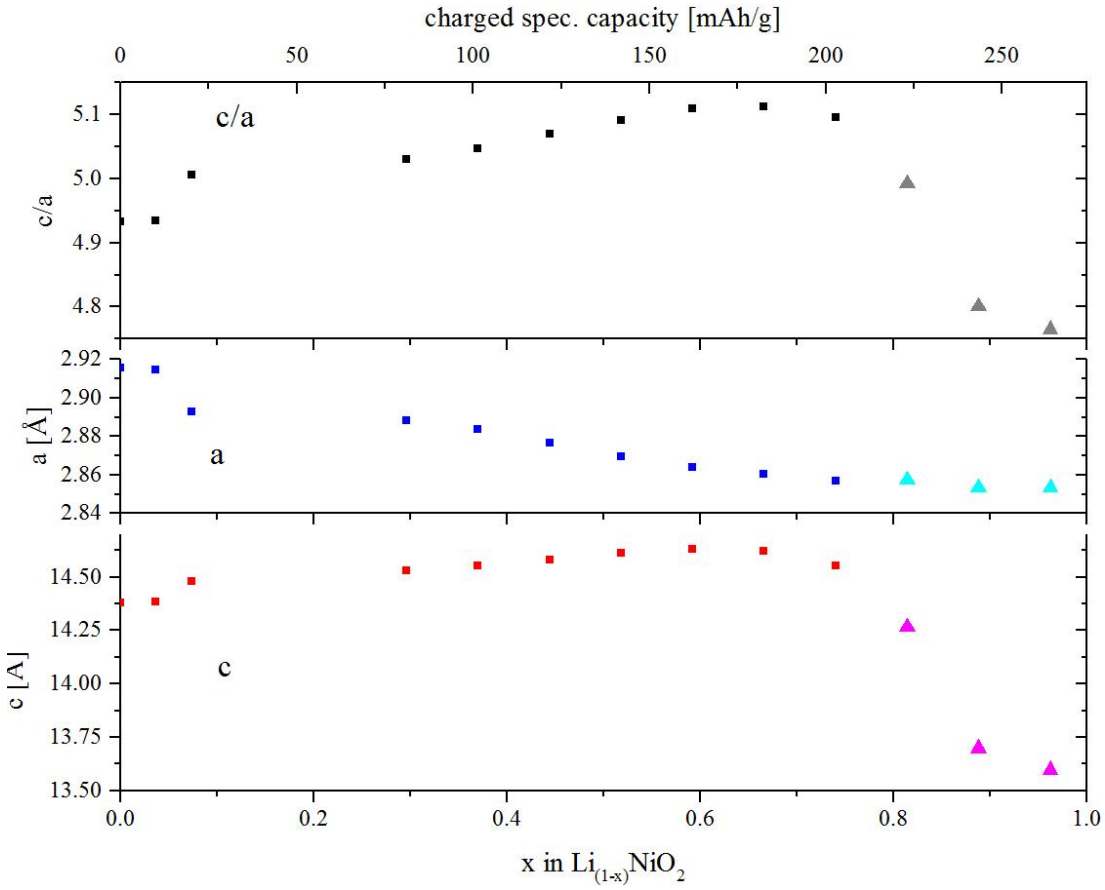

Figure 51 Variation of lattice parameters *a*, *c* and ratio *c/a*, subsequent of the Rietveld refinement of the $LiNiO_2$, in the hexagonal space group (R-3m) during delithiation.

Additionally, in-situ XRD pattern were recorded with C/10, of this the raw data are shown in Figure 52. The evolution of the reflections is similar to that observed for the C/20-cycling. Therefore it was renounced to an additional refinement.

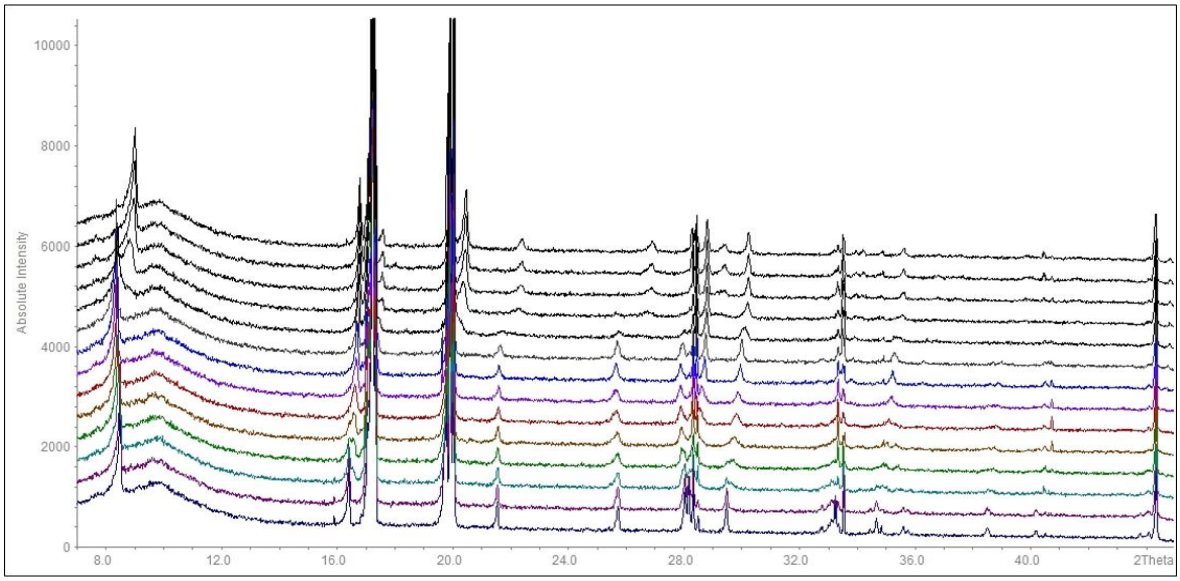

Figure 52 : Raw-data of the in-situ XRD measurement of pouch-cell LNO vs Li^+/Li charged at C/10 up to 4.8 V.

5.3.2 In-situ OEMS

For the gas analysis of the first charge, a OEMS-cell was built as described in chapter 3.8.2 with an LNO with a loading of 2.6 mg/cm².

Figure 53 shows the OEMS data obtained while charging LNO at C/10 up to 4.8 V. In the upper part of the graph the potential of the cell is shown, while in the middle of the graph the concentration of CO_2, CO and H_2 are shown, which are the main interest. In the last panel, the calculated gas evolution rate for this gasses is shown.

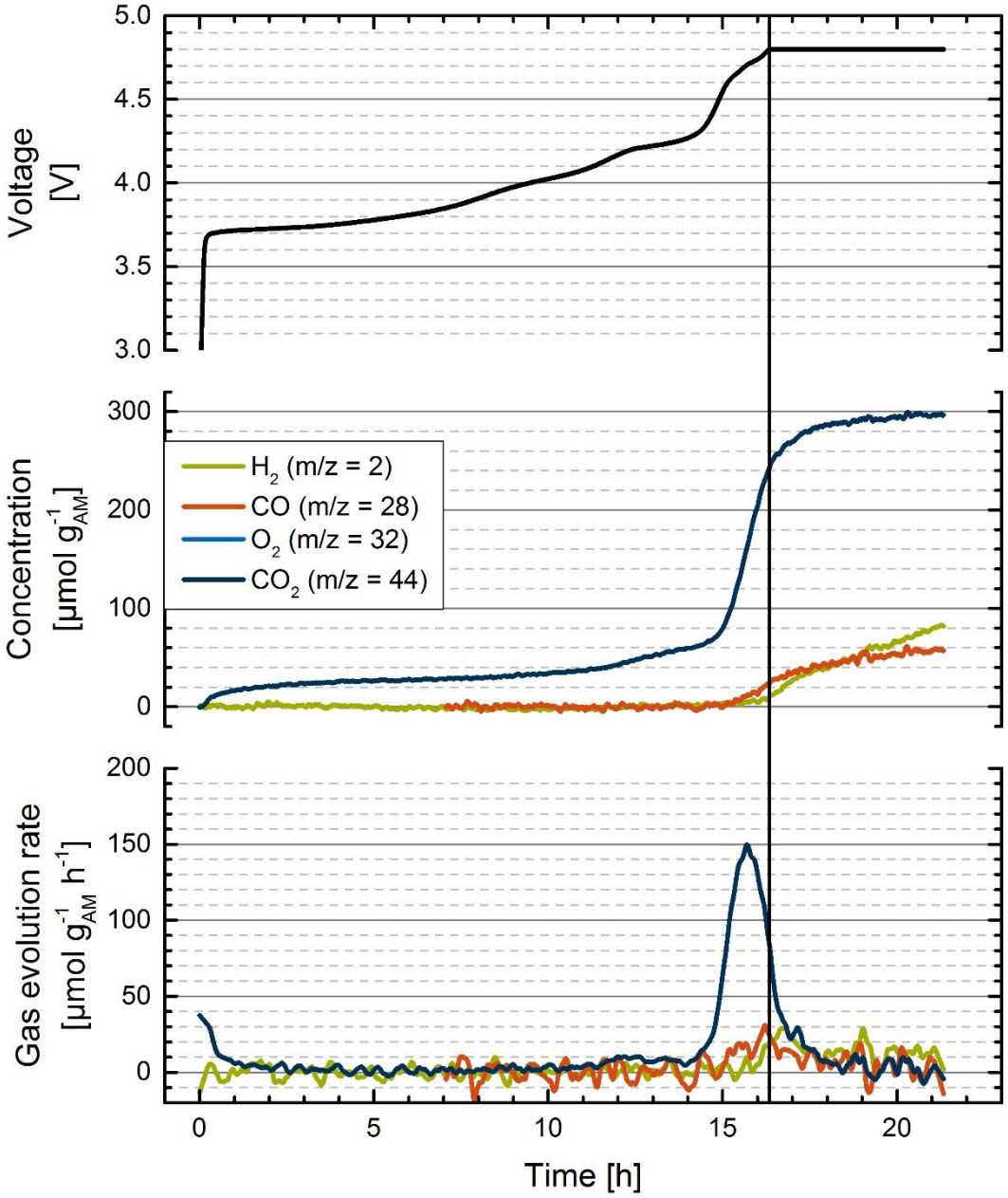

Figure 53 OEMS measurement of LNO vs Li^+/Li, charged at C/10 up to 4.8 V. Upper panel shows the voltage curve of the cell, in the middle the gases evolved with the gas evolution rate in the below one.

The CO_2 evolution starts at 4.2 V followed by a continuous increase up to 4.8 V and continuing also during the CV step. However, at 4.6 V the evolution rate arrived at maximum starts to decrease.

The CO and H_2 evolution start slightly before 4.8 V, this can be correlated with the decomposition of the organic electrolyte as discussed for the LCO and with the structural change as shown in the in-situ XRD (chapter 5.3.1).

6 Synthesis of $LiNi_{0.5}Co_{0.5}O_2$ and characterization

6.1 Sol-gel-water synthesis and characterization

The water sol-gel synthesis, successful for LCO and nearly stoichiometric LNO, was implemented also for the mixed $LiNi_{0.5}Co_{0.5}O_2$ (LNCO). The formation of the sol-gel was identically as for the LNO and LCO.

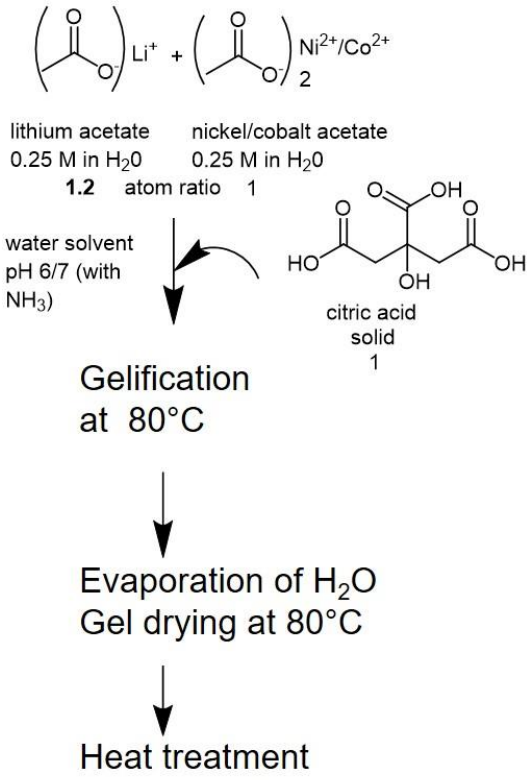

Figure 54: Schematic representation for the LiNi0.5Co0.5O2 synthesis via sol-gel using water as solvent.

A lithium-cobalt-nickel-citrate gel precursor was obtained following the same procedure described in chapter xx. $Li(CH_3COO)$ (Sigma Aldrich, 99.99%), $Ni(CH_3COO)_2*4H_2O$ (Sigma Aldrich, >99.0%), $Co(CH_3COO)_2*4H_2O$ were used in an atom ratio of 1.2 : 0.5 : 0.5 as metal oxide sources, citric acid was used in a molar ratio of 1 in relation to the sum of metal as chelating agent. The formation of the gel follows the same steps as described in Figure 54, the pH was corrected to 6.5-7.0 with ammonium hydroxides.

In the case of the LNCO for the thermal treatment it was decided due to the usage of nickel to perform the same heating treatment as for the LNO, as described in chapter 5.1 in Figure 40.

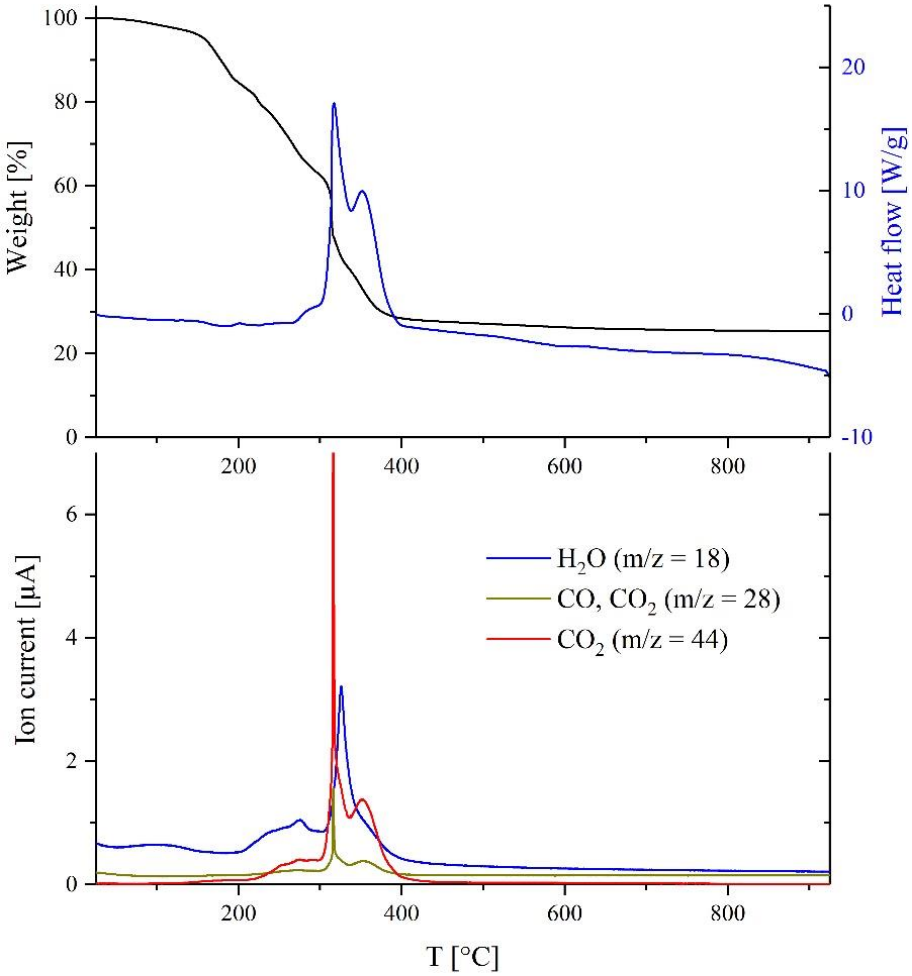

Figure 55: Thermogravimetric analyses and mass spectrometers (TGA-MS) of gel precursor for LiNi0.5Co0.5O2 at heating rate of 10 °K/min.

Even if the DSC signal of the TGA/MS measurement shows two different important peaks near one to each other. Where the first and second are in the range of 300-340 °C and subsequently 340-415 °C. Additionally the mass spectrum confirms the decomposition of the complex agent with the evolution of CO_2, CO and obviously, H_2O due to the solvent.

In fact, might be possible to use the same heat treatment as for the LCO and the synthetic air atmosphere.

Overall the XRD pattern of the obtained LNCO-powder shown in Figure 57 shows a good crystallinity. The stoichiometry of the sample was identified by phase-matching with ICCS data base to be $LiNi_{0.5}Co_{0.5}O_2$ (PDF 01-072-8321). The SEM pictures in Figure 56 show the gel morphology after the annealing (B). In addition, the range of the particle size can be determined, by counting a significant number of particles in the SEM picture. It is deduced to be between 3 and 4 µm. To ensure that this result is reliable, the specific surface area of the LNCO was investigated with BET and an average particle size was calculated with the

assumption of spherical particles, as described in the chapter 2.3. This resulted in an average particle size of 3 µm consisted with the SEM evaluation.

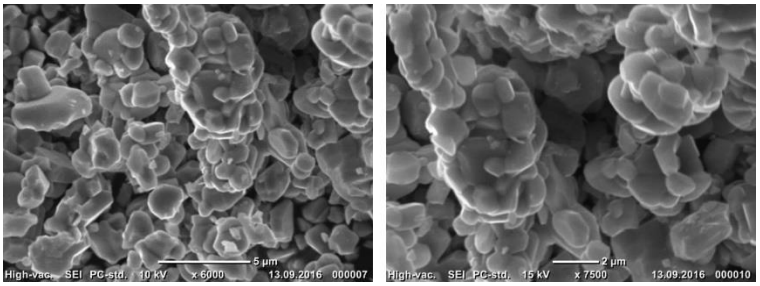

Figure 56: SEM-pictures of the gel for LNCO and after the final annealing.

The BET, surface area measured as described in the chapter 3.3, was identified to be 0.4 m^2/g.

Subsequently Figure 57 shows the Rietveld profile for the LNCO. The profile fits the XRD pattern with the crystallographic structure based on the α-$NaFeO_2$, with a space group R -3m.

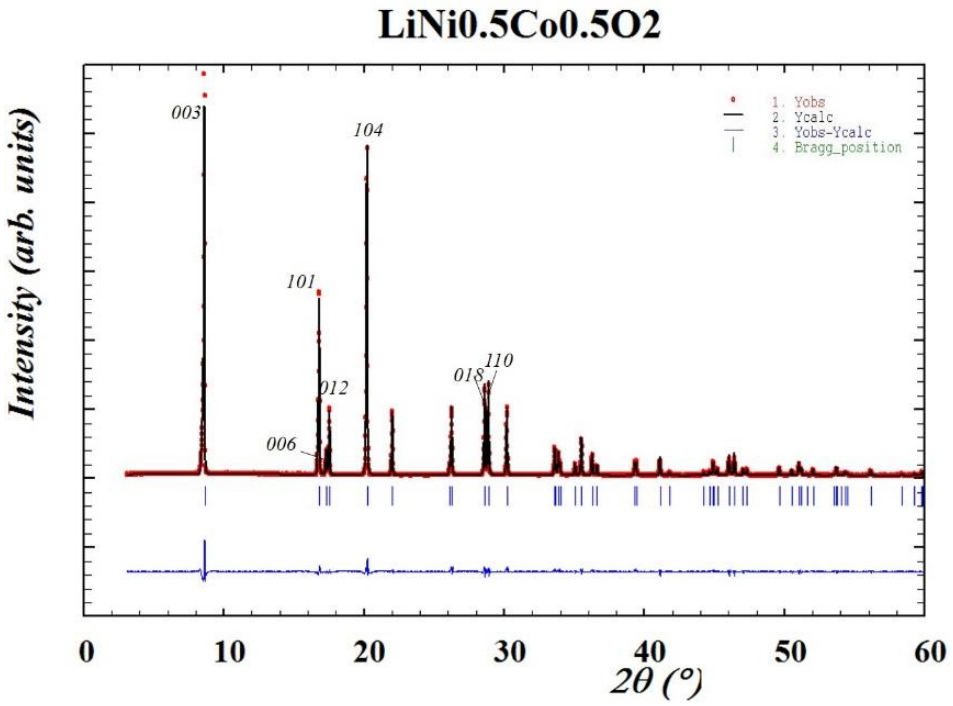

Figure 57 Rietveld of the XRD of LNCO synthesized with sol-gel water synthesis.

The hexagonal lattice parameters, *c/a* ratio and intensity ratio I_{003}/I_{104} of the 003 and 104 peaks are given in the Table 4

Table 4: Results of Rietveld Refinement of the LNCO synthesized with sol-gel water.

#	**$LiNi_{0.5}Co_{0.5}O_2$ – sol-gel water**
c	14.12459(5) Å
a	2.84287(7) Å
c/a	4.97
I_{003}/I_{104}	1.2

The XRD patterns and the hexagonal *a* and *c* match well with the LNCO reported in the literature *a* =2.84287(7) Å; *c* = 14.12459(5) Å. The 006/012 and 018/110 peaks are correlate to a perfect layered structure, in this pattern are well-resolved. Even if, the *c/a* ratio is 4.97, slightly deviated from the 4.99 assigned usually to a well-ordered structure and the fact that the intensity ratio of I_{003}/I_{104} is 1.2 confirms that this structure maintains the order structure.

Since only one sample was successful synthesized all the data are given for this sample.

6.2 Electrochemical characterization

The Figure 58 shows specific discharge capacity of the rate capability and cycling test for the LNCO ($LiNi_{0.5}Co_{0.5}O_2$) for two different compositions of the LNCO electrodes, which were measured in half cells with Li anodes. For better comparison of the different electrodes only the discharge capacity is plotted, which is relevant for the use of a battery. The theoretical capacity of LNCO is 274 mAh/g, if the AM would be 100 % delithiated, but for calculating the C-rate a specific capacity of 155 mAh/g is used, which corresponds to an extraction of Li of x = 0.58 in $Li_{1-x}Ni_{0.5}Co_{0.5}O_2$. The upper cut of potential is set to 4.2 V vs. Li/Li^+, which is the same as for LCO and LNO.

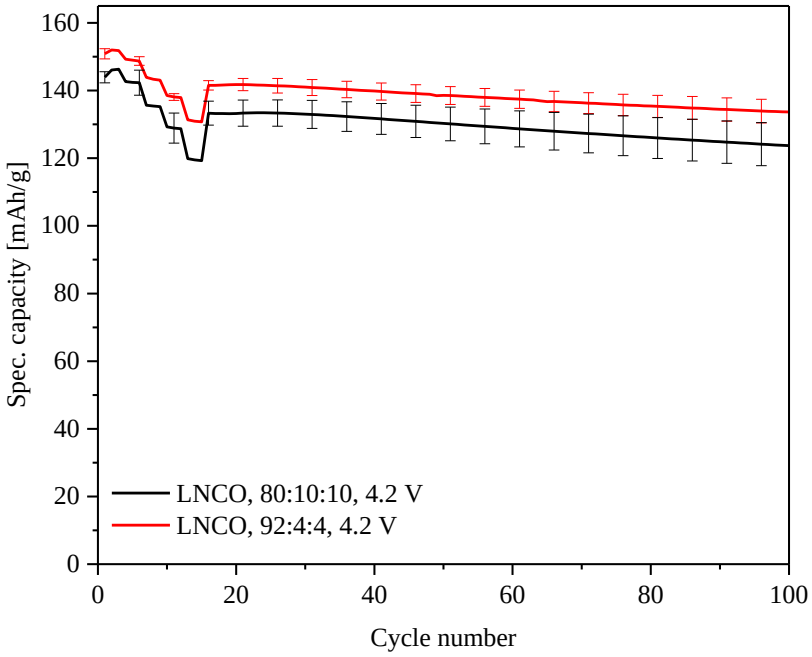

Figure 58: C rate test at C/10, C/5, C/2, 1C, 2C and cycle at C/2 for 100 cycles of LiNi0.5Co0.5O2 with inks with 80 % or 92 % active material. For each composition, the average values of 3 cells with standard deviation are shown.

The red curve shows the average specific capacity and standard deviation of 3 cells of electrodes made with the Thinky mixer with 92 % AM, as described in chapter 3.5. The C-rate test (described in chapter 3.7) starts at C/10, the initial discharge capacity of the LNCO at this C-rate is 152 mAh/g. After 100 cycles in total the measured specific capacity at a C-rate of 2 C was 134 mAh/g, which is 88 % of the initial value. However, if looking at the conservation of the energy at the same C-rate, 2C it starts with 142 mAh/g and ends at 134 mAh/g, with a really good conservation of capacity, only 6 % of capacity loss.

The black curve shows the average specific capacity and standard deviation of 3 cells of electrodes made with 80 % AM.

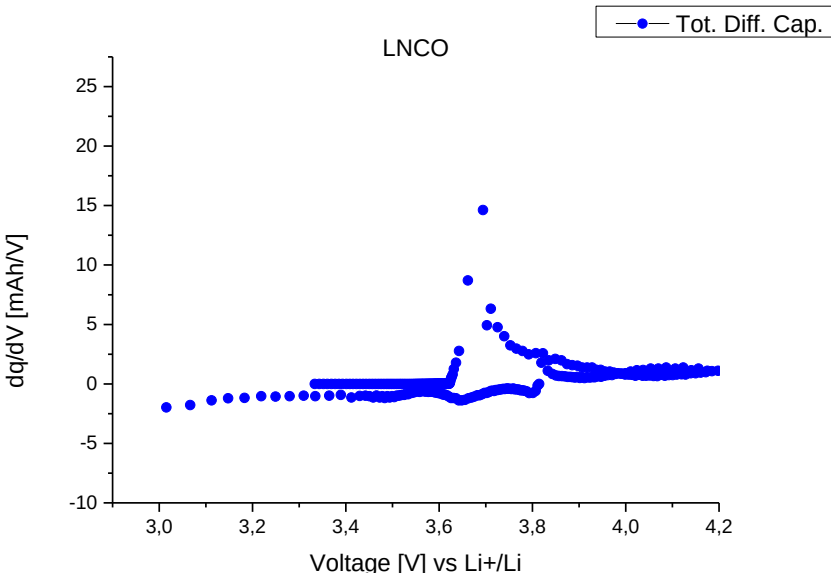

Figure 59: dQ/dV-plot for LiNi0.5Co0.5O2 vs Li^+/Li, assembled in a Swagelok cell, 1st charge and 1st discharge.

6.3 In situ measurements on LNCO

6.3.1 In-situ XRD

The set-up of the pouch cell was realised as mentioned in chapter 3.8.1 with a LNCO electrode with a loading of 3.03 ± 0.01 mg_{LNCO}/cm^2. This set-up allowed to record continuously XRD patterns (shown in Figure 60) during the first C/20 charge up to 5.0 V. The XRD pattern were recorded in transmission mode as described in chapter 3.8.1.

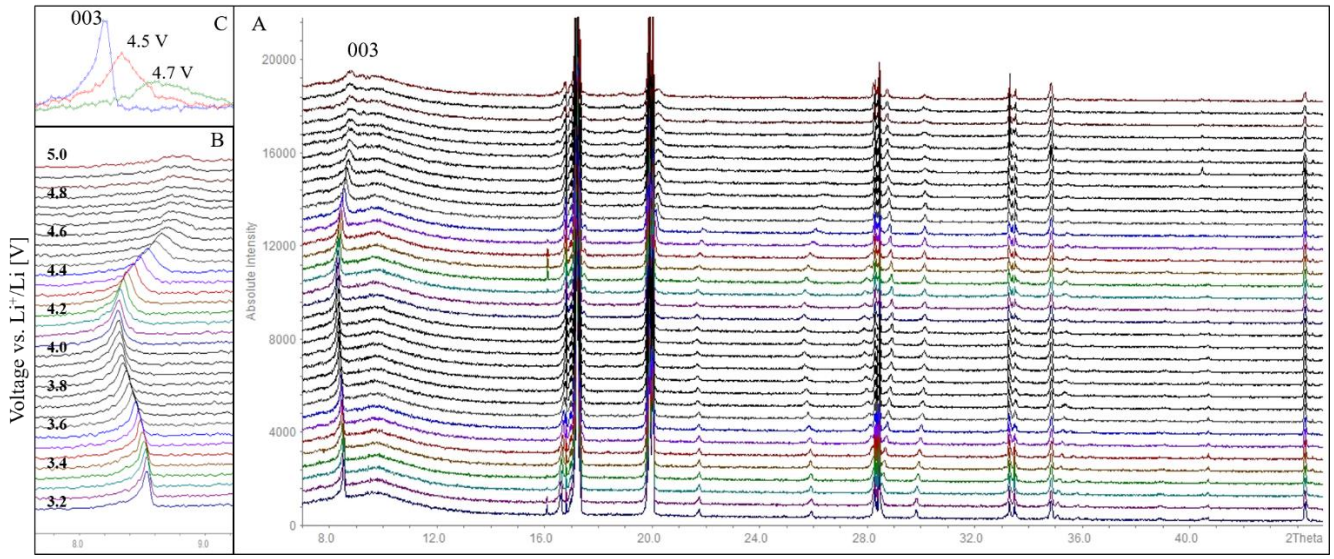

Figure 60:Raw-data of the in-situ XRD measurement assembled in the pouch cell LNCO vs Li^+/Li, charged at C/20 up to 5.0 V. A: Complete set of the in-situ XRD data, with the attention on the 003 reflection. B: Zoom on the 003 reflection while charging. C: 003 reflection, the amorphous pattern after 4.7 V (green curve).

The potential curve of the in-situ XRD charging the cell of LNCO vs. Li with C/20 is shown in Figure 61. This is identical to the results of LNO charged in the Swagelok cell.

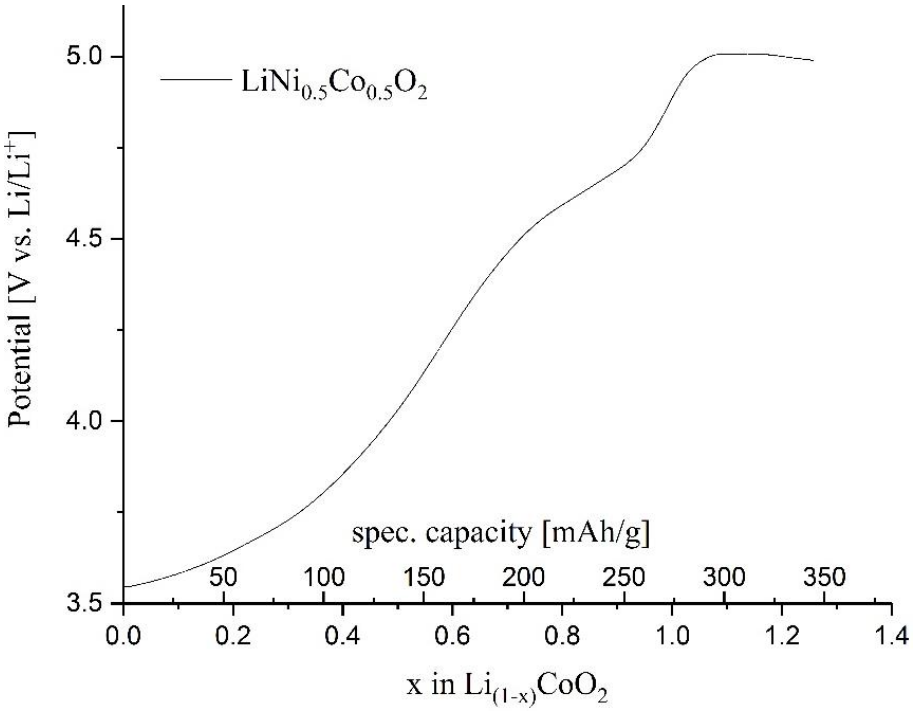

Figure 61: Charge curve for the pouch cell LNCO vs Li^+/Li during the in-situ XRD collection charged with C/20.

Considering the exchanged amount of electrons, the variation of x in $Li_{1-x}Co_{0.5}Ni_{0.5}O_2$ was calculated to be 0.035 till the end of charge. X indicates the degree of delithiation and x = 1 means the cell was charged with the maximum theoretical capacity (274 mAh/g). Before starting the electrochemical cycling of the cell, an XRD pattern was collected in the pristine state. The result is shown in Figure 62. By comparing the observed reflection positions of the LNCO electrode with the standard capillary measurement of the pure LNCO powder, a good agreement between both diffraction patterns can be recognized. As for the other LMO_2, all additional reflections in the upper pattern can be assigned to the aluminium current collector or to the aluminium containing pouch foil. Indeed, the same decrease in intensity was observed due to the pouch cell. Nevertheless, the main reflections for the investigation of the LNCO structure, e.g. 003 and 101, can be clearly distinguished.

A first qualitative analysis of the XRD patterns of the pouch cell (cycled with C/20) shows a shift of the 003 and 101 reflections, while all Al-reflection do not change in position. A splitting of reflection 003 into two reflections, observed at 4.57 V vs Li^+/Li, indicates structural changes

at high states of charge. Additional upcoming reflections with a small intensity can be observed also at 19.84 ° and the reflections at 22 ° and 26 ° disappear.

All patterns were analysed using Rietveld refinement. For the cell charged up to 4.63 V, the Rietveld refinements were calculated using the FullProf software package.[58,66] Al (F m-3m), LNCO (R-3m), and Li (I m-3m) were refined according to their space groups. The refined parameters were the scale factor, the specimen displacement or zero shift, the background, the lattice parameters, the profile parameters W and X and the asymmetry.[66] Instrumental reflection broadening was refined with silicon standard and the reflection profile parameters were included in the refinement. The atomic coordinates, obtained from a crystallographic information file (cif), were kept constant. In order to have a better resolution and due to the high intensity of the Al-reflections, this phase was refined first. After that, the Al-reflections were excluded for the subsequent LNCO refinement.

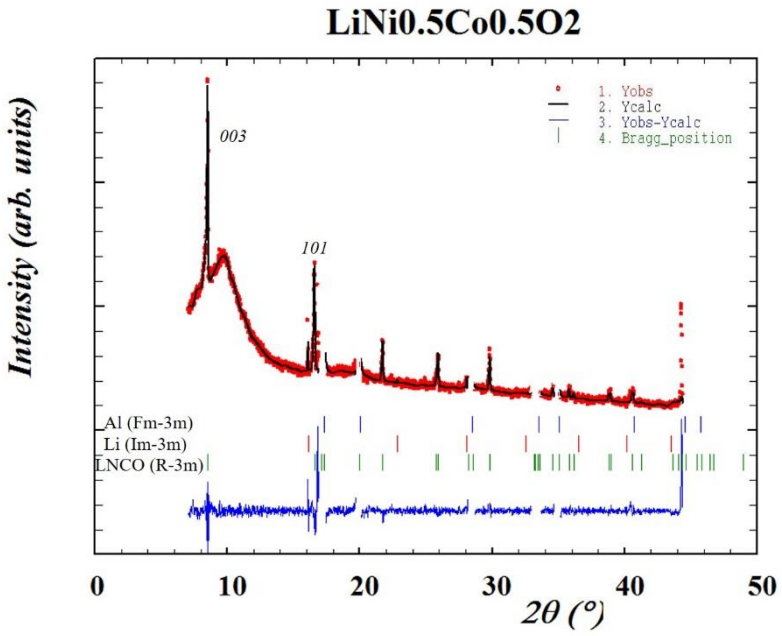

Figure 62: XRD pattern of the pristine LNCO electrode assembled in the pouch cell vs Li^+/Li, cell before charging. Rietveld refinement for the three components. Due to high intensity Al was omit.

The refinement of pristine LNCO is shown in Figure 62. Figure 63 shows the variation of *a* and *c* lattice-parameters and the *c/a* ratio during the electrochemical delithiation. The lithium content in the structure can be extracted as described in chapter 4.5.1.

The data reveals that the initial R-3m structure of $Li_{1-x}Co_{0.5}Ni_{0.5}O_2$ is maintained up to $Li_{0.22}Co_{0.5}Ni_{0.5}O_2$, which is related to a capacity of 213 mAh/g and 4.57 V vs Li^+/Li. For this

structure, x is equal to 0.78, while *c* and *a* parameters correspond to 14.112(1) Å and 2.847(5) Å, respectively.

However, the maximum *c* value and the minimum *a* value are reached at 4.06 V, being 14.686(4) Å and 2.8392 Å, respectively, with x equal to 0.52. The capacity assigned at this point is 141 mAh/g. In the pristine state, the *c* lattice parameter was 14.306(8) Å and *a* was 2.877(7) Å. The overall variation of the lattice parameters are $\Delta c \sim 0.4$ Å and $\Delta a \sim 0.04$ Å. Until x reaches 0.84, at 4.63 V it is possible to see the decrease in the c parameter using the hexagonal phase during the refinement. Even up to 4.73 V at x=0.91 the position was maintained, however it was not possible to discriminate the real reflections clearly. The hexagonal-hexagonal transformation at 4.5 V is reliable.Figure 60

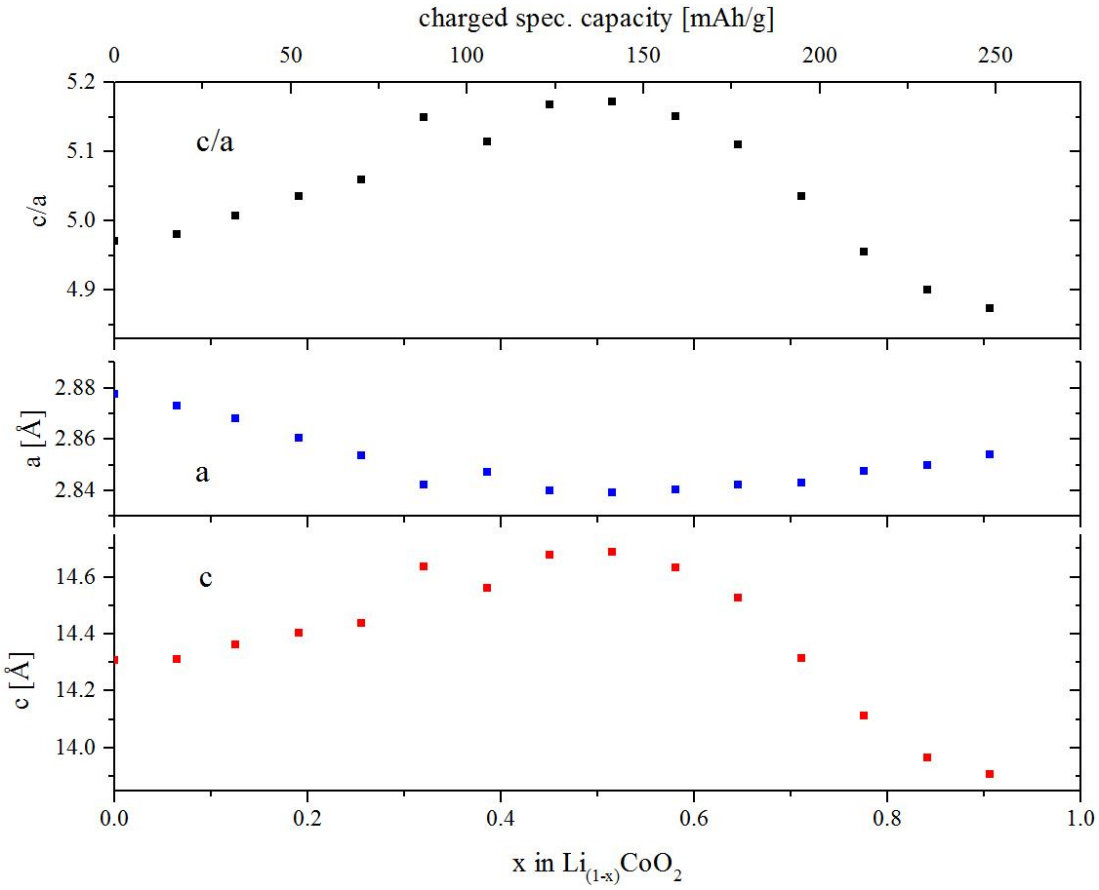

Figure 63 Variation of lattice parameters *a*, *c* and ratio *c/a*, subsequent of the Rietveld refinement of the $LiNi_{0.5}Co_{0.5}O_2$, in the hexagonal space group (R-3m) during delithiation.

Additionally, in-situ XRD patterns were recorded with C/10, shown in Figure 64. The evolution of the reflections is similar to that observed for the C/20-cycling. Therefore, an additional refinement was not necessary.

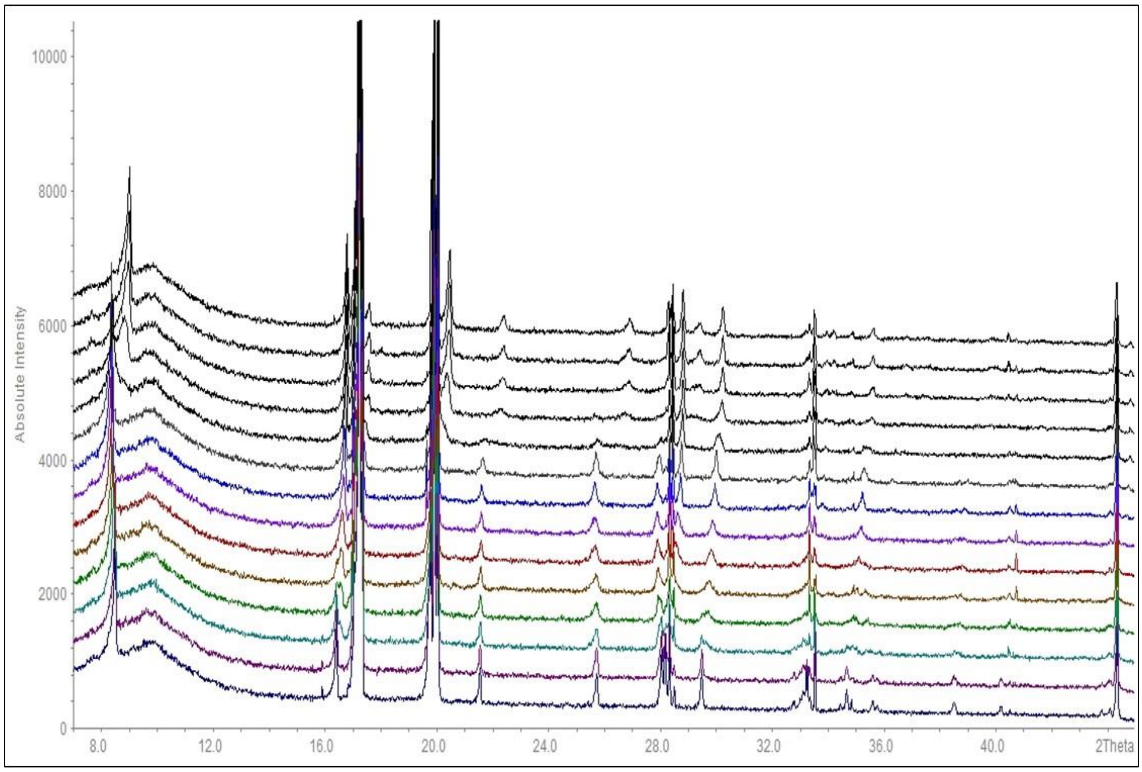

Figure 64: Raw-data of the in-situ XRD measurement of pouch-cell LNCO vs Li^+/Li charged at C/10 up to 5.0 V.

6.3.2 In-situ OEMS

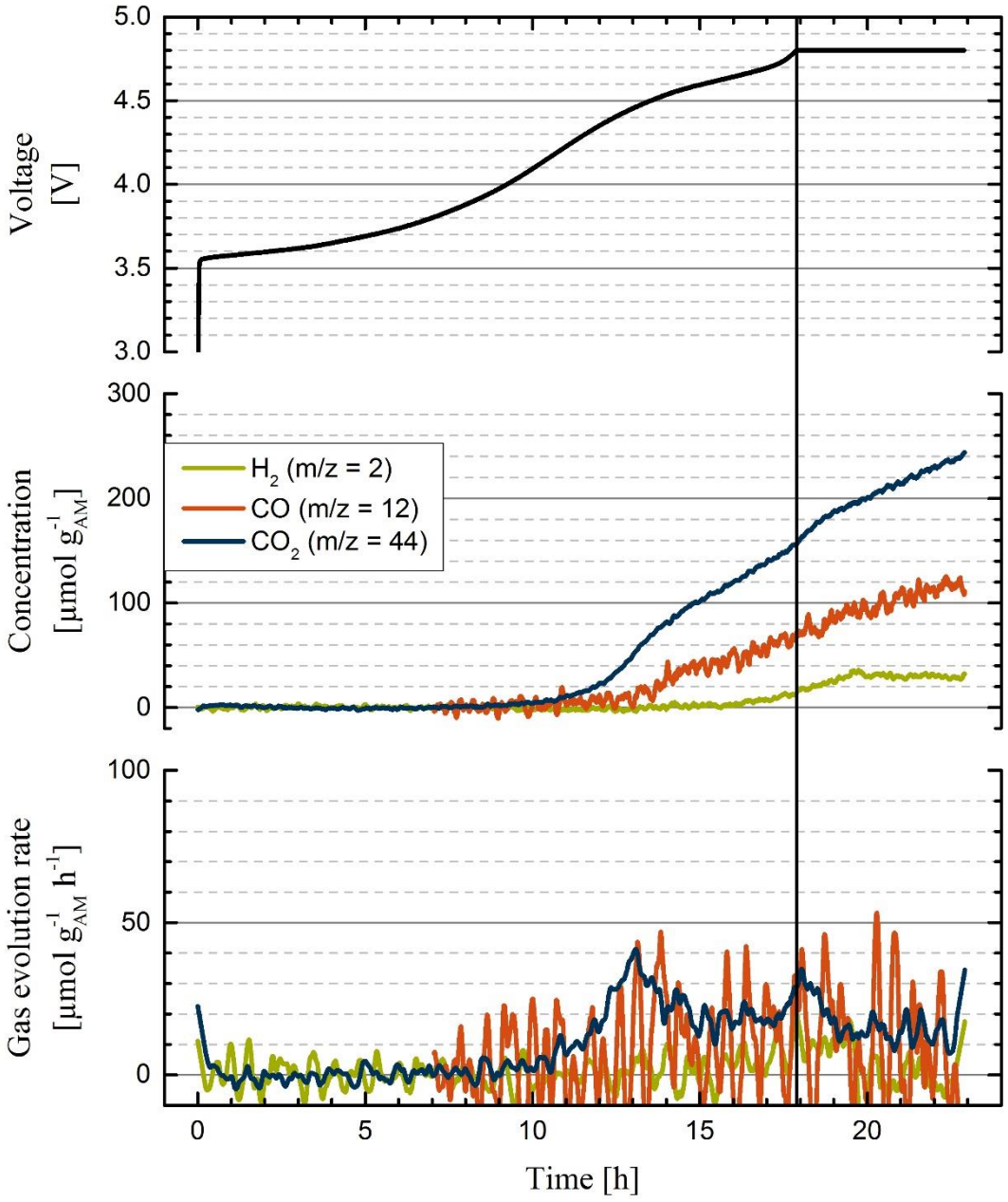

Figure 65 OEMS measurement of LNCO vs Li^+/Li, charged at C/10 up to 4.8 V. Upper panel shows the voltage curve of the cell, in the middle the gases evolved with the gas evolution rate in the below one.

For the gas analysis of the first charge, an OEMS-cell was built as described in chapter 3.8.2. The LNCO prepared as described in chapter 3.8.2, was used resulting in a loading of 2.83 mg/cm².

Figure 65 shows the OEMS data obtained while charging LNCO at C/10 up to 4.8 V. In the upper part of the graph the potential of the cell is shown, while in the middle of the graph the

concentration of CO_2, CO and H_2 are shown, which are the main interest. In the last panel, the calculated gas evolution rate for this gasses is shown.

The CO_2 evolution starts at 4.2 V followed by a continuous increase up to 4.8 V and continuing also during the CV step. At the same potential, however, seems that the CO starts the evolution at 4.2 V. The problem is that with the same m/z is the N_2 and was detected an air intrusion.

The H_2 evolution starts slightly before 4.8 V, this can be correlated with the decomposition of the organic electrolyte, same expected for the CO, as shown by Zhang et al.[70] and with the structural change as shown in the in-situ XRD (chapter 6.3.1).

7 Results and Discussion

7.1 Synthesis and electrochemistry of LMO_2

$LiCoO_2$, $LiNiO_2$ and $LiNi_{0.5}Co_{0.5}O_2$ were synthesized and characterized as described in the following section. All 3 precursors were prepared successful via water assisted sol-gel synthesis with citric acid as complexing agent. The morphology seen by the SEM pictures (chapter 4.3, 5.1 and 6.1) result in a polymer frame and from the SEM pictures of the product, it is possible to distinguish just the distribution of the particles. For LNO the heat treatment was changed due to the instability of the Ni^{3+} in air atmosphere to oxygen atmosphere. In the case of LNO and LNCO this ensured phase purity. However, as reported by Julien et al.[21] for the LNCO, it should be possible to obtain microcrystalline powder and phase pure material also in air. Nevertheless, it was decided to use the same heat treatment as for LNO for the synthesis of LNCO.

Before performing the heat treatment, TGA/MS experiments were used to identify the range of the temperature where the decomposition of the complexing agent is finished. The results are shown for each material in the respective chapter 4.3, 5.1 and 6.1.

After performing the heat treatment, all the obtained LCO, LNO and LNCO products were microcrystalline. The BET surface area and particle size are reported in the Table 5. The pure LCO with 3-4 µm particle size and BET 0.4 m^2/g is comparable to LNCO (3 µm and 0.3 m^2/g BET surface area). LNO has smaller particle size (1 µm) and therefore a higher BET surface area of 1.5 m^2/g. For LNCO (Ni : Co = 1 : 1) it can be therefore deduced that Co is the dominant element considering the morphology of the powder.

Table 5. BET surface area and particle size for LiCoO2, LiNiO2 and LiNi0.5Co0.5O2. powders calcined in air at 750 °C, oxygen at 800 °C and oxygen at 800 C, respectively.

#	**$LiCoO_2$**	**$LiNiO_2$**	**$LiNi_{0.5}Co_{0.5}O_2$**
BET	0.4 m^2/g	1.5 m^2/g	0.3 m^2/g
Particle size (BET and SEM)	3-4 µm	~1 µm	~3 µm

The XRD patterns for all the three materials are shown in each chapter (4.3, 5.1 and 6.1). The reflections of all materials can be indexed based on a hexagonal α-$NaFeO_2$ structure with the space group R-3m. Therefore LCO, LNCO and LNO are isostructural.

In a R-3m-structure the oxygen ions are close-packed in rhombohedral arrangement. The metals M (M=Co,Ni) and the Li-ions occupy octahedral sites in alternating layers with an ABCABC stacking sequence, called also "O_3-type" structure, introduced by Dahn et al.[52] Assuming an ideal ordered rhombohedral structure, Li^+ and Co^{3+}/Ni^{3+} ions are located in 3*a* and 3*b*, respectively. Oxygen occupies 6*c* sites. The unit cell is shown in Figure 1.

The lattice parameters (hexagonal setting) of the three, pristine materials, derived by Rietveld Refinement, are shown in Table 6. In this analysis, the attention was focused on disorder due cation mixing, which is well known from literature, especially in the case of Ni-containing sample.[32,73] In fact Ni^{3+}(0.56 Å) can easily be reduced to Ni^{2+} (0.68 Å) and tend to migrate into Li-positions (Li^+: 0.76 Å). Co^{3+} (0.545 Å) is more stable and has no tendency to migrate, resulting in a well-organized structure.[21]

Table 6: Results from Rietveld Refinement for LC), LNO and LNOCO.

#	**$LiCoO_2$**	**$LiNiO_2$**	**$LiNi_{0.5}Co_{0.5}O_2$**
c	0.4 Å	0.25 Å	0.4 Å
a	0.006 Å	0.05 Å	0.04 Å
c/a	4.99	4.93	4.97
cation mixing	No	~ 3 %	No
I_{003}/I_{104}	1.27	1.15	1.21

In $LiNi_{0.5}Co_{0.5}O_2$ the structural properties of Co dominate as the structure is well organized. This was already seen before by discussing the characterization of the powders. This observation is also confirmed by the *c/a* ratio (Table 6) and by the splitting of the 006/012 and 108/110 reflections as shown in Figure 60. A clear split in the LCO and LNCO is observed while the reflections are overlapping in the case of LNO. Moreover, the indication of disorder in LNO is confirmed with the Rietveld Refinement that fits better after considering the cation mixing between Li^+ and Ni^{2+}. In fact, about 3 % of Ni^{2+} occupies octahedral sites in the Li layer (3a) and the stoichiometry is better indicated with $Li(3a)_{1-z}Ni(3a)_zNi(3b)_{1-z}Li(3b)_zO_2$, $0.00 \leq z \leq 0.02$.

As it is well known, the distinction in size, morphology and surface area would lead to differences in their electrochemical performance and all are closed linked with the synthesis

routes.[32,36] In order to analyse the electrochemical performance and to correlate the difference only with the change of the cation, less parameters were modified during the synthesis, as pH for the better dissolution of the educts and the atmosphere of calcination.

7.2 Electrochemistry of LMO_2

The electrochemical properties of cathodes based on LCO, LNO and LNCO, which are cycled in half cells against Li anodes are shown in Figure 66 and Table 7, respectively.

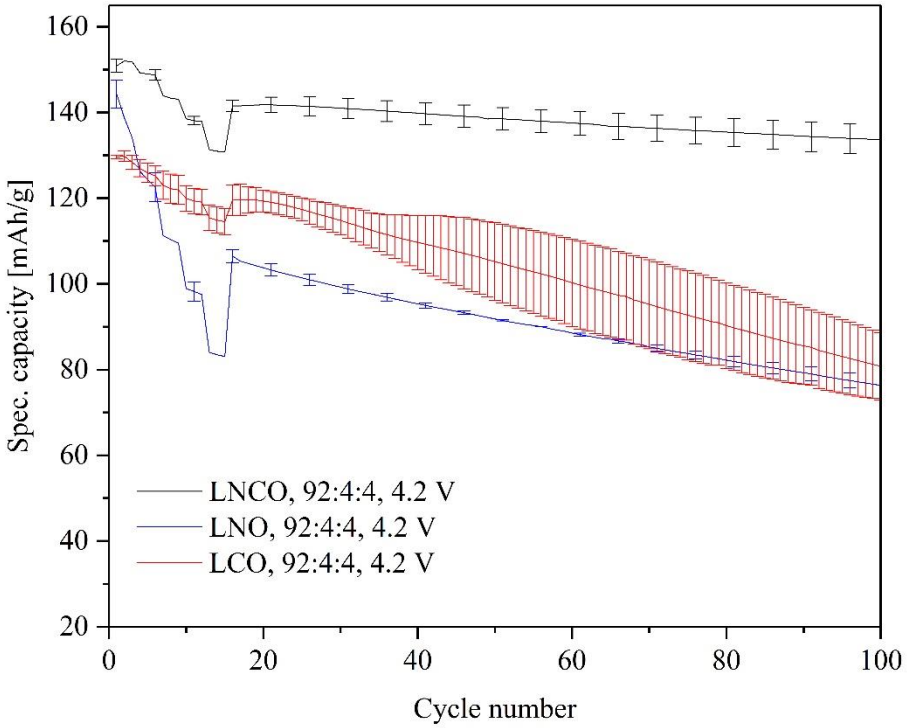

Figure 66: C-rate test, with C/10, C/5, C/2, C, 2C and lifetime at C/2 up to 100 cycles for LiCoO2, LiNiO2 and LiNi0.5Co0.5O2 electrodes vs Li+/Li. Applied 4.2V as cut-off. The specific capacity was 150 mAh/g for LCO, 160 mAh/g for LNO and 155 mAh for LNCO.

The LCO, which is claimed to show a better cycling stability than the others is the worst one in terms of capacity retention. Thus it is important to understand which factor influenced this, considering that it is cycled up to 4.2 V, which is a high cut-off limit. However, the self-synthesized LCO is in terms of cycling not comparable to the commercial one, even if the only obvious difference which was seen is particle size and distribution.

Furthermore, the data of cycling are in accordance to the literature.[18,36] Two different coatings were tested, where the ink was prepared with ball-mill or the thinky mixer, to make a nice ink with good particle size distribution and homogeneous distributed material in the electrode.

Moreover, two different compositions of the ink, 92 : 4 : 4 and 80 : 10 : 10 were tested, but with no significant influence to the performance, as shown in Figure 28.

In Table 7 all the data are reported only for the ink with 92 : 4 : 4 which was used in the in situ-XRD characterization. The importance of the first cycle is taken into consideration and the capacity loss after 100 cycles at 2C, which were performed after the rate capability test. A capacity loss in the first cycle is expected due to SEI formation, but not in this quantity. For the LCO, a difference of 10 % between the first charge and discharge capacity can be noticed with a subsequent loss of 37 % after 100 cycles. LNO shows 25 % difference for the first charge/discharge cycle and 47 % capacity loss after 100 cycles, as expected. Finally, for the LNCO the difference is about 21 % for the first charge/discharge, but showing a good cycling stability, loosing after 100 cycles only 11 % capacity.

Table 7: Charge and discharge capacity of the first cycle of LCO, LNO and LNCO (electrodes with 92 % AM) and discharge capacity after 100 cycles.

#	**$LiCoO_2$**	**$LiNiO_2$**	**$LiNi_{0.5}Co_{0.5}O_2$**
1st Charge capacity	141 mAh/g	191 mAh/g	190 mAh/g
1st Discharge capacity	127 mAh/g	144 mAh/g	150 mAh/g
Capacity (100 cycles)	80 mAh/g	76 mAh/g	134 mAh/g

Another difference can be identified in the specific capacity, as all the compounds have the same theoretical capacity of 274 mAh/g. It is known from the literature that the well-organized structure is more suitable for the reversible insertion of the Li^+ in the structure and leads to a better cycle stability. However, the structure was identified to be the right one for all 3 synthesized samples, the morphology and the difference in the particle seem to be the only difference. It is believed that smaller particles are better, however this is not the case for this study. From different synthesis reported in the literature it was reported that the capacity fade is increasing with increasing particle size.[74] On the other hand, the commercial LCO-MTI has bigger particle, but shows better capacity retention while the self-synthesized LCO with smaller particle size shows a less stable cycle life. It is reported that the maximum discharge capacity is independent of the particle size, what seems not to be in accordance with this study.[36]

Additionally, the LNCO sample is comparable in terms of morphology and structure to the LCO, but has in contrast a good retention of the capacity after cycling and in general a higher

specific capacity. The higher specific capacity is attributed to the 50 % nickel in the sample and the cycling stability to the structure, which is found to be stable up to high potential and allows by this a higher degree of delithiation. In fact, it is interesting to note that in terms of capacity loss in the first cycle the LNCO is similar to LNO. The highest capacity loss occurs at the first cycle, after this it is stabilized and cycles well.

On the other hand, a nearly stoichiometric LNO is losing about 25 % of the capacity in the first cycle and during the rate capability test the decrease of the capacity is continuing. This is in accordance with the literature which reports the capacity fade due to the cation mixing occurring in the structure. The disorder in the structure has a negative effect to the capacity fade, but allows a higher capacity.

In fact, Ni is correlated with cation mixing, but contributes to more capacity. Moreover, the higher the concentration of Ni, the higher the specific capacity since the structure is more flexible and allows in the beginning to extract more lithium. On the other hand, this material suffers from such drawbacks as shortage of cycling performance and poor rate capabilities. This might be possible to be attributed also to the migration of Ni from layers to the interlayer space, thereby inducing deterioration of the particles.

7.3 In-situ XRD

The structural properties of LCO and LNO have received high attention from a lot of research groups and for all aspects. The general structure is shown in chapter 1 and is built out of oxygen octahedrons with alternating transition metal- and Li-layers. Thereby the metals are octahedral coordinated by the oxygen atoms. In this arrangement, Li^+ can be removed from the layers to a certain degree assured by the right cut-off potential for a significant lifetime.

At lithium contents lower than x = 0.5 in Li_xCoO_2 the material runs through irreversible phase transformations. The most accepted one is reported by Dahn et al., who proposed a hexagonal-hexagonal transformation at 4.2 V (x=0.5) followed by 2 hexagonal-monoclinic transformations forming CoO_2.[52] The second monoclinic phase at low Li contents was not observed by McBreen et al., who assigned this phase to a hexagonal structure.[18,75] In this work the accordance is more likely for the hexagonal-hexagonal transformation. All the recorded pattern before the sample getting amorphous can be refined only with a R-3m group in an hexagonal form just with a variation in lattice parameter as shown in chapter 4.5.1 in Figure 35.

Thereby the 003 reflection is changing the position up to 4.2 V, this can be seen in Figure 32 C by the reflection before 4.1V and after when is supposed to be completely amorphous at 4.6 V.

For LCO in contrast to Amatucci et al.[76] who affirm that a complete delithiation should leave CoO_2 this was not seen. This was neither for LNCO nor for LCO observed in the present study. Instead of this, the patterns showed a significant decrease in intensity which means that the materials become amorphous (Figure 32 and Figure 60). LCO starts to show the amorphous part at 4.6 V, the structure of LNCO starts to be completely deformed from 4.8 V on.

Similar results as for LCO were reported for LNO, despite that LNO shows a coexistence of hexagonal and monoclinic phases at x lower than 0.6 and higher than 0.5.[54] Moreover, it was stated by Amatucci et al.[18,53] that for completely delithiated LCO and LNO, the CoO_2 and NiO_2 are able to reinsert up to 90-95 % of Li. In fact, the changes in the lattice parameters (volume changes) should be reversible. By using in-situ synchrotron powder diffraction McBreen et al.[54] discussed, if the monoclinic phase in LNO exists while Ceder et al. facilitated the same discussion about LNCO by performing theoretical calculations.[18]

According to literature the transitions are hexagonal-hexagonal phase transformations. Additionally, the splitting of the reflections can be unambiguous assigned to a monoclinic phase.[76]

In the present work Rietveld refinement was performed for the hexagonal phase of LNO and LNCO, which were cycled up to 4.8 respectively 5.0 V, while every 45 min XRD patterns were taken, shown in Figure 48 and Figure 60. The first phase transformation was observed at 4.2 V and 4.5 V with a maximum variation in *c* parameter at 4.2 V, as shown in Figure 51 and Figure 63.

However, the monoclinic phase was also fitting the additional reflections in the pattern, but based on the quality of the Rietveld refinement the hexagonal-hexagonal transformation is more reliable.

The LNCO shows the same trend as LCO considering the phase transformations. However, the potential window of this phase transitions is shifted to higher voltages up to 4.6 V. This is possible due to the presence of Ni, which is resulting in less changes in the volume and the *a* parameter and by this it is much more stable than the pure LCO. Figure 63 shows the evolution of the lattice parameters and the c/a value, while the maximum volumetric changes are reported with in Table 8.

On the one hand, Co improves on layered characteristics of $LiNiO_2$ and reduces the disorder, as was shown by the refinement of the pristine LNCO pattern in Figure 57, on the other hand Ni allows a higher variation of the lattice parameters, especially the *a* parameter, which reduces the microstrain and therefore the material can be charged to higher voltages. With Rietveld refinement of the LNCO patterns no cation mixing was observed in LNCO during the first charge. However, it was reported in literature that disorder occurs at lithium contents x >0.3 in $LiNi_{1-x}Co_xO_2$ during charge.

For LNO two hexagonal-hexagonal transformation at 4.25 V and 4.75 V were detected in accordance with McBrean, as shown in Figure 52Figure 51.[54] However, at 4.25 V the refinement of a monoclinic phase in coexistence with a hexagonal phase is in good agreement with the measured XRD pattern, as shown in Figure 51.

Bianchi et al. and Pouillerie et al. affirm that the phase coexistence and the extension of the change of the unit cell volume upon delithiation strongly depend on the Ni^{2+} content in the Li layer. This indeed explains the possibility of having the monoclinic phase.[18,77]

In contrast to LCO and LNCO, LNO remains in a hexagonal structure till it is completely delithiated to NiO_2 from 4.8 V on, as shown in Figure 51. However, the lattice parameters differ significantly from the pristine ones as shown in Table 8.

By removing 60 % of Li^+ from $Li_{0.975}Ni_{1.025}O_2$, the volumetric change is 1.4 %. The same removal of Li^+ from $Li_{0.992}Ni_{1.008}O_2$ shows a volumetric change of only 0.4 %. However, in this work a variation of 1.8 % was found by removing 60 % of Li^+ and 4.7 % by removing 80 % of Li^+ in accordance with a stoichiometry of $Li_{1-z}Ni_{1+z}O_2$ with $0 \leq z \leq 0.2$.

Table 8: Variation of a and c lattice parameter and change of the volume for LCO, LNO and LNCO during charge of the electrodes.

#	**$LiCoO_2$**	**$LiNiO_2$**	**$LiNi_{0.5}Co_{0.5}O_2$**
Δ*c*	0.4 Å	0.25 Å	0.4 Å
Δ*a*	0.006 Å	0.05 Å	0.04 Å
ΔV max	2.0 %	4.7 %	3.4 %

7.4 In situ OEMS

In situ XRD recorded with C/10 allows to correlate the phase transformation during the complete delithiation with the OEMS measurement since both measurements are recorded at the same C rate. However, the XRD-pattern analysed with Rietveld refinement and thereby showing the evolution of the lattice parameters were recorded at C/20 for having a better resolution. Nevertheless, the C/10-patterns are comparable to the C/20-pattern as shown in chapter 4.5.1, 5.3.1 and 6.3.1.

Figure 67 shows the concentration of CO_2 during the first charge up to 4.8 V for $LiCoO_2$, $LiNiO_2$ and $LiNi_{0.5}Co_{0.5}O_2$. This is the gas evolved in major quantity and is plotted for comparing the three different materials. The other evolved gases were CO and H_2 for all investigated cathode materials.

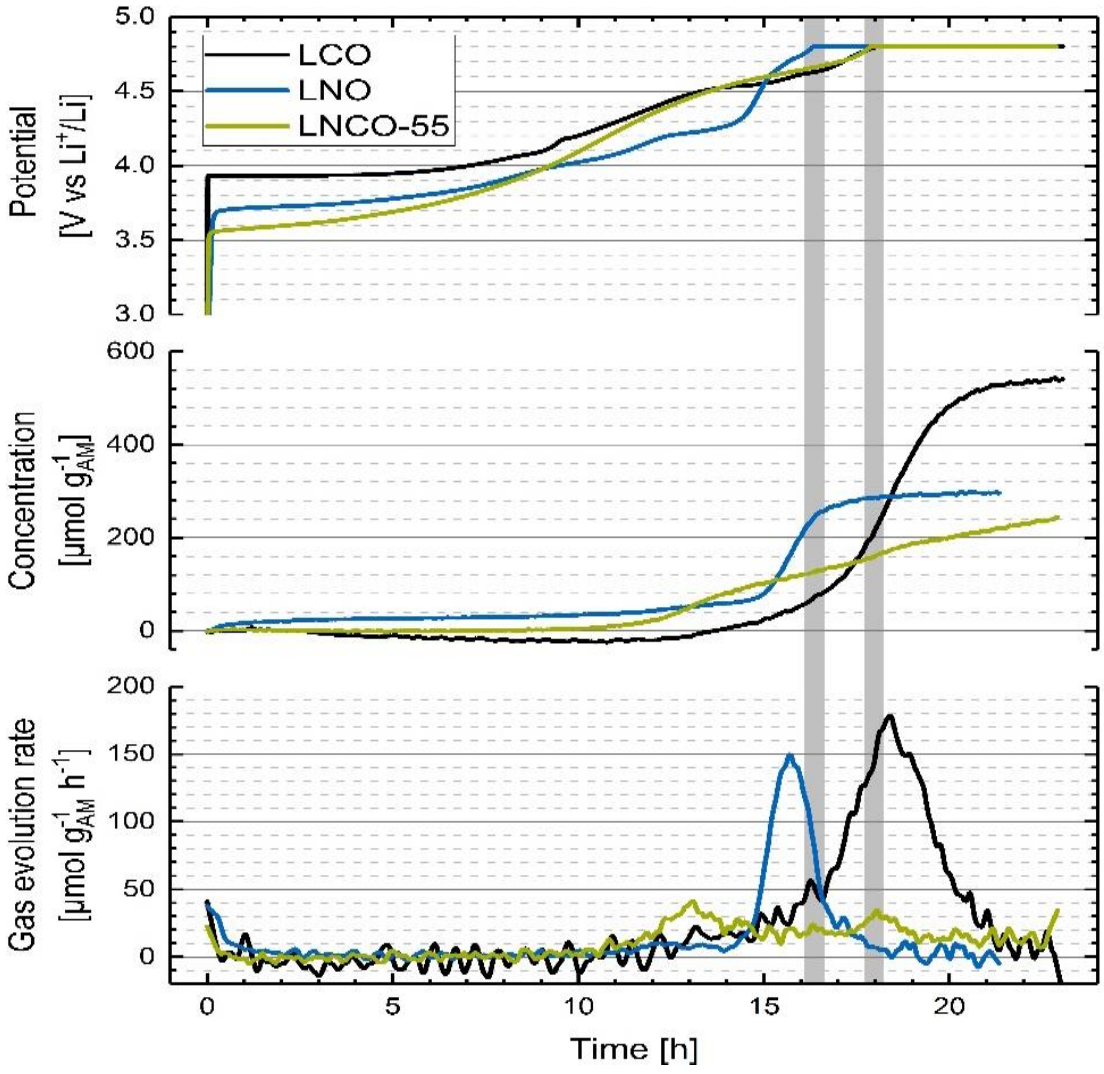

Figure 67. Results of the OEMS measurements for LCO, LNO and LNCO.

Electrolyte decomposition products are the same gases which one would expect to occur if the active material decomposes.[70] In fact, irreversible structural changes of LCO, which start at 4.6 V vs Li^+/Li (see chapter 4.5.1), can be correlated to the decomposition of electrolyte with CO_2, CO and H_2 evolution. Moreover, the LCO shows an amorphization at 4.5-4.6 V, which corresponds to the onset of CO_2 evolution.

LNO and LNCO show the same behaviour as LCO. The gas evolution can be correlated theoretically to structural changes, considering the onset for LNO at 4.3 V and for LNCO at 4.6 V. However, the problem of the electrolyte decomposition remains at 4.6 V and at 4.3 V is also the contribution of the Li_2CO_3.[70]

As mentioned above, all signals can also be ascribed to electrolyte oxidation. LNO for example, shows the first signals of CO_2 at 4.2 V, which is the same potential of Li_2CO_3, assigned by Zhang et al.[61,70] Li_2CO_3 might be an impurity on the surface due to the storage of the material in air, especially for LNO because of a higher surface area of this sample compared to the other materials. In fact, the CO_2 at 4.2 V is observed only in the case of LNO and not detected for LCO and LNCO. Furthermore, for LNO oxygen evolution was expected, which was reported to be expelled from the structure during thermal decomposition or electrochemically during charge, while it is changing from the hexagonal phase to the spinel one.[32] However, no oxygen evolution and also no spinel phase transformation were observed during charge. Moreover, a stable structure of NiO_2 was observed by in-situ XRD from 4.8 V versus Li^+/Li. This might be correlated to the non-evolution of oxygen but sever changes in the lattice parameter. However, the in situ OEMS measurements should be repeated, as one experiment is not reliable, as influences of the environment, the way of assembling the cell or additionally the way of how the baseline correction during the OCV phase is done can influence the results significant. For higher gas signals it would be also desirable to repeat the measurements with higher electrode loadings. Taking into consideration the amount of the gas from the electrolyte, as blank, it should be possible to differentiate the gas evolution of the cathode materials and electrolytes.

8 Conclusion and Outlook

In this work the three different layered oxides $LiCoO_2$, $LiNiO_2$ and $LiNi_{0.5}Co_{0.5}O_2$ were synthesized. The sol-gel-water synthesis route was identified to be the best for producing polymer precursors for all the samples. The heat treatment was adjusted based on the used transition metal, as Ni^{3+} is unstable in air, oxygen atmosphere was used. A systematic way for investigating the materials, which can be applied to the layered oxides as well as for other materials, was reached.

The characterization of the gel was done via SEM and TGA/MS, which allows to identify the decomposition products of the gel during the heat treatment and to adjust based on this the temperature program for the subsequent annealing procedure.

Phase pure materials were obtained without crystalline impurities, which was confirmed by XRD-measurements of the powders and analysed further with Rietveld refinement. The hexagonal phase (R-3m) was synthesized for LCO, LNO and LNCO. By performing Rietveld Analysis significant differences between the pristine materials were observed considering the disorder in the structures. The LCO as expected gives a well-organized structure. On the other part, the nearly stoichiometric LNO shows a cation mixing with Li in the order of 3 %. This was expected due to the small size of Ni, which is similar to the Li-radius. Although LNCO with a Ni : Co ratio of 1 : 1 contains nickel, no cation mixing was identified.

The ratio of Ni : Co is an interesting point for further investigations, since the cobalt is dominant for considering the morphology of the product and nickel showing more influence on the electrochemical performance of the material, and by this the ratio of Ni : Co should be optimized. The presence of nickel is usually correlated with a higher specific capacity but also resulting in a higher capacity fade. Therefore, the disorder might be worth to be investigated for different quantities of Ni in basic layered oxides. Subsequently this could be correlated with the development of the next generation of cathode materials, namely Ni-rich and Li-rich layered oxides, which are highly disordered but offer a huge specific capacity.[7–9,29]

The electrochemical characterization was done with two different composition of the electrodes (80 : 10 : 10 and 92 : 4 : 4 of AM : PvdF : SuperC65) were tested for LCO, LNO and LNCO. The electrodes were investigated with C-rate and lifetime tests in a Swagelok T-cell. Nevertheless, the ink-composition seems to have no influence on the cycling performance of the materials.

Due to agglomerate formation of the LCO powder, two different methods for the ink preparation were tested additionally. Ball milling the ink allows a better particle mixing of the ink and breaks up the agglomerates, but the improvement for the electrochemical behaviour is not significant. Due to this, further improvements of the coating or the annealing should be made for the self-synthesized LCO to reach the performance of the commercial LCO from MTI.

LNO shows a significant capacity loss over 100 cycles, which is also reported in literature. Moreover, the commercial LNO from Sigma-Aldrich was identified to be electrochemically inactive and powder diffraction results revealed that it is not a phase pure material.

In the end the mixed LNCO was the best sample in terms of capacity and cycling stability, confirming that the combination of Co and Ni leads to better performances. Additionally, it gives an information about the role of Co and Ni in the lithium layered oxides. As shown Co seems to dominate in terms of synthesis and Ni accommodates the structure and allows higher capacity.

In-situ XRD combined with OEMS measurements were used to monitor the electrochemical behaviour and changes of the structure during the operation of the batteries. From the in situ XRD can be shown at which voltages (capacities) materials start to decompose. Subsequent Rietveld refinement analysis allowed the identification of the lattice parameter and volume changes. The OEMS allows to identify the gas evolution and with an accurate analysis of the data the contribute from the material separate from the electrolyte.

However, a better signal to noise ratio in the XRD patterns, which could be reached with higher loading of the electrodes or a longer measuring time, should be used for being able to perform Rietveld refinement during the phase changes. This favours a better evaluation of the lattice parameters variation during charge. In contrast, acquisition of XRD data on a normal loading of active material and using conventional x-ray tube do not allow a detailed structural analysis while multiple phases occur.

OEMS measurements are suitable for the investigation of the gas evolution and, in combination with the XRD, to understand if gas evolution is arising due to a structural decomposition or just due to electrolyte reactions. The charge resulting from electrolyte decomposition should be compensated by calculation with a baseline measurement, however it was not performed since the OEMS measurements were not completely optimized and should be repeated.

Additionally, to quantify the gas evolution corresponding to the cathode an accurate elemental analysis should be performed to the synthesized materials to proof the composition of the lithium oxides.

This systematically investigation of layered oxides with different transition metal ratios leads to a good understanding of the structure property relationship of these materials.

The present study confirms that each transition metal plays a specific role.[7,21,29] Additionally, a basic knowledge about this family of oxides is mandatory in order to understand more complex systems like lithium excess materials. Furthermore simple layered oxides can be used as precursors for synthesizing more complex materials like HE-NCM (Li-rich) and Ni-rich layered oxides, which are of high interest due to their high energy density.[7-9] The other transition metal which would be interesting to be further studied is Mn, even though it has a slightly different structure.

Eventually, even a lot of research has already been done on layered oxides materials, questions are still there. A multidisciplinary approach would be favourable. In particular, the combination of the material science discipline to some new technical development may result in an increase of the battery performance.

9 Bibliography

1. https://ec.europa.eu/clima/policies/ets/revision_en.
2. Gröger, O., Gasteiger, H. a. & Suchsland, J.-P. Review—Electromobility: Batteries or Fuel Cells? *J. Electrochem. Soc.* **162,** A2605–A2622 (2015).
3. Wold, A., Arnott, R. J. & Goodenough, J. B. Some magnetic and crystallographic properties of the system LaMn 1-xNixO3+?? *J. Appl. Phys.* **29,** 387–389 (1958).
4. Nitta, N., Wu, F., Lee, J. T. & Yushin, G. Li-ion battery materials: present and future. *Mater. Today* **18,** 252–264 (2015).
5. Bruce, P. G., Scrosati, B. & Tarascon, J.-M. Nanomaterials for Rechargeable Lithium Batteries. *Angew. Chemie Int. Ed.* **47,** 2930–2946 (2008).
6. Amine, K., Kanno, R. & Tzeng, Y. Rechargeable lithium batteries and beyond: Progress, challenges, and future directions. *MRS Bull.* **39,** 395–401 (2014).
7. Rozier, P. & Tarascon, J. M. Review—Li-Rich Layered Oxide Cathodes for Next-Generation Li-Ion Batteries: Chances and Challenges. *J. Electrochem. Soc.* **162,** (2015).
8. Manthiram, A., Knight, J. C., Myung, S. T., Oh, S. M. & Sun, Y. K. Nickel-Rich and Lithium-Rich Layered Oxide Cathodes: Progress and Perspectives. *Adv. Energy Mater.* (2016). doi:10.1002/aenm.201501010
9. Liu, W. *et al.* Nickel-Rich Layered Lithium Transition-Metal Oxide for High-Energy Lithium-Ion Batteries. *Angew. Chemie - Int. Ed.* **54,** (2015).
10. Scrosati, B. *Modern Batteries by C. Vincent and Bruno Scrosati*.
11. Yang, M. & Hou, J. Membranes in Lithium Ion Batteries. *Membranes (Basel).* **2,** 367–383 (2012).
12. Robert A. Huggins. *Advanced Batteries 2009*. (2009).
13. (Source: ElectronicDesign.com 22 October 2010).
14. M. S. Whittingham. Science. 192, 1126 (1976).
15. K. Mitzushima, P. C. Jones, P. J.Wiseman, and J. B. G. Mater. Res. Bull. *Mater. Res. Bull.* **15,** 783
16. Buchberger, I. H. Electrochemical and structural investigations on lithium-ion battery

materials and related degradation processes. (2016).

17. Vetter, J. *et al.* Ageing mechanisms in lithium-ion batteries. *J. Power Sources* **147,** 269–281 (2005).

18. Pasquali, M., Passerini, S. & Pistoia, G. in *Lithium Batteries: Science and Technology* (eds. Nazri, G.-A. & Pistoia, G.) 315–360 (Springer US, 2003). doi:10.1007/978-0-387-92675-9_11

19. Arakawa, M. & Yamaki, J.-I. The cathodic decomposition of propylene carbonate in lithium batteries. *J. Electroanal. Chem. Interfacial Electrochem.* **219,** 273–280 (1987).

20. Xu, J. *et al.* Elucidation of the surface characteristics and electrochemistry of high-performance LiNiO $_2$. *Chem. Commun.* **52,** 4239–4242 (2016).

21. Julien, C. M., Mauger, A., Zaghib, K. & Groult, H. Comparative Issues of Cathode Materials for Li-Ion Batteries. *Inorganics* **2,** 132–154 (2014).

22. Laubach, S. *et al.* Changes in the crystal and electronic structure of LiCoO2 and LiNiO2 upon Li intercalation and de-intercalation. *Phys. Chem. Chem. Phys.* **11,** 3278–3289 (2009).

23. Lee, S.-W. *et al.* Improved electrochemical performance of LiNi0.6Co0.2Mn0.2O2 cathode material synthesized by citric acid assisted sol-gel method for lithium ion batteries. *J. Power Sources* **315,** 261–268 (2016).

24. Thackeray, M. M. *et al.* Li2MnO3-stabilized LiMO2 (M = Mn, Ni, Co) electrodes for lithium-ion batteries. *J. Mater. Chem.* **17,** 3112 (2007).

25. Whittingham, M. S. Lithium batteries and cathode materials. *Chem. Rev.* **104,** 4271–4301 (2004).

26. Bréger, J. *et al.* Effect of High Voltage on the Structure and Electrochemistry of LiNi 0.5 Mn 0.5 O 2 : A Joint Experimental and Theoretical Study. *Chem. Mater.* **18,** 4768–4781 (2006).

27. Goodenough, J. B. & Kim, Y. Challenges for rechargeable Li batteries. *Chem. Mater.* **22,** 587–603 (2010).

28. Goodenough, J. B. & Park, K. S. The Li-ion rechargeable battery: A perspective. *J. Am. Chem. Soc.* **135,** 1167–1176 (2013).

29. Schipper, F. *et al.* Review—Recent Advances and Remaining Challenges for Lithium

Ion Battery Cathodes. *J. Electrochem. Soc.* **164,** A6220–A6228 (2017).

30. Thackeray, M. M. Lithiated Oxides for Lithium Ion Batteries. *J. Electrochem. Soc.* **142,** 2558–2563 (1995).

31. Chen, H., Dawson, J. A. & Harding, J. H. Effects of cationic substitution on structural defects in layered cathode materials LiNiO2. *J. Mater. Chem. A* **2,** 7988 (2014).

32. Kalyani, P. & Kalaiselvi, N. Various aspects of LiNiO2 chemistry: A review. *Sci. Technol. Adv. Mater.* **6,** 689–703 (2005).

33. Thackeray, M. M. *et al.* Li2MnO3-stabilized LiMO2 (M = Mn, Ni, Co) electrodes for lithium-ion batteries. *J. Mater. Chem.* **17,** 3112 (2007).

34. Buchholz, D. *et al.* X-ray Absorption Spectroscopy Investigation of Lithium-Rich, Cobalt-Poor Layered-Oxide Cathode Material with High Capacity. *ChemElectroChem* **2,** 85–97 (2015).

35. Antolini, E. LixNi1−xO (0<x≤0.3) solid solutions: formation, structure and transport properties. *Mater. Chem. Phys.* **82,** 937–948 (2003).

36. Antolini, E. LiCoO2: Formation, structure, lithium and oxygen nonstoichiometry, electrochemical behaviour and transport properties. *Solid State Ionics* **170,** 159–171 (2004).

37. Lyu, Y., Liu, Y. & Gu, L. Surface structure evolution of cathode materials for Li-ion batteries. *Chinese Phys. B* **25,** 18209 (2016).

38. Gao, S. *et al.* Elektrochemische und analytische Untersuchung der Ermüdungsprozesse in Lithium-Ionen-Akkumulatoren. *J. Electrochem. Soc.* **162,** XI, 314 S (2015).

39. Kleiner, K. Elektrochemische und analytische Untersuchung der Ermüdungsprozesse in Lithium-Ionen-Akkumulatoren. XI, 314 S (2015).

40. He, X. *et al.* Enhanced electrochemical performance in lithium ion batteries of a hollow spherical lithium-rich cathode material synthesized by a molten salt method. *Nano Res.* **7,** 110–118 (2014).

41. Peng, Z. S. Synthesis by sol – gel process and characterization of LiCoO 2 cathode materials. *J. Power Sources* 215–220 (1998). doi:10.1016/S0378-7753(97)02689-X

42. Zettsu, N. *et al.* Flux growth of hexagonal cylindrical LiCoO 2 crystals surrounded by Li-ion conducting preferential facets and their electrochemical properties studied by

single-particle measurements. *J. Mater. Chem. A* **3,** 17016–17021 (2015).

43. Santiago, E. I., Andrade, A. V. C., Paiva-Santos, C. O. & Bulhoes, L. O. S. Structural and electrochemical properties of LiCoO 2 prepared by combustion synthesis. *Solid State Ionics* **158,** 91–102 (2003).

44. Predoan??, L. *et al.* Electrochemical properties of the LiCoO2 powder obtained by sol-gel method. *J. Eur. Ceram. Soc.* **27,** 1137–1142 (2007).

45. PREDOANA, L. *et al.* Electrochemical properties of the LiCoO2 powder obtained by sol-gel method. *J. Eur. Ceram. Soc.* **27,** 1137–1142

46. Tan, K. S., Reddy, M. V., Rao, G. V. S. & Chowdari, B. V. R. High-performance LiCoO2 by molten salt (LiNO3:LiCl) synthesis for Li-ion batteries. *J. Power Sources* **147,** 241–248 (2005).

47. Han, C. J., Yoon, J. H., Cho, W. Il & Jang, H. Electrochemical properties of LiNi0.8Co0.2-xAlxO2 prepared by a sol-gel method. *J. Power Sources* **136,** 132–138 (2004).

48. Sathiya, M., Prakash, A. S., Ramesha, K. & Shukla, A. K. Nitrate-melt synthesized HT-LiCoO2 as a superior cathode-material for lithium-ion batteries. *Materials (Basel).* **2,** 857–868 (2009).

49. Kwon, T., Ohnishi, T., Mitsuishi, K., Ozawa, T. C. & Takada, K. Synthesis of LiCoO2 epitaxial thin films using a sol-gel method. *J. Power Sources* **274,** 417–423 (2015).

50. Moses, A. W., Flores, H. G. G., Kim, J. G. & Langell, M. A. Surface properties of LiCoO2, LiNiO2 and LiNi1-xCoxO2. *Appl. Surf. Sci.* **253,** 4782–4791 (2007).

51. Ohzuku, T., Ueda, A., Nagayama, M., Iwakoshi, Y. & Komori, H. Comparative-Study of LiCoO$_{2}$, LiNi$_{1/2}$Co$_{1/2}$O$_{2}$ and LiNiO$_{2}$ for 4-Volt Secondary Lithium Cells. *Electrochim. Acta* **38,** 1159–1167 (1993).

52. Reimers, J. N. & Dahn, J. Electrochemical and In Situ X-Ray Diffraction Studies of Lithium Intercalation in Li[sub x]CoO[sub 2]. *J. Electrochem. Soc.* **139,** 2091 (1992).

53. Tarascon, J. M. *et al.* In Situ Structural and Electrochemical Study of Ni 1 ⁄ x Co x O 2 Metastable Oxides Prepared by Soft Chemistry. *J. Solid State Chem.* **147,** 410–420 (1999).

54. Yang, X. ., Sun, X. & McBreen, J. New findings on the phase transitions in Li1−xNiO2:

in situ synchrotron X-ray diffraction studies. *Electrochem. commun.* **1,** 227–232 (1999).

55. Adcock, M. N. S. C. *SCANNING ELECTRON MICROSCOPE OPERATOR'S MANUAL*.

56. Http://hyperphysics.phy-astr.gsu.edu/hbase/quantum/bragg.html. No Title.

57. http://www.icdd.com/.

58. Reference:Physica B.(1993), 192, 55 Authors:Rodriguez-Carvajal, J. Remarks: For a more recent version see Rodríguez-Carvajal, J. Recent Developments of the Program FULLPROF, in Commission on Powder Diffraction (IUCr). Newsletter (2001), 26, 12-19. (http:/.

59. Tsiouvaras, N., Meini, S., Buchberger, I. & Gasteiger, H. A. A Novel On-Line Mass Spectrometer Design for the Study of Multiple Charging Cycles of a Li-O2 Battery. *J. Electrochem. Soc.* **160,** A471–A477 (2013).

60. Meini, S., Piana, M., Tsiouvaras, N., Garsuch, A. & Gasteiger, H. a. The Effect of Water on the Discharge Capacity of a Non-Catalyzed Carbon Cathode for Li-O2 Batteries. *Electrochem. Solid-State Lett.* **15,** A45 (2012).

61. Metzger, M., Marino, C., Sicklinger, J., Haering, D. & Gasteiger, H. A. Anodic Oxidation of Conductive Carbon and Ethylene Carbonate in High-Voltage Li-Ion Batteries Quantified by On-Line Electrochemical Mass Spectrometry. *J. Electrochem. Soc.* **162,** A1123–A1134 (2015).

62. Bugaris, D. E. & Zur Loye, H. C. Materials discovery by flux crystal growth: Quaternary and higher order oxides. *Angew. Chemie - Int. Ed.* **51,** 3780–3811

63. Zheng, J. *et al.* Structural and chemical evolution of Li- and Mn-rich layered cathode material. *Chem. Mater.* **27,** 1381–1390 (2015).

64. Predoana, L., Jitianu, A., Voicescu, M., Apostol, N. G. & Zaharescu, M. Study of formation of LiCoO2 using a modified Pechini aqueous sol???gel process. *J. Sol-Gel Sci. Technol.* 406–418 (2015). doi:10.1007/s10971-014-3611-2

65. Song, M. Y. & Lee, R. Synthesis by sol-gel method and electrochemical properties of LiNiO2 cathode material for lithium secondary battery. *J. Power Sources* **111,** 97–103 (2002).

66. McCusker, L. B., Von Dreele, R. B., Cox, D. E., Louër, D. & Scardi, P. Rietveld

refinement guidelines. *J. Appl. Crystallogr.* **32,** 36–50 (1999).

67. Hausbrand, R. *et al.* Fundamental degradation mechanisms of layered oxide Li-ion battery cathode materials: Methodology, insights and novel approaches. *Mater. Sci. Eng. B Solid-State Mater. Adv. Technol.* **192,** 3–25 (2015).

68. Wolfgang Weydanz Andreas Jossen. *Moderne Akkumulatoren richtig einsetzen*. (2006).

69. Patridge, C. J., Love, C. T., Swider-Lyons, K. E., Twigg, M. E. & Ramakerd, D. E. In-situ X-ray absorption spectroscopy analysis of capacity fade in nanoscale-LiCoO2. *J. Solid State Chem.* **203,** 134–144 (2013).

70. Zhang, B. *et al.* Role of 1,3-propane sultone and vinylene carbonate in solid electrolyte interface formation and gas generation. *J. Phys. Chem. C* **119,** 11337–11348 (2015).

71. Lee, S. W. *et al.* Improved electrochemical performance of LiNi0.6Co0.2Mn0.2O2 cathode material synthesized by citric acid assisted sol-gel method for lithium ion batteries. *J. Power Sources* **315,** 261–268 (2016).

72. Strehle, B. *et al.* The Role of Oxygen Release from Li- and Mn-Rich Layered Oxides During the First Cycles Investigated by On-Line Electrochemical Mass Spectrometry. *Submitted* 1–6 doi:10.1149/2.1001702jes

73. Yamada, S., Fujiwara, M. & Kanda, M. Synthesis and properties of LiNiO2 as cathode material for secondary batteries. *J. Power Sources* **54,** 209–213 (1995).

74. Fu, L. J. *et al.* Electrode materials for lithium secondary batteries prepared by sol-gel methods. *Prog. Mater. Sci.* **50,** 881–928 (2005).

75. Morcrette, M. *et al.* New phases and phase transitions observed in Li(1-x)CoO2 during charge: In situ synchrotron X-ray diffraction studies. *J. Power Sources* **81–82,** 100–103 (1999).

76. Morcrette, M. *et al.* In situ X-ray diffraction techniques as a powerful tool to study battery electrode materials. *Electrochim. Acta* **47,** 3137–3149 (2002).

77. Pouillerie, C., Suard, E. & Delmas, C. Structural Characterization of Li1−z−xNi1+zO2 by Neutron Diffraction. *J. Solid State Chem.* **158,** 187–197 (2001).

78. Manthiram, A., Knight, J. C., Myung, S. T., Oh, S. M. & Sun, Y. K. Nickel-Rich and Lithium-Rich Layered Oxide Cathodes: Progress and Perspectives. *Adv. Energy Mater.* **6,** (2016).

10 List of figures

11 List of abbreviations

AM ..... Active material
BET ..... Brunauer, Emmett and Teller, method for determination of specific surface area
BEV ..... Battery electric vehicle
CA ..... Citric Acid
cif ..... Crystallographic information file
DMC ..... Dimethyl carbonate
EC ..... Ethylene carbonate
EG ..... Ethylene Glycol
EMC ..... Ethyl
EV ..... Electric vehicle
HE-NMC ..... High-Energy Nickel-Cobalt-Manganese oxides
HEV ..... Hybrid electric vehicle
IRC ..... Irreversible capacity loss
LCO ..... $LiCoO_2$
Li Lithium
LiB ..... Lithium ion battery
$LiMPO_4$ ..... Lithiummetalphosphate
LNCO ..... $LiNi_{0.5}Co_{0.5}O_2$
LNO ..... $LiNiO_2$
LP57 ..... Rrganic electrolyte, 1 M $LiPF_6$ in EC : EMC 3 : 7
MS ..... Mass spectrometer
Ni-Cd ..... Nickel-Cadmium battery
Ni-MH ..... Nickel metal hydrate battery
NMC ..... $Li(Ni_{0.33}Mn_{0.33}Co_{0.33})O_2$
NMP N-methyl-2-pyrrolidone
OEMS ..... On-line Electrochemical Mass Spectroscopy
PC ..... Propylenecarbonate
PVdF ..... Polyvinylidene-difluoride
SEI ..... Solid electrolyte interface
SEM ..... Scanning Electron Microscopy
Super C65 ..... Carbon black, conductive carbon
TEC ..... Chair of Technical Electrochemistry at Technical University Munich
TGA ..... Thermogravimetric analysis
XRD ..... X-ray diffraction

12 Appendices

12.1 List of samples

Table 9: List of LCO samples.

Sample Nr $LiCoO_2$	Method
CG_1.1	Flux synthesis (NaCl)
CG_2.1	Sol-gel Ethylene glycol Peng et all.
CG_2.2	Sol-gel Ethylene glycol Peng et all.
CG_2.3	Sol-gel Ethylene glycol Peng et all.
CG_2.4.1	Sol-gel Ethylene glycol Peng et all.
CG_2.4.2	Sol-gel Ethylene glycol Peng et all.
CG_3.1	Sol-gel Water Predoana et all.
CG_3.2_1/2	Sol-gel Water Predoana et all.
CG_3.3_1	Sol-gel Water Predoana et all.
CG_3.3_2	Sol-gel Water Predoana et all.
CG_3.4	Sol-gel Water Predoana et all.
CG_3.5	Sol-gel Water Predoana et all.
CG_3.6.1	Sol-gel Water Predoana et all.
CG_3.6.2	Sol-gel Water Predoana et all.
CG_3.8	Sol-gel Water Predoana et all.
CG_3.9	Sol-gel Water Predoana et all.
CG_3.11.	Sol-gel Water Predoana et all.

12.2 Rietveld Refinements of samples

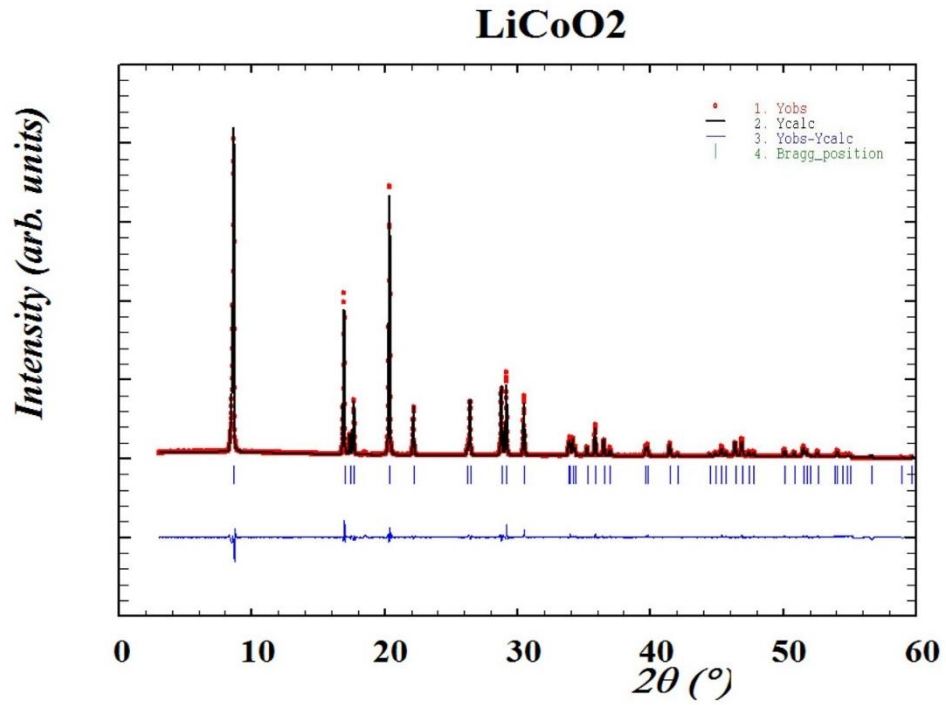

Figure 68: Rietveld Refinement for the LiCoO2 (R-3m), sample 3_2.

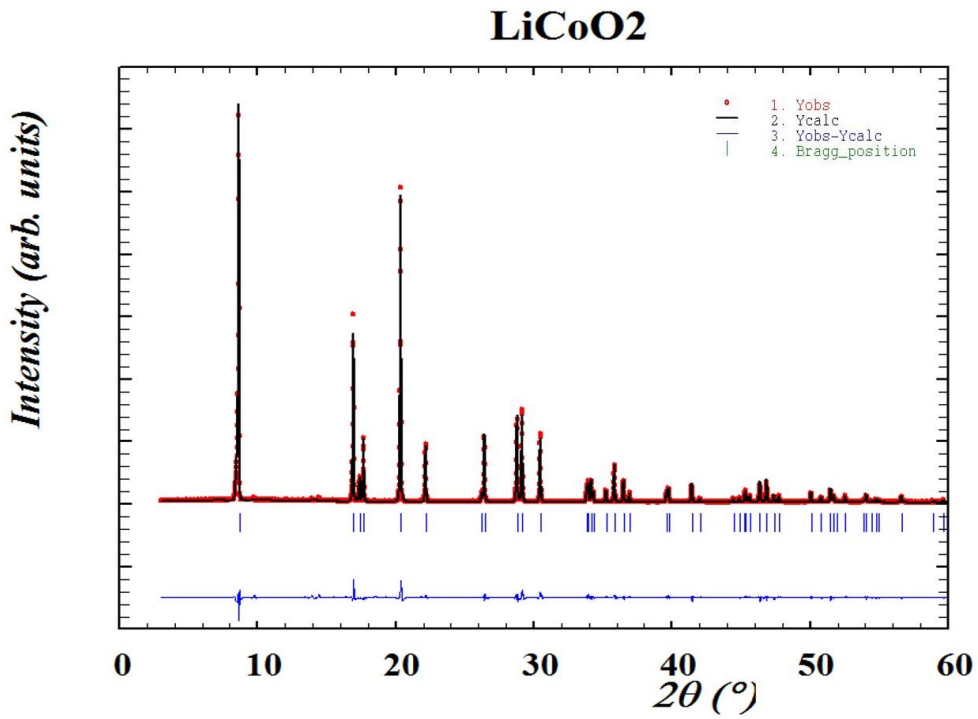

Figure 69 Rietveld Refinement for the LiCoO2 (R-3m), sample 3_5.

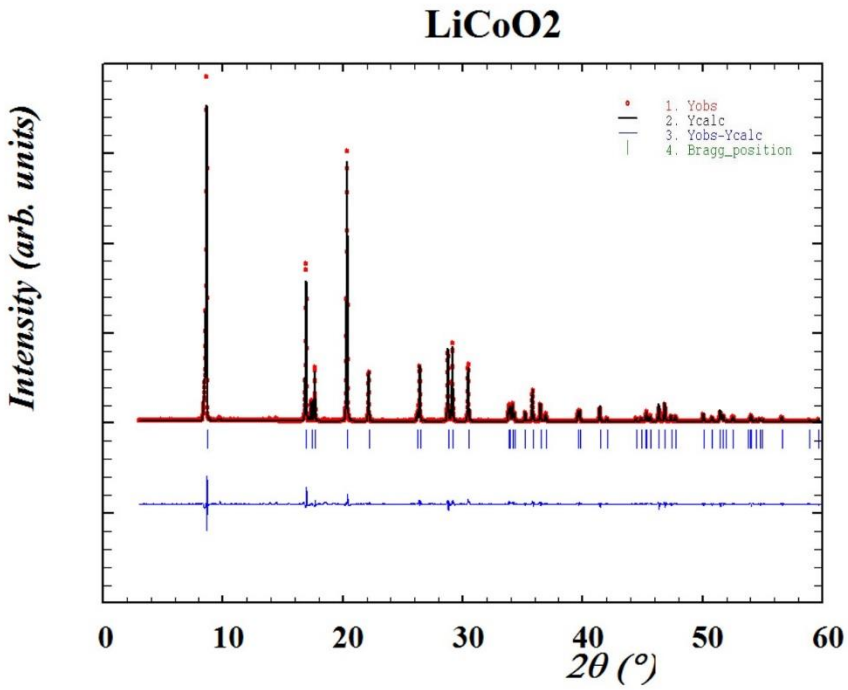

Figure 70 Rietveld Refinement for the LiCoO2 (R-3m), sample 3_9

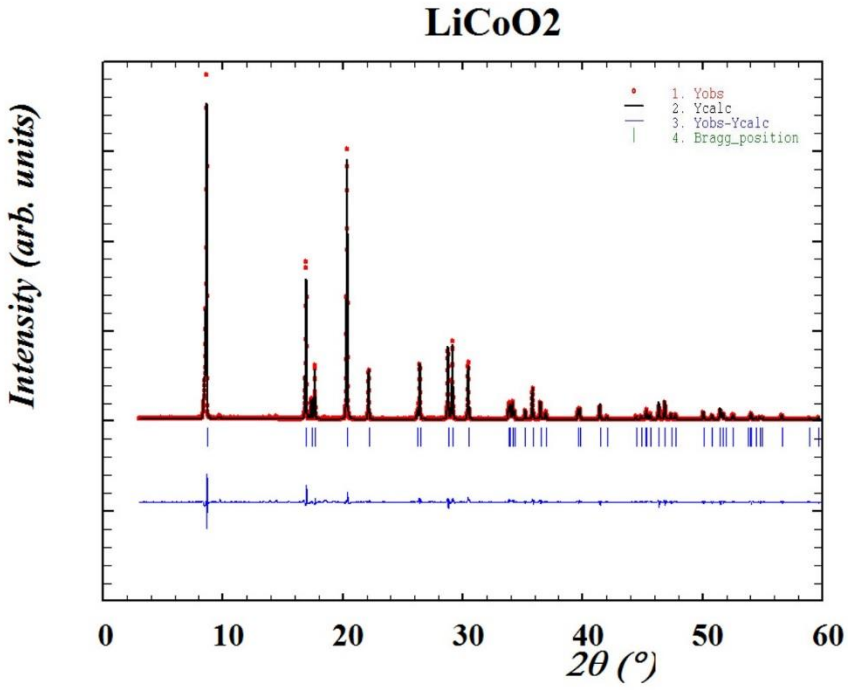

Figure 71: Rietveld Refinement for the LiCoO2 (R-3m), sample 3_11.